Development of a fundus camera with adaptive optics using a pyramid wavefront sensor

OÉ Gaillimh
NUI Galway

Sabine Chiesa

Supervised by Professor Chris Dainty

An Grúpa Optaic Feidimí
Ollscoil na hÉireann, Gaillimh

A thesis submitted in partial fulfillment of the requirements for the degree of Doctor of Philosophy and the Diploma of the National University of Ireland, Galway

School of Physics, Department of Experimental Physics,
College of Science, National University of Ireland, Galway,
Ireland Éire

January 2012

Contents

List of Figures

5

Abstract

This PhD thesis presents the building of an adaptive-optics system based on a pyramid wavefront sensor applied to the imaging of the human retina (fundus) in vivo. The instrument aims to simultaneaously measure the ocular aberration, and correct it to allow the imaging of the fundus.

The adaptive optics system uses a high-stroke magnetically-actuated deformable mirror with 52 elements that presents a correction range best adapted to the refraction in most non-emmetropic eyes and the appropriate surface deformation required for the correction of high-order ocular aberrations. This wavefront correction system is coupled with a sensor originally used in astronomy here selected for ophthalmic use due to its adjustable dynamic range that insures characterization of the ocular measurement and due to its robustness in adaptive optics applications. The retinal imaging is based on a green illumination (530nm) commonly used in commercial fundus cameras in clinical environments but to our knowledge not yet applied in the existing high-resolution systems imaging the retina at the cellular level.

The calibration of the instrument response to the ocular aberration is performed using ophthalmic lenses and custom phase plates representing typical patterns. Adaptive optics correction is applied to these complex refractive elements and to typical test objects to estimate the improvement in retinal image quality. Using safe light levels and an experimental protocol agreed by the Research Ethics Committee of the National University of Ireland, Galway, a high-resolution image of the retina was obtained after correction of the refractive error. Use of this system for imaging at the cellular level would require additional changes.

Acknowledgements

First of all I would like to thank Prof. Chris Dainty for giving me the opportunity to work in his group in Galway on this project and for the guidance and support thorough its development stages. It was a great chance to attend the high-quality lectures, colloquia and training sessions in Galway and elsewhere over these four years.

I would like to thank also Prof. Adrian Podoleanu and his group of Applied Optics, from University of Kent, Canterbury, United Kingdom (UK), for hosting this research over summer 2009.

I would like to thank Dr. Eamonn O'Donoghue from the NUIG Eye Clinic for his renewed enthusiasm and interest in the ophthalmic research carried out in the Applied Optics NUIG.

I would like to thank Dr. Stéphane Chamot for reviewing of the 2006 Engineering the eye workshop paper and for his inputs on the project. I would like to thank Dr. David Lara-Saucedo for double checking of the location of the retinal capillary in Figure 2.6a with the large-field fundus image of Figure 2.6c, and Prof. Ann Elsner for her analysis of the retinal images and identification of the macular pigment signal in Figure 2.6b.

From Galway I would like to thank Dr. Elizabeth Daly for the training on the system built by Chamot et al., for the Fisba interferometer data of Figure 3.13, and for reviewing of my work. I would like to thank Dr. Andrew O'Brien for the LED-based illumination system and for the design of the electronics board. I would like to thank Dr. Gerard O'Connor for the review of the ocular safety levels.

I would like to thank Dr. Eugénie Dalimier for the numerical analysis of the deformable mirror, for her review and scientific discussions. I would like to thank Prof. Larry Thibos for the access to the model of 100 typical ocular refractions. I would like to thank Dr. Eric Logean for advises in the lab and for discussions about the eye. I would like to thank Dr. Charles Leroux for the Matlab codes of modal wavefront reconstruction. I thank the Galway University Workshop for the machining of the fix-

ation target mechanical mount, of the electronics trigger board and help in electronics testing. I would like to thank Dr. Fabien Bernard from the NCLA for the machining of the illumination masks.

Chapter 1

Thesis synopsis

1.1 Thesis synopsis

1.1.1 Aims of the thesis

The aim of this work was first to understand the functioning and the limitations of a prototype adaptive optics system built by Chamot et al. [1] and to use it in the eye, then to design a new adaptive optics system based on the pyramid wavefront sensor and a high-stroke deformable mirror, and to implement a retinal imaging system using adaptive optics.

Over the first year of this project first results were acquired with the existing system, then the optical design for the new system with the Mirao was made in Zemax, the software for the adaptive optics control of the new mirror was written in LabVIEW 8.2 and applied to the correction of a static aberration. The second year of this project the new retinal imaging system was used in one eye with adaptive optics. The third and fourth year were spent on improving the adaptive optics efficiency and the retinal imaging through the calibration of the wavefront aberration measured by the sensor and through the successive implementation of a single-LED flash, a Xenon flashlamp coupled with Halogen source and of a multiple-LED flash as illumination systems.

1.1.2 Summary of Chapters

Chapter 1 presents the PhD goals, the thesis report contents and the instances of poster and oral presentations throughout the PhD timeline.

Chapter 2 briefly describes the principles of fundus cameras through the review of today's instruments and of their limits. The initial adaptive optics system built by Dr. S. Chamot and Dr. S. Esposito in which an imaging arm designed by Dr. E. Daly, a flash-illumination system built by Dr. A. O'Brien and a fixation target designed and built by the author in the illumination arm retrieved a 1-degree off-axis image of the fundus in an healthy and young eye. From these results, improved performance was expected by building a new system with the Mirao52-d (Imagine Eyes, France).

Chapter 3 describes the principles on which the new pyramid wavefront sensor system design was developed, and presents the experimental calibration and alignment procedure. The importance of the beam modulation at the pyramid and the relation to the sensor dynamic range is demonstrated. Typical open loop wavefront measurements were performed to calibrate the sensor response and the ocular wavefront reconstruction.

Chapter 4 describes the components of the adaptive optics system and the control algorithm used in conjunction with the deformable mirror. Experimental correction of static wavefronts used for the open loop calibration is presented. The application of the closed loop adaptive optics to a static object is illustrated.

Chapter 5 describes the retinal imaging system used in the eye. Light coupling efficiency from the eye to the camera device is presented for a set of static objects. The resolution limit of the system is estimated and preliminary results of in-vivo retinal imaging with adaptive optics are described.

Chapter 6 contains the summary of the results and the conclusions of this work. From the author's point of view, more characterization and improvements remain to be done before this technique can be used in a clinical environment. Problems encountered and possible future works are discussed.

Appendix A describes the software developed for the acquisition of retinal images

and of the wavefront sensor data. The identification of a wavefront sensor frame to a retinal image frame over time was possible only in the post-processing.

Appendix B contains the ocular safety limits calculations for the instrument for the data collection protocol, which was granted approval by the NUI Galway Research Ethics Committee. All volunteers involved in this study gave informed consent.

1.2 Presentations of the work in this thesis

1.2.1 Poster presentations

Adaptive optics system for retinal imaging based on a pyramid wavefront sensor and 52-element magnetically actuated deformable mirror, S. Chiesa, E. Daly, S. Chamot, C. Dainty, 6th International Workshop on Adaptive Optics for Industry and Medicine, Galway, Ireland, 2007.

Adaptive optics with pyramid wavefront sensing for fundus imaging of the human retina, S. Chiesa, E. Daly, S. R. Chamot, C. Dainty, Photonics Ireland, Galway, Ireland, 2007.

An adaptive optics assisted retinal imaging system using a pyramid wavefront sensor, S. Chiesa, C. Dainty, 1^{rst} Workshop on OCT and Adaptive Optics, Canterbury, Kent, UK, 2008.

An adaptive optics assisted retinal imaging system using a pyramid wavefront sensor, S. Chiesa, C. Dainty, Photonics Ireland, Kinsale, Co. Cork, Ireland, 2009.

An adaptive optics assisted retinal imaging system using a pyramid wavefront sensor: principle, calibration, in-vivo operation, S. Chiesa, C. Dainty, JTuC6, Frontiers in Optics Joint AO/COSI/LM Poster Session, San José, CA, USA, 2009.

Investigation of the sensitivity of the pyramid wavefront sensor for ophthalmic applications, S. Chiesa, C. Dainty, ARVO 2010, Ft Lauterdale, FL, USA, Invest. Ophthalmol. Vis. Sci. 2010 51: E-Abstract 2308.

An adaptive optics assisted retinal imaging system using a pyramid wavefront sensor, S. Chiesa, C. Dainty, NUI Maynooth Optoinformatics Summer School, Ireland, 2010.

1.2.2   Oral presentations

Fundus camera with adaptive optics using a pyramid wavefront sensor, S. Chiesa, C. Dainty, HIRESOMI Workshop, Porto, Portugal, 25-27/10/2007.

Retinal imaging system with adaptive optics using a pyramid wavefront sensor, S. Chiesa, C. Dainty, HIRESOMI Workshop, NUI Galway, Ireland, 13/07/2009.

Pyramid wavefront sensor, S. Chiesa, C. Dainty, Applied Optics Kent Group Meeting, University of Kent, Canterbury, UK, 21/08/2009.

An adaptive optics assisted retinal imaging system using a pyramid wavefront sensor, S. Chiesa, C. Dainty, 7th International OSA Network of Students IONS Meeting, NUI Galway, Galway, Ireland, 04/03/2010.

Adaptive optics and imaging of the eye, CORIA Rouen Invited Seminars, Rouen University, Saint-Etienne du Rouvray, France, 09/03/2010.

Fundus camera with Adaptive Optics Using a Pyramid Wavefront Sensor, S. Chiesa, C. Dainty, 4th HIRESOMI Workshop, Orsay, France, 15/07/2010.

Chapter 2

Introduction

We extended existing work and results obtained in the eye with a pyramid wave-front sensor-based adaptive-optics system [1] to high-resolution retinal imaging. An electromagnetically-actuated high-stroke deformable mirror was selected to improve the range of correction of the ocular aberration. Part of this work was devoted to the question whether the pyramid sensor is an appropriate sensor for the characterization of the ocular aberrations. Another part was devoted to in-vivo imaging of the human fundus using the pyramid sensor in an adaptive optics configuration.

2.1 Retinal imaging systems and adaptive optics

This section is intended to introduce the principles of retinal imaging by commercial instruments and their importance in the diagnosis of retinal diseases in clinical environments. The role of ocular aberrations in high-resolution imaging is related to their correction by adaptive optics. The recent instruments developed for high-resolution imaging of the retinal structures have increased the knowledge of the photoreceptor functionality.

2.1.1 Principle of the fundus camera

An image of the fundus is obtained by illuminating the eye from the pupil (defined at the iris) in Figure 2.1. Medical assessment of the retinal health is performed with images from commercial fundus cameras (Zeiss FF450 for example), which subtend a

20-30 degree field in the eye. This represents twice the distance from the optic disk to the macula.
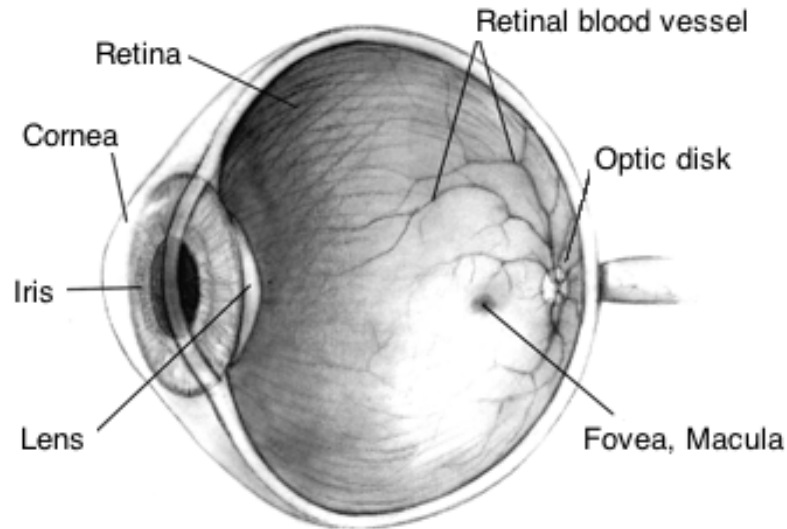
Figure 2.1: General view of the human eye, pointing the optics of the eye (Cornea, Iris aperture, Lens) and simple retinal structures: Macula surrounding the Fovea, Retinal blood vessels that supply the nutrients for the cells and nerves which gather at the Optic disk.

From histology we know that the retina is formed of multiple layers of cells. The different cellular layers are illustrated in Figure 2.2. Most of the light reaching the retina is absorbed, or scattered within the cellular layers thus only a very small fraction of the illumination exits the eye. Light that reaches the camera to form the fundus image is the portion of the illumination backreflected by the retinal cells out of the eye and propagating through the imaging system.

The human visual process is based on the electro-chemical potentials generated by the photoreceptors cells in response to an illumination. Ganglion cells, nerve fibers and neurones activated by these signals transmit information to the brain via the optic disk. When retinal cells do not function properly, the visual process is affected. To prevent complete vision loss, and detect diseases at an early stage, in-vivo imaging of these light-sensitive cells may be helpful. Affected cells are identified by the practitioner from their lower signal compared to the healthy background. High-resolution images showing individual cells are however achieved only with customed instruments. Diagnosis is then performed over a field of view of 2x2 degrees squared diameter subtense in the eye, located in the retina by the subject fixation position.

In this work we propose to implement a high-resolution retinal imaging system with a
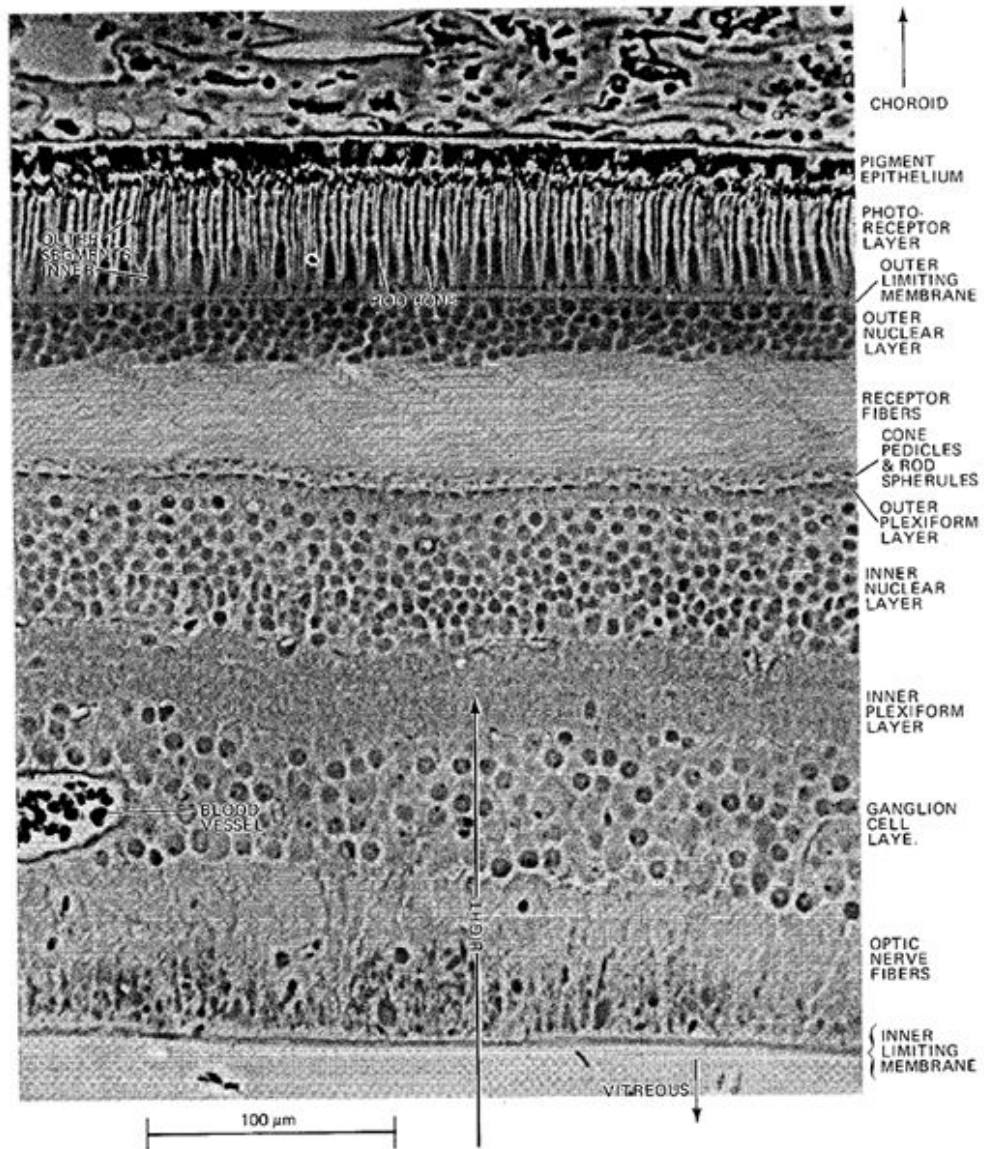
Figure 2.2: Histological section of the retinal layers in the human eye about 4° from the fovea, from S.L. Polyak, 1941 [2].

4x4 degree image to allow rapid identification of the image field location in the retina. Diffraction-limited cellular sampling in the central part of the image was provided by adaptive optics. Several illumination sources and types of camera triggering were set up to obtain an image of short exposure and high resolution of the retina.

2.1.2   Influence of the ocular aberration on retinal imaging

From diffraction theory it is well known that in the absence of aberrations the image of a point source object located at infinity from a circular aperture becomes an Airy function after transmission through this pupil which forms a diffraction-limited optical system. The presence of optical aberrations in this system deteriorates the Airy disk peak intensity, and in turn the signal transmission from the object to the acquisition system. An illustration of the point spread function modification due to an aberration is presented in Figure 2.3.

The aberration pattern measured at the sensor corresponds to the on-axis wavefront departure from the 'perfect' wavefront applied to the light coming from the retina [3]. Aberrations are separated into low-order and high-order types as a function of their shape complexity. Large pupil diameters – such as after pupil dilation by ophthalmic drugs – present larger amplitudes of high-order aberrations than small pupil diameters. The digital image is degraded by the ocular aberrations that affect all the secondary point-sources of the retina, formed in response to the illumination (wavefront sensor probe beam or flashed Maxwellian illumination). The image becomes diffraction-limited after implementation of an aberration compensation system (e.g. adaptive optics).

Isoplanaticity
The isoplanatic angle is the angle over which the wavefront (and hence point spread function) are reasonably constant. If the corrected on axis point spread function has a Strehl ratio of 1.0, then it is generally accepted that the isoplanatic angle is the angle for which the Strehl ratio of the point spread function is 0.37, which is equivalent to an rms wavefront aberration of 1 rad. The isoplanatic angle can vary quite widely, but in a typical eye is on the order of 2-4 degrees [4]. For adaptive optics, the isoplanatic angle defines the angular subtense of the image for which the diffraction-limited image quality is achieved by referencing the correction on the central (reference) point spread function. Out of this zone usually centered on the optical axis, the correction is only partial. To achieve diffraction-limited image quality, additional adaptive optics
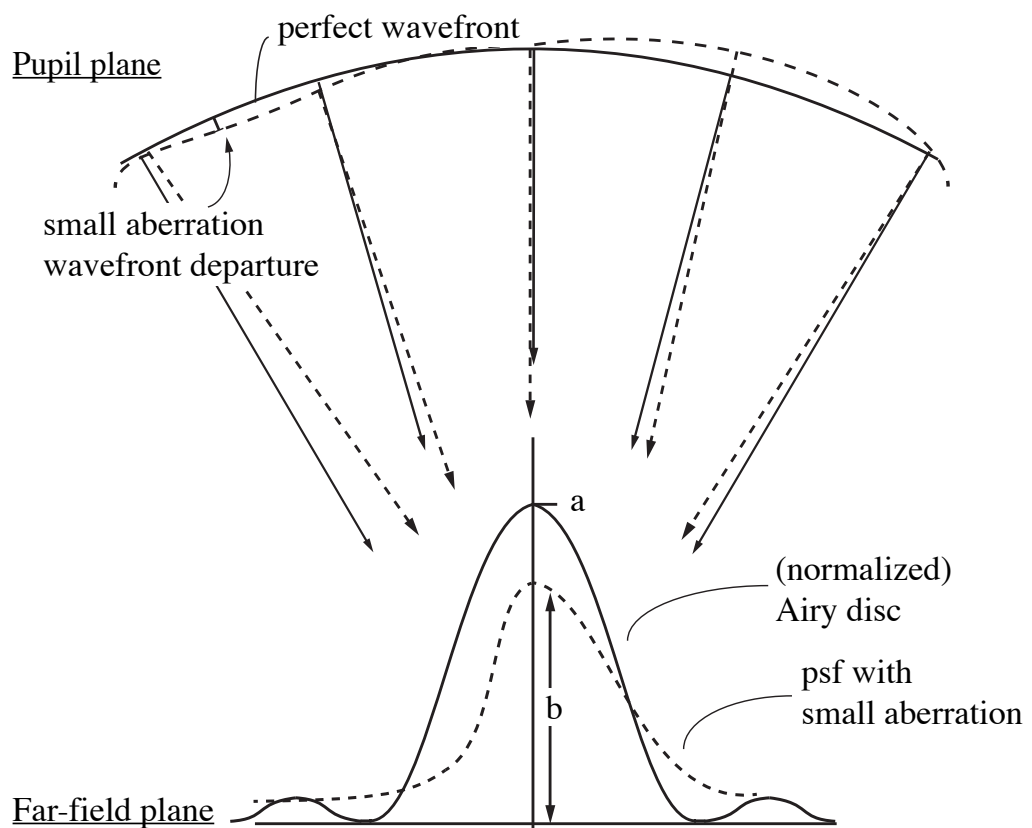
Figure 2.3: Aberration effect on the point spread function of a system. The ratio of the peak intensity for the aberrated signal (b) to the peak intensity for the perfect signal (a) is the Strehl ratio (S=b/a). 0.8⩽S⩽1 defines a diffraction-limited image. From Prof. C. Dainty, Imaging Lectures.

19

correction referenced on an outer part of the image define a new isoplanatic angle. Such an optical configuration represents multi-conjugate adaptive optics.

Chromatic aberrations

Chromatic effects are due to the fact that the refractive index of the optical media is a function of the wavelength. The longitudinal and transverse chromatic aberrations of the imaging system are minimized for the static aberration of an artificial eye by the use of achromat lenses. Compensation of the image focal plane position shift is observed with achromat lenses and use of multiple wavelengths of the visible. Retinal imaging is however subject to the longitudinal chromatic aberration of the eye compensated by a quantified amount of defocus. The correction requirement as a function of the imaging wavelength for the observation of a given retinal layer at the science camera in an healthy eye was developed and used by other teams [5,6,7].

Light scatter in the eye

Scatter is not an aberration described by classical optics but is mentioned here as a factor that reduces the signal to noise ratio. The back-scattered signal from the retina is the source for the wavefront sensing and for imaging the eye, as illustrated in Figure 2.4. Scatter occurs in the eye first in the anterior segment and second in the retina. In the ocular media (that is the cornea, the crystalline lens, and the vitreous humor), the shorter the wavelength the more the scattering [8,9,10]. Meanwhile, in the retina the longer the wavelength the deeper the light penetration in the tissue and the more the scattering.
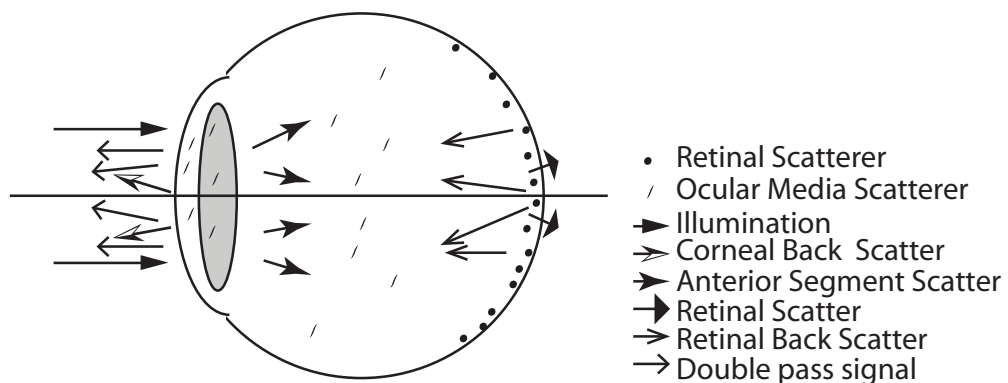
Figure 2.4: Schematic of ocular scatter mechanism. Wavefront sensing and image acquisition is performed with the double pass signal, backscattered from the retina through the ocular media. Backscatter by the crystalline lens is not represented for clarity purposes.

For a 3μW laser power (635nm) and fixed camera exposure, the image of the probe

beam was first recorded in the human eye and afterwards recorded through an achromat lens with an artificial retina formed by a paper card or formed by a metallic support. A narrower and more intense probe beam signal than in the human eye was observed in the artificial eye. The spread of the incoming probe beam was attributed to in-depth scatter related to the retinal layers (tissues, blood cells and other organic components).

The most reflective layer for this wavelength was assumed to be at the photoreceptors outer segment despite other layers of the volume also backscatter light in the direction of the acquisition camera. Optical conjugation of the image plane with the outer segment of the photoreceptors under Maxwellian illumination corresponded to a background signal intensity peak. Polarization filtering of the retinal signal was shown to filter the unwanted scattering in the retinal image for confocal scanning ophthalmoscopes [11]. Improvement of image quality in fundus imaging using polarized optics was implemented in a commercial fundus camera used in the work described further in Figure 2.6c. A pinhole placed in a conjugate plane of the imaged layer used in confocal microscopy protected the detector from light backscattered by out-of-focus layers. Fundus images of the systems further described were acquired without confocal optics, thus contained light from all layers.

2.1.3 High-resolution retinal imaging systems

The following section describes a few existing instruments used for retinal imaging purposes and how they benefited from the implementation of adaptive optics correction systems. High-resolution retinal imaging refers to the identification of the photoreceptor cells outer segment in an image of the human retina. This identification had been realized based on statistical methods of speckle interferometry [12], or deconvolution of the retinal image by the wavefront sensor signal [13]. Adaptive optics refers to the image quality improve obtained in a science camera by mechanical action (correction) on the phase aberration measured by a wavefront sensor. In 1997, Liang *et al.* [14] presented the first images of photoreceptors obtained after correction of high-order ocular aberrations with adaptive optics. Liang's correction system was based on a deformable mirror in a feedback loop controlled by a Shack Hartmann wavefront measurement. The benefit of adaptive optics on the signal was such that the technique was extended to other fundus-imaging instruments.

Flash-based fundus cameras

Commercial fundus cameras (Zeiss, Topcon) are the most commonly used instruments for imaging of the human retina without adaptive optics. The focus on the retinal layer of interest is set up using a continuous illumination of low power then the image is acquired using the aperture of a mechanical shutter triggered with a high power illumination flash. A high quality image of the retina (or fundus image) over 20 degree to 40 degree field is obtained but the resolution is too low to image single photoreceptors. Adaptive optics flash-based fundus cameras have a smaller image field (typically 1×1 or 2×2 degrees) but retrieve photoreceptor cells images after correction of the ocular aberrations. Light comes from all the retinal layers and image post-processing is required to improve the signal. After the demonstration of signal improvement was realized, research was carried out to obtain fast acquisition rates that led to a time-resolved identification of the photoreceptor activation [15,16]. Functional imaging of the photoreceptor mosaic [17,18], identification of the locus of fixation [19], or imaging of the retinal rods [20] is possible with such instruments.

Confocal systems

In a confocal scanning system, a single pixel detector (photomultiplier) is placed behind a pinhole whose position along the optical axis (z axis in the cartesian coordinates system) defines the retinal layer from which the light is scattered. Lateral and vertical scanning of the sample is provided by the scanning mirrors on the order of MHz for the horizontal scan and on the order of kHz for the vertical scan. The final image is obtained in around 50ms. In these very short integration times and with the confocal pinhole, the light that reaches the photo-multiplier is free of scattering from retinal layers other than the one in focus. The main advantage of these systems is that the high resolution of the instrument is maintained through the in-depth imaging of the sample layers, which leads to a volumetric reconstruction of the retinal structures. The image is nevertheless only monochromatic, and requires a lot of post processing for compensating the image jitter related to the scanning speed variation [21] and for the eye saccades. These systems led to the identification of functional imaging of retinal cells in AO-SLOs such as the color sensitivity function of the cones photoreceptors [22]. Additional characterization of this signal was obtained by the identification of the cones long-course infrared signal changes emitted in response to a visible light stimulus [23], (or intrinsic optical signal). Many results of in-vivo observations of a single layers along the retina depth were achieved by AO-SLOs instruments [24,25,26].

Two-photon microscropy

Two-photon microscopy images are formed by the emission of a photon induced by laser excitation of the fluorescent agent inserted in the biological sample. The name comes from the fact that the absorption of two laser photons by the fluorophore is necessary to induce the emission. Given the automatic filtering of the volumetric scattering towards regular fluorescence imaging with adaptive optics in animals [27, 28] the signal is very clear. However, the light levels required to induce the emission process lead to cell death after bleaching. Two-photon microscopy is a fast process that was applied to the measurement of the retinal pigment epithelium [29] with a femtosecond laser and is of growing interest in human applications.

Optical Coherence Tomography (OCT) systems

OCT systems are based on the post processing of the interference signal created between a reference wave and the signal from the retina. Initial systems (Time Domain OCT) were based on axial scanning of the reference mirror, providing 3D-imaging of the sample. Spectral Domain OCT (SD-OCT) has progressively replaced Time-Domain OCT, avoiding the z-scanning requirement [30]. Speckle deterioration of the OCT images due to the use of very coherent sources was greatly reduced with use of swept-source fibre lasers. Retinal imaging OCT systems, unless used in an adaptive optics configuration, are mainly limited by a low transverse resolution [31, 32, 33]. Volumetric imaging of the retina is obtained at a scanning rate of about 2 second per stack, whose post processing can take several days but retrieves identification of the cones slow retinal intrinsic optical signal [34] as a highly punctuated and bright reflection spot vanishing in adjacent frames or of the Stiles Crawford response [35]. The advantage of adaptive optics was demonstrated in observations of the cones mosaic [36] and in the observation of the retinal cellular structure [37, 38].

Between 2006 and 2011, the implementation of high-stroke deformable mirrors in adaptive optics retinal imaging instruments extended their use to the measurement of higher amplitudes of ocular aberration [39]. Additional results were obtained using these new technologies in OCT retinal imaging systems [40].

The adaptive optics system based on the pyramid sensor measurement built during the thesis is described further in Chapter 4. This system aims at high-resolution retinal imaging using a high-stroke mirror in the adaptive optics. Ocular aberrations in the range ± 3 diopters (D) as characterized by the sensor measurement can be corrected.

2.2 Design requirements for an adaptive optics retinal imaging system

In this section we will present the design requirements in Section 2.2.3. In order to understand how these requirements were determined, the results obtained with the OKO19Piezo deformable mirror system are described in Section 2.2.1. The system limitations that defined the requirements and mechanical constraints are discussed in Section 2.2.2.

2.2.1 Initial system description

The data acquisition was realized with the optical system represented in Figure 2.5. The sensing of the aberrations of the eye was obtained by a Helium Neon laser (633nm) backscattered from the retina to the pyramid prism. The focus error of the subject was corrected before sensing by modifying the optical path length of the imaging system with a Badal stage until the probe beam point spread function size was minimal at the science imaging camera. Circular modulation of the focused beam around the tip of the pyramid was induced by a Newport fast steering mirror running at 100Hz resulting in 4 pupils reimaged on the wavefront sensing camera. Custom LabVIEW 7.0 (National Instruments, Austin, TX, USA) software detected the wavefront aberrations after correction of the focus error and determined the mirror command controls required to correct for the higher-order aberrations by singular value decomposition of the wavefront gradients. Adjusting the camera binning to get 16 pixels across the 385μm pupil and the modulation radius to small values (7λ/D, where D is the diameter of the pupil image on the steering mirror), the typical residual wavefront error of the closed–loop mode reached 0.1μm root mean square (λ/8) at 55Hz frame rate and 10ms exposure frame.

From the definition of the point spread function of a diffraction–limited system, a 2.2μm Airy radius was obtained at the retina of a model eye of 16.7mm focal length with a 6mm pupil diameter at 633nm. The same pupil aperture magnified to 30mm and focussed by a 400mm focal length lens in the imaging system formed a point spread function of 10.5μm (633nm) at the imaging camera. From these values, a 5$\times$ magnification factor was estimated between the retinal plane and its conjugate plane at the imaging camera. An adjustable diaphragm was placed in a conjugate retinal plane to allow adjustment of the imaging field of view, with a 0.6$\times$ magnification be-
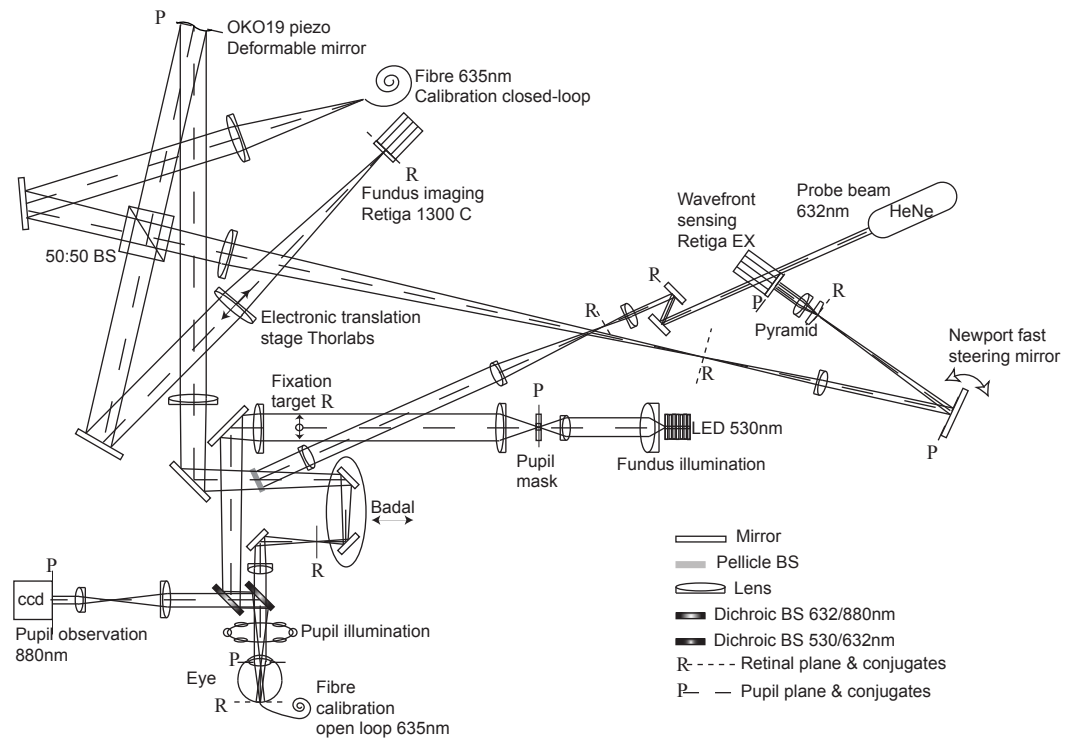
Figure 2.5: Layout of the optical system for retinal imaging using the OKO19 Piezo mirror. The average illumination power at the eye was 20μW (530nm), the average wavefront sensor beacon power at the eye was 3μW (633nm). Exposure time of the wavefront sensor camera was 10ms and exposure time of the science camera was 200ms. Sensor frame rate was 55Hz for 16x16 pixels across the pupil.

tween the camera image and the diaphragm planes. The region of interest selected on the camera was defined to cover the diaphragm field of view, as presented in Figure 2.6a, where the internal disk highlighted a 3.15°-diameter retinal zone (∼1mm diameter).

Retinal image acquisition was performed with a 530nm–pulsed illumination arm delivering 200ms flashes of 20mW power at the output of the source optics, added by E. Daly and A. O'Brien to the original system [1]. Flash synchronization with the image acquisition camera (Retiga 1300C, QImaging Corp., Canada) enabled repeated imaging of a single location in the eye. The 20mW power out of the LED–collimation assembly was reduced down to 20μW average power (4μJ per single flash) at the pupil of the eye due to the vignetting by the optics of the system. The fixation target designed and built by the author was placed in a conjugated retinal plane in the illumination path which enabled a quantified rotation of the eye's line of sight and imaging of a retinal structure as in Figure 2.6a. The fixation target was visible in the image of Figure 2.6b, in which the subject was asked to fixate at the edges of the diaphragm while the target remained centered on the optical axis of the system. With the Emsley reduced eye model in the optical design, an eye movement of 0.5° towards the line–of–sight was obtained with a 2.9mm shift of the fixation target towards the optical axis of the illumination optics.

2.2.2 Discussion of the results, limits of the system

1. Wavefront sensor signal quantification: The wavefront reconstruction was obtained by identification of the sensor signal to a phase departure at the pupil of the eye. The calibration was based on the least squares fit of the sensor signal recorded for the deformable mirror influence functions with the mirror surface deflection recorded for the same influence functions with a phase shifting interferometer (Fisba Optik, Switzerland). This method required post-processing of the sensor signals recorded to quantify the phase aberration and did not allow in-situ visualization of the rms.

2. Piezoelectric membrane hysteresis and mirror stroke limits: The piezoelectric structure of the deformable mirror membrane was limited in stroke and in turn to the correction of ocular aberrations of amplitude below 0.25 diopter. The adaptive optics code was not programmed to account for membrane hysteresis, which propagated numerical errors to the wavefront reconstruction.

3. Imaging wavelength: Infrared wavelengths are widely used for the comfort of the patient and retrieve sharp imaging of the photoreceptors mosaic with adaptive optics but clinical instruments diagnostics are based on visible light images. Previous results of the fundus autofluorescence to multi-wavelength illumination were obtained with flash-based fundus camera 470nm, 550nm and 650nm sources [22] then with a scanning ophthalmoscope at 532nm, 658nm and 840nm [7]. Fluorescence images of the fundus in medical devices with the use of a fluorescent agent (angiography) rely on the acquisition of the 500-520nm emission activated with 488nm light. In this work, no fluorescent agent is used, and the structures contrast in the image obtained with light backscattered from the retina is chosen for criterion of identification. Extreme attention was required as the human eye sensitivity peaks at 530nm, meaning a healthy human retina is more likely to detect green light than any other wavelength of same absolute intensity on a dark background, thus that high light-levels were uncomfortable and harmful.

4. Retinal structure localization: Knowing that the subject was able to follow the fixation target, the estimate of the position and size of a feature of a retinal capillary acquired as in Figure 2.6a was obtained by reversing the feature distance towards the image center. In addition, a wide-field image of the fundus in Figure 2.6c acquired with a customized flash fundus camera Zeiss FF450 using cross-polarizers (540nm) was used for control of the results. This image confirmed the capillary branch position at $1.45°$ from the locus of fixation marked by the end of the target needle tip. The intensity patches of the retina observed in Figure 2.6b were also identified to the pigment density variations observed at $2°$ nasal from the fixation locus pointed by the needle extremity in Figure 2.6c.

5. Science camera exposure: The illumination system presented here was successfully used to quantify macular pigment optical density in flicker photometry experiment, and for calibration of the imaging resolution using fixed objects. However, used for the acquisition of series of monochromatic images in the eye, only long exposure images (200ms) were obtained. This added to the image an effect of optical blur related to the ocular movement occurring over the camera exposure time. A $50\times$ reduction in the camera exposure was required to reach the light levels used for photoreceptor cones imaging in a 2ms to 10ms (short-exposure) image, as implemented in other groups [41, 14]. To fulfill the eye safety limits and maintain average illumination below harmful levels, a flashed illumination of high-power triggered with the image acquisition was designed.

27

Average of 10 images; B2x2; Exp.200ms

Raw image unknow fixation, B2x2; Exp.200ms

(a)

(b)

(c)
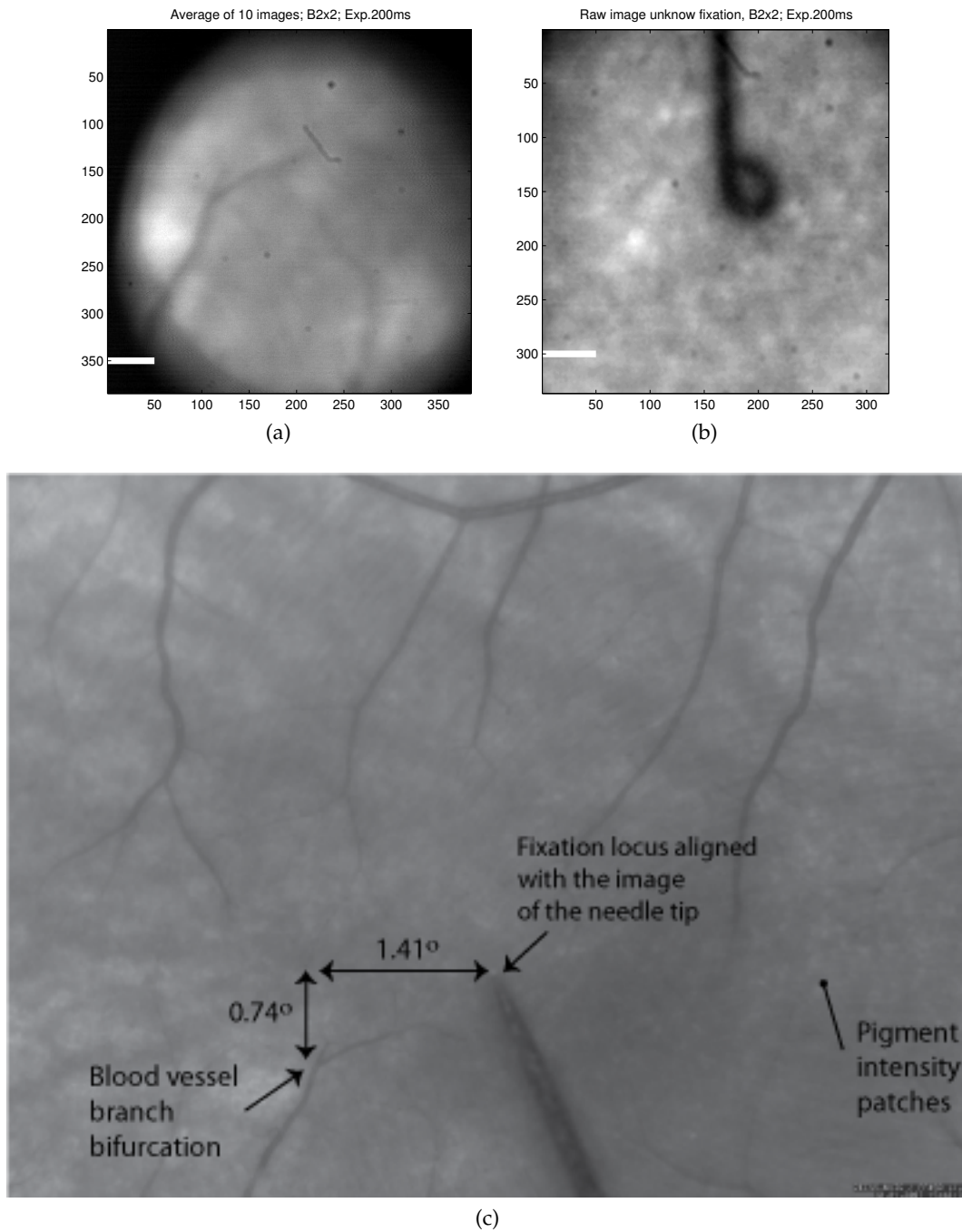
Figure 2.6: a. and b. are PWS-AO retinal images, with E. Daly, and S. Chamot system (fixation target by S. Chiesa). a. Image obtained after averaging of 10 single flashes to reduce Gaussian noise of the raw image. White scale bar is 80μm in the eye. b. Raw image at 200ms for a random fixation the eye while fixation target is in the centre of the field, white scale bar is 80μm in the eye. c. Horizontal field of 8° in the retina of the same subject, 30ms exposure, with modified fundus camera FF450 (courtesy of Dr. D. Lara and Prof. C. Dainty).

6. Imaging resolution: For a diffraction-limited point source located at the retinal plane of a model eye, the point spread function of the system observed through the 6mm diameter aperture defined by the iris of the model eye was of 10.5μm at the conjugate retinal plane at the imaging camera. The point source image was distributed over 1.5 pixels of the camera, thus by the Nyquist criterion, any item of the retina of size below 2.7μm was not resolved in the digital image. The cones photoreceptors of 2μm diameter were thus impossible to identify with this imaging system.

7. Light losses: The 50/50 beamsplitter cube which separated the retinal imaging path from the wavefront sensing path was a source of light losses out of the eye, in particular for the retinal imaging path. To maximize the light efficiency of the imaging arm (530nm) while transmitting the maximum of light to the wavefront sensor, a dual wavelength-specific coated dichroic mirror (CVI Melles Griot Long Wave Pass Dichroic Filter, unpolarized) was leading to an improve of 35% to 40% in light efficiency in each channel, all other optics remaining identical.

2.2.3 New system parameter requirements

- Zernike coefficients expression of the wavefront aberration
  With the circular modulation, the sensor signal was directly related to the wavefront aberration gradient in physical units. The non-linearity at the edges of the pupil [42] was not considered as a zero-amplitude of gradient was defined outside the pupil. The signal saturation (non-linearity) occured when the signal always marked one for an increasing aberration. The reconstruction will always show the same value of shape and in turn the same phase at the pupil.
  The wavefront reconstruction from the gradients and its decomposition into Zernike coefficients allowed the calculation of the rms during the experimental session. For comparison of the wavefront aberration amplitude measured at the sensor with the results of commercial instruments (e.g. Zywave aberrometer, Bausch & Lomb, USA), the Zernike polynomials expression is recommended. Since 2002 an international convention has been defined by the Optical Society of America [43] and in 2004 an international standard was defined (ANSI Z80.28-2004) for the reporting of optical aberration of eyes. This normalized convention was also convenient for the communication of results.

- Retinal image resolution and field
  In the system of Liang et al [41, 14] the image resolution was of 0.13arcmin

29

(0.6μm) per camera pixel at the retina, meaning about 10 times the resolution ability of the imaging system described in Section 2.2.1. The photoreceptor mosaic was imaged in a field of 1° located between 1° and 2° from the fovea (or fixation center [19]). The cones cells of 2-5μm diameter in the foveal region were not resolved until the adaptive optics was switched on, and the exact location of the imaged field in the retina was restricted to the cases in which the fixation target was visualized.

The new design of the pyramid wavefront sensor-based AO system attempted to compromise between the necessary increase in the magnification factor γ_T to the value resolving a mosaic of pattern size below 2μm diameter, an image field of subtense including the 2° diameter avascular zone located around the fovea, and a compact optical system size (below the 1.8m×1.5m limits of the optical table). A system in which 1pixel of the camera measured 0.18arcmin (0.9μm) at 635nm wavelength, respected the Nyquist sampling criterion for the cones, as in other systems [17, 44], and provided an image field of $3.5° \times 3.5°$.

- Deformable mirror implementation

  The Mirao52® deformable mirror from Imagine Eyes France presented a $\pm25\mu$m membrane stroke amplitude and a surface flatness of 20nm rms. Based on an electromagnetic actuation, the mirror was numerically assessed as a suitable replacement [45, 46, 47]. It had been incorporated successfully in an AO-fundus camera based at the Quinze-Vingts hospital in Paris, France for clinical trials and commercialized in AO-flash fundus systems and AO-corrected visual simulator, for the correction of ocular aberration during scene visualization. The membrane stroke amplitude has been applied to the correction of very large aberrations such as keratoconic eyes [39]. It was sold for use with a Shack-Hartmann lenslet array and a control software for adaptive optics by the supplying company (Imagine Eyes, France) but required new LabVIEW code to be developed for adaptive optics operation with the pyramid sensor.

- Synchronous acquisition of adaptive optics data and of retinal image

  The use of two independent operating systems, one for the adaptive optics control and one for the retinal image acquisition retrieved a direct acquisition of the double pass point spread function not synchronized with the wavefront sensor data acquisition. Comparison of the direct psf image with a numerical computation based on the wavefront sensor gradients expected to retrieve information lost in the noise of the retinal image instead of using deconvolu-

tion from the wavefront sensor data was thus impossible. This post-processing initially discussed in the context of astronomy later increased retinal images quality [13, 48, 49, 50, 51]. Implementation of the retinal imaging acquisition in the same operating system as the adaptive optics control was thus required.

Several systems were implemented in the aim to fill these requirements. The following report scope was limited to the results useful for the thesis subject. The final system was consequently the most relevant to this purpose.

Chapter 3

Pyramid wavefront sensing

This chapter describes the implementation of the measurement of an aberration with the pyramid wavefront sensor with a circular modulation. The sensor used in this thesis was built for the measurement of large aberrations at the pupil of the human eye. The laboratory implementation, calibration of the sensor measurement and of the wavefront reconstruction are presented in the following.

3.1   Pyramid wavefront sensing in astronomy

In 1996 Ragazzoni [52] introduced a new type of wavefront sensor for astronomy which was based on a pyramid prism. Despite its mechanical complexity, this sensor has an adjustability of its dynamic range, a better photon efficiency, and better results in closed loop compared to the classical Shack Hartmann in a quad-cell configuration. Recent advances in algorithms can address now the saturation limit and centroiding issues [53, 54] in many of today's Shack Hartmann systems. The first drawback of the pyramid is mechanical, as the pyramid prism is very difficult to manufacture compared to lenslet arrays, and is not commercially available despite the recent technological advances in this domain [55, 56, 57, 58]. The second drawback is related to the modulation requirement for getting a quantitative slope measurement with the sensor [59, 30].

The pyramid sensor principle is related to the Foucault knife edge test (1859, [60]) in that both techniques split the beam at or near the focal plane of the wavefront or ele-

ment to be tested. In consequence the pyramid sensor could be seen as a 'focal plane' or 'Fourier-plane' sensor. However, the aberration determination is not obtained by translation of the knife perpendicular to the propagation axis but by comparing the intensity of the beam parts detected after splitting by the prism edges. Each part of the beam is diverted by the prism so in the reconstructed pupil plane a single frame is sufficient to characterise the wavefront aberration instead of having to process the reconstructed pupil for multiple positions of the knife-edge near the focus. As the analysis is performed using a detector placed in a conjugate pupil plane for the wavefront to be tested, the pyramid sensor is thus effectively a 'pupil plane' wavefront sensor. The pyramid retrieves a wavefront slope measurement equivalent to that of a Shack-Hartmann physically placed in a conjugate pupil plane.

As the division of the beam focus is made by the 4 facets of the prism, the pyramid is said to be equivalent to a Shack Hartmann sensor in a quad-cell configuration. The quad-cell advantage is a lower read-out noise in the sensor due to the lower number of pixels to read in the detector [61] and does not require access to the wavefront spot size behind the lenslet. One possible solution proposed to increase the number of pixels for the detection was to use an array of pyramids instead of a single prism and to relay each pyramid to the pupil plane of the camera using lenslets [59]. However further work showed the optimal number of lenslets in the focal plane was a 2x2 arrangement, similar to using the pyramid prism [62]. Using a 2x2 lenslet array retrieved comparable atmospheric turbulence values as with a quad-cell Shack Hartmann [63], and the influence of the lenslet array edges quality for successful operation was highlighted. This system also showed a lower error propagation than its equivalent lenslet array in closed loop [64]. Comparative turbulence measurements were also performed with this 4-lenslet pyramid using the static modulation approach [65].

Mechanical modulation of the prism or of the beam is required in theory to measure quantitative wavefront slopes from the sensor signals [52,66,67] and to provide in-situ adjustment of the sensor 'gain' or sensitivity. In astronomy the mechanical modulation may not be necessary as the residual atmospheric turbulence contains a 'natural' modulation term [68,69] and thus after appropriate calibration the sensor signal still retrieves a wavefront gradient measurement [70], and provides a good adaptive optics efficiency even in poor seeing conditions [71]. Circular modulation provides a comprehensive framework for the implementation of the wavefront reconstruction but is perhaps not essential for pyramid sensing in the eye [72], due to natural eye

movements. The effects of natural aberration dynamics such as accommodation and pupil diameter are however limited in ophthalmic applications by cyclopegic drugs. Other effects to be considered are due to periodical change in the orientation of the retina of the order of the tens of milliseconds. These natural eye saccades responsible for ocular blur might provide a pupil drift around the central point of the eye and modify the ocular aberrations similarly as the inherent turbulence in the atmosphere.

Algorithmic solutions have also been developed for the unmodulated pyramid in astronomy introducing a wavefront reconstruction scheme based on a Jacobian decomposition of the mirror modes instead of the classical singular-value-decomposition scheme. This was used successfully in closed loop [73, 74] to increase the dynamic range of an adaptive optics system. Another replacement for the mechanical modulation is based on the use of fixed-divergence diffusers (holographic or rotating type) which are placed in a conjugate pupil plane before the pyramid [75], then the point spread function (psf) size at the pyramid provides the sensor sensitivity adjustment [72]. This static modulation has been implemented in layer-oriented multiconjugate adaptive optics [76, 75, 77] using double pyramids to better control the output direction after the pyramid [78] for the ELT and in ophthalmic applications [72].

The pyramid measurement has been studied [79] to explain how the slope or the phase of the wavefront measurement depends on the modulation amplitude considered, in the circular modulation scheme. When compared to a Shack-Hartmann in quad cell configuration with weighted center of gravity algorithm [80] and beam filtering [81], the pyramid was estimated to perform similarly [82] in high photon flux. This confirmed the previous numerical results [83, 67] predicting a better closed loop efficiency of the pyramid for low-magnitude natural guide stars and was recently confirmed experimentally, this time without mechanical modulation [71].

To confirm the simulation results between the pyramid and the Shack Hartmann a special program has been developed and is currently in progress on the high-order testbench (HOT)-ELT (First Light AO system for the Large Binocular Telescope) [84, 57, 85, 86]. One advantage of the pyramid sensor compared to the Shack Hartmann is however that it allows the measurement of positioning errors (differential piston) in the individual segments of this telecope mirror [87, 88]. For this category of extremely large telescopes the question of the maximal Karhunen-Loeve mode that can be corrected and by which way is often raised. Those systems also seem to present an optimal modulation ratio [89] for a specified guide star size which would thus open

new perspectives such as a possible use with laser guide stars [83].

In ophthalmology, open loop measurement is of major importance in applications such as laser refractive surgery. The pyramid sensor is usually considered as a poor system for the determination of the refraction (i.e. focus error). The closed loop effectiveness of wavefront sensors in adaptive optics systems is mainly related to high resolution retinal imaging. This research was initiated by Liang, Miller and Williams in 1997 [41,14] after they produced with adaptive optics the first in-vivo high-resolution imaging of the photoreceptor cells in the human eye. Further developments of this work showed efficient identification of the functional role of photoreceptors in color vision [22], leading the way to the development of adaptive optics use in imaging of the neuronal activity of the retina.

Although Shack-Hartmann wavefront sensors are widely used today in ophthalmic research instruments, pyramid sensors have been implemented for the eye, firstly by Iglesias and Ragazzoni [72] using the probe beam size at the retina to set the dynamic range and rotating diffusers to replace the mechanical modulation, or in closed-loop configuration using the conventional circular modulation scheme [1, 90, 91, 92, 93]. In this work we tried to implement a sensor of large enough dynamic range for description of various ocular aberrations and still able to retrive very accurate measurements for closed loop operation.

3.2   Wavefront sensing with a pyramid prism

The following section discusses the implementation of the pyramid wavefront sensing in an ophthalmic system. The use of several approximations and compromises is required. In contrast to the Shack-Hartmann, the pyramid does not rely on centroiding algorithm for obtaining a wavefront measurement. The aberration is directly calculated from the 4 wavefront pupil images at the camera. The price for this computational simplicity however stands in the difficulty of mechanical implementation, and of identification of the sensor saturation limit during experimental sessions.

3.2.1   Wavefront pupil reimaging into 4 sub-pupils

A focusing beam onto the pyramid is divided in 4 parts by the prism facets as illustrated in Figure 3.1a. In that case however the divergence β is defined towards the

on-axis ray, and the rays defining β become principal rays for the rest of the system.

For calibration of the pyramid divergence β, an on-axis collimated beam of 10.5 mm diameter was sent onto the pyramid as represented in Figure 3.1b. For such a configuration the divergence β is given by:

$$\beta = 2 \times \arctan\left(\frac{h}{d}\right) \tag{3.1}$$

Equation 3.1 means that at a distance (d) from the prism the spacing (2h) measured between the centers of the 4 beam quadrants is resulting of the incident collimated beam split by the pyramid facets.

From the measurements of (2h) with a collimated beam at multiple distances (d) from the prism we obtain the graph in Figure 3.1c using Equation 3.1. Measurements at a close distance are visibly subject to a high variability but their mean value over the distances considered are consistent with a long distance measurement; thus we estimate that for our case $\beta_{mean} = 2.51° \pm 0.01°$ is a good approximation for the value of the divergence.

Riccardi [94] showed that the prism vertex angle (γ) relates to the divergence (β) following the geometrical optics for the refraction of a of a ray parallel to the optical axis. Within the [-6, 6°] limits of the geometrical optics approximation:

$$\gamma = \frac{\beta}{(n_{glass} - 1)} = \frac{2.51}{(1.5157 - 1)} = 4.86° \pm 0.02° \tag{3.2}$$

The value of γ is determined from the measured value of β and from Equation 3.2. This show our measurement is consistent with the value of 5° presented in the literature for this pyramid which comes from astronomy [94, 66].

In Figure 3.1a, the angle β defines the angular separation between the pupils centers. To obtain separation of the pupils for a focusing beam in the general case the F-number of the beam must be higher than a critical value F_c. If overlap of the pupils is detected the pupil gradient calculation cannot be performed. At the critical F-number, 2 pupils sides are just in contact but do not overlap. Diagonally the pupils centers angular separation is $\beta' = \sqrt{2}/F_c$ [94]. From the prism divergence, we thus define the critical F-number for the maximal density packing configuration as F_c and derive the
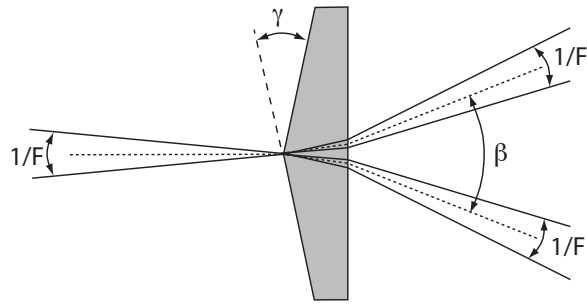
(a) Divergence, Focusing beam
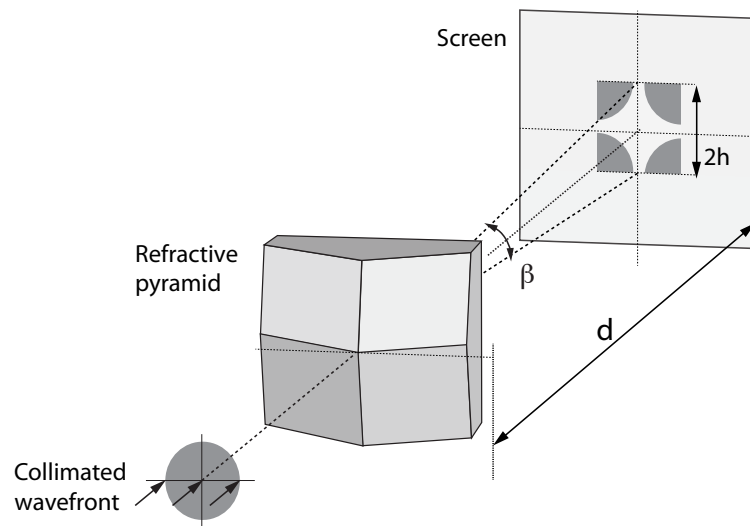
(b) Divergence, Collimated beam
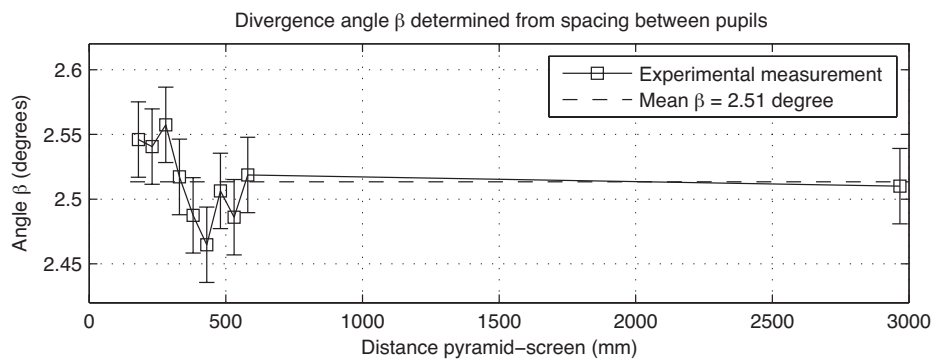
(c) Divergence angle β (in degrees) of the prism from experimental measurement of the pupil center - to - center spacing

Figure 3.1: Vertex calibration measurement

37

constraint on the beam F-number for a given pyramid prism:

$$\beta = \gamma \left(n_{glass} - 1 \right) \tag{3.3}$$

$$F \geq \frac{\sqrt{2}}{\beta \prime} = F_c = \frac{1}{\beta} \tag{3.4}$$

Equation 3.3 and Equation 3.4 define the critical F-number for which the pupils overlap is avoided for the prism considered, that is the limit F_c under which no wavefront sensing can be performed. For the divergence measured after Equation 3.2 the limit F-number is thus:

$$F_c = \frac{1}{[(\frac{4.87\pi}{180})(1.5157 - 1)]} = 22.8131 \approx 23 \tag{3.5}$$

Equation 3.4 will be used further as a criterion of successful alignment when considering the pyramid pupils, in Section 3.2.2.2.

Mechanical constraints, such as the housing of the camera which does not allow very short reimaging focal lengths and the finite size of the optical bench limit the use of lenses of focal above 600mm length. The camera pupils must also follow the sampling requirement for adaptive optics. In this system, to be Nyquist sampled at the wavefront sensor camera highest binning, we must have at least 16 pixels across each pupil. To satisfy the mechanical and sampling requirements, we built the system using an input beam f-number of 69.5. This is about twice the F-number value for the optimal packing for this pyramid but consists in an acceptable compromise between the pupil sizes and the available optics.

Discussion of the design

Considering the reading time of the camera chip is constant, the trade off stands in between having many wavefront samples and a dense packing or a sufficient number of pixels and a clear separation between the pupils. Furthermore, this separation allows adjustments in high f-number cases which would modify the pupils spacing or adjustments for higher pupil diameters. The F-number at the pyramid defines also the sensitivity range of the sensor. With the modulation this parameter becomes a scaling factor for the sensitivity range, but for an unmodulated beam the F-number should be chosen also accounting for the sensitivity range it defines towards the wavefront sensing.

3.2.2   Modulation

Even if the modulation is perhaps not essential for pyramid sensing in the eye [72] as the inherent aberrations act as the inherent turbulence in the atmosphere [68], it is convenient to work with a circular modulation [66]. As we will see in the following section, the modulation determines the maximal wavefront aberration amplitude sensed in the system. Providing the mirror stroke is sufficient to correct it, the adjustability of the sensing range allows an accurate measurement of the eye aberration while maintaining the benefit of adaptive optics for the retinal imaging.

3.2.2.1   Circular modulation at the pyramid

For a collimated wavefront propagating along the optical axis in the 4-f system formed by the lenses (L1) and (L2), placing the pyramid prism in the plane of the mixed focus divides the focal spot between the 4 facets of the pyramid, as illustrated in Figure 3.2a.

(a)

(b)
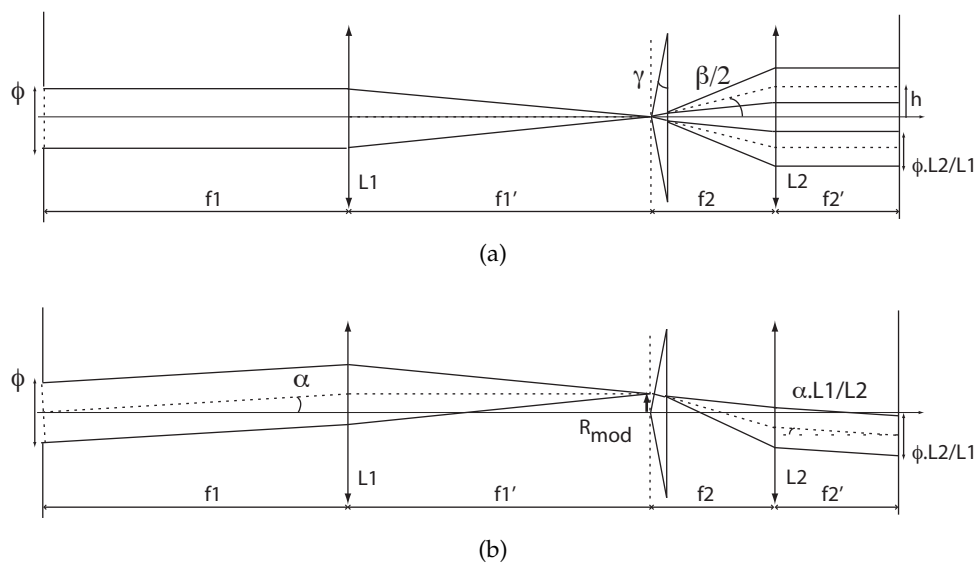
Figure 3.2: Modulation implementation for the pupils conjugation: at the steering mirror plane the diameter of the pupil Φ and the focal length of the lens (f_1) define the amplitude of the modulation radius R_{mod}.

In this 4-f system, the focusing lens (L1) and reimaging lens (L2) conjugate the steering mirror pupil plane to the wavefront sensor camera pupil plane. The size of the wavefront sensor camera sub-pupils is similar to the size of the pupil if the pyramid prism was removed given the beam F-number is not modified before and after the pyramid. The pupil positions at the wavefront sensor camera are defined by the di-

vergence after the prism as detailed in Section 3.2.1 and Figure 3.2a. If the modulation is represented as a tilt angle α applied along the vertical axis (Y) at the steering mirror, as in Figure 3.2b, the focused beam is shifted by a value ($R_{mod} = f_1' \tan \alpha$) at the pyramid. The more the incident beam position increases at the pyramid the stronger the deviation applied to the beam by the prism, thus the wavefront sensor camera pupils positions remain constant - until the modulation reaches the critical deviation angle for the prism.

If the modulated beam at the steering mirror is tilted of an angle ($+\theta$) towards the optical axis, the corresponding transverse aberration in the pyramid plane is a focus shift of ($+\Delta y$). When the modulation projects the focus on the upper part of the pyramid, in Figure 3.3a for the angle ($+\alpha$), the wavefront tilt and the modulation angle subtract thus the focus is shifted of (-Δy) in the pyramid plane.

(a)

(b)
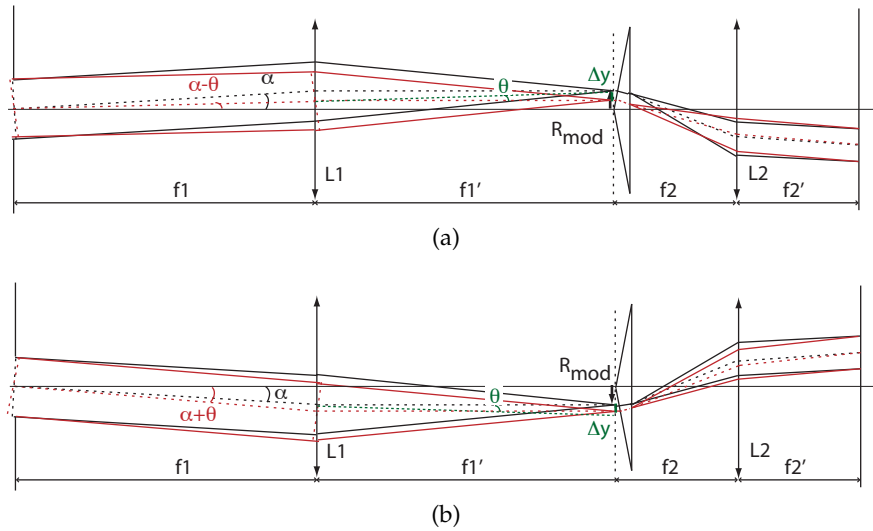
Figure 3.3: Modulation in telescopic arrangement

When the modulation projects the focus in the lower part of the pyramid in Figure 3.3b for the angle ($-\alpha$), the wavefront tilt and the modulation add thus the focus is shifted of (-Δy) in the pyramid plane. In consequence the optical path becomes non-uniformly distributed amongst the 4 pyramid facets as in Figure 3.4 (left).

The signal at the wavefront sensing camera for the circular modulation S_y is given by the difference in the optical path traced by the shifted circle onto the pyramid top and down facets:

$$S_y = \frac{b_2 - b_1}{2\pi R_{mod}} \tag{3.6}$$

40
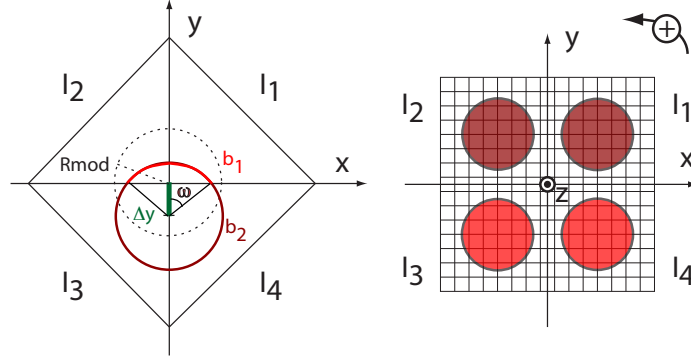
Figure 3.4: Modulation path, positive tilt of θ. The conjugated pupils at the camera plane receive more light in the direction containing the longest optical path, represented here by a darker red shade in the top pupils.

in which the optical paths (b_1 and b_2) are expressed using the cosine of (ω) for the modulation circle after the beam is tilted:

$$
\begin{cases}
b_1 = 2\omega R_{mod} \\
b_2 = 2R_{mod}[\pi - \arccos \frac{\Delta y}{R_{mod}}]
\end{cases}
\tag{3.7}
$$

Replacing the terms for b1 and b2 from Equation 3.7 into the sensing expression in Equation 3.6, and developing we obtain an expression of the sensing signal S_y in function of the transverse aberration Δy:

$$
\frac{\Delta y}{R_{mod}} = \sin\left(\frac{\pi}{2} S_y\right)
\tag{3.8}
$$

Equation 3.8 is the form that will be used in Section 3.3.1 in the development of the sensor signal study for the case of a local tilt presented by a single wavefront element.

The modulation amplitude R_{mod} is usually a factor of the minimal modulation factor $R_{mod_{MIN}}$, which is the extend of the focused spot in the pyramid plane. As in Shack-Hartmann systems this is a criterion of sensitivity range for the sensor. $R_{mod_{MIN}}$ is the Dawes' resolution criterion for 2 stars separated of (λ/D) in astronomy and is the Rayleigh (Airy) resolution limit in imaging.

$$
R_{mod_{MIN}} =
\begin{cases}
\lambda f \ / \ D & \text{Dawes} \\
1.22\, \lambda f / D & \text{Airy}
\end{cases}
\tag{3.9}
$$

41

In the following the modulation factor was mainly expressed in terms of the Dawes criterion, which was convenient for comparison with the majority of the literature on pyramid wavefront sensing.

3.2.2.2 Laboratory implementation of the circular modulation

This section presents the optical system used for calibration of the sensor signal in Figure 3.5 and its modifications for the optical design software, calibration of the modulation amplitudes in Figure 3.6a.
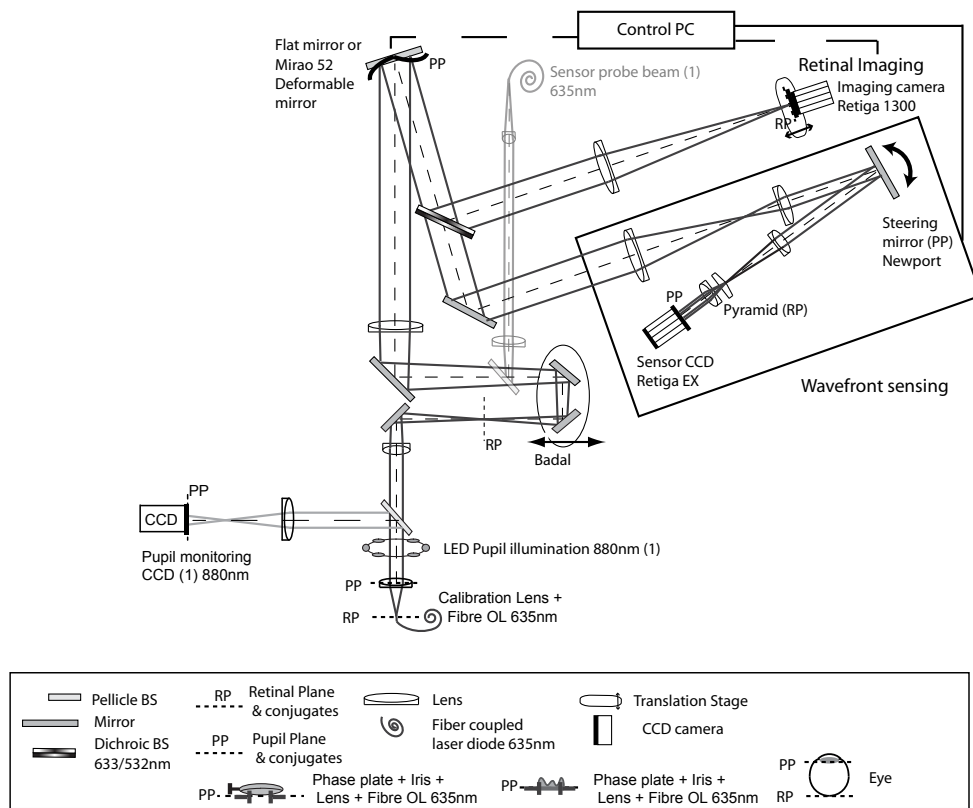
Figure 3.5: Schematic of optical bench used for calibration of sensor signal. Modification of the pupil illumination optics was performed for closed loop calibration and use in the 5-subjects aberration measurement and psf imaging of Chapter 4.

System description

The wavefront sensor calibration beam was defined at the pupil plane of the eye by a fibre laser source output collimated by a 100mm achromat lens and an iris aperture of 6mm diameter. A telescopic assembly conjugated the pupil plane to the deformable mirror through the Badal optometer mirrors stage set at mid-position of translation range. A pellicle beamsplitter defined the input of the wavefront sensor probe beam

focusing into the Badal stage further described in Chapter 4, Section 4.2.4. The magnified collimated calibration beam at the deformable mirror was reflected towards the wavefront sensor path. A second telescope assembly conjugated the pupil plane at the deformable mirror to the modulation control steering mirror. A dichroic beamsplitter defined the starting position of the psf and retinal imaging optical path. A last telescope assembly formed by a focusing lens and a reimaging lens placed after the pyramid sensor relayed the steering mirror pupil plane to the wavefront sensor camera.

The implementation of circular modulation was provided in the pupil plane of the focusing lens by a steering mirror (Newport FSM-300 Fast Steering mirror). This plane mirror surface was tilted horizontally and vertically with an amplitude defined by coupled galvano-actuators located underneath its surface. The surface deviation amplitude was determined by the voltages sent to the mirror amplifier by two synchronized function generators (Agilent waveform generators 33250A and 33120A), and was limited by a cut-off frequency above which the mirror response was attenuated. 90° out-of-phase sinusoidal signals of the same frequency provided an elliptic modulation of the focus at the pyramid. The signal frequency was the inverse of the integration time of the wavefront sensing camera to obtain a signal at the sensor [66].

Adaptation to the calibration of the modulation

The wavefront sensor optical system was reproduced in Zemax using the manufacturer's specifications for the lenses parameters, physical mirrors apertures and light sources wavelengths. The adaptation to the modulation calibration for a Zemax design sketch is presented in Figure 3.6a. Replacing the pyramid by an empty plane cancelled the beam deviation by a single facet. Replacing the reimaging lens by an empty element cancelled the steering mirror pupil plane conjugation with the wavefront sensing camera. Appropriate positioning of a pinhole in the telescope path between the deformable mirror and the steering mirror formed a finite size modulated image of the pinhole at the wavefront sensor camera. For a common voltage amplitude and a 90° phase shift between the function generators, the pinhole image initially formed an ellipsoidal shape onto the camera. Experimental adjustment of the steering mirror voltages and function generators phase offset was performed to define the modulation circle at the pyramid as in Figure 3.6b.

The centre of the circle defines the beam propagation direction similar to that of the 4-f system. The cross section intensity profile in Figure 3.6c identifies the pinhole image

43

Deformable mirror
(`flat' commands)

Steering mirror

Pinhole

Cube
Beamsplitter

Focusing lens

Pyramid (empty)
Reimaging lens (empty)
Wavefront sensing camera (image)

Badal optometer
translation stage
(mid-range of travel)

Calibration lens

Calibration laser
(centered point source)
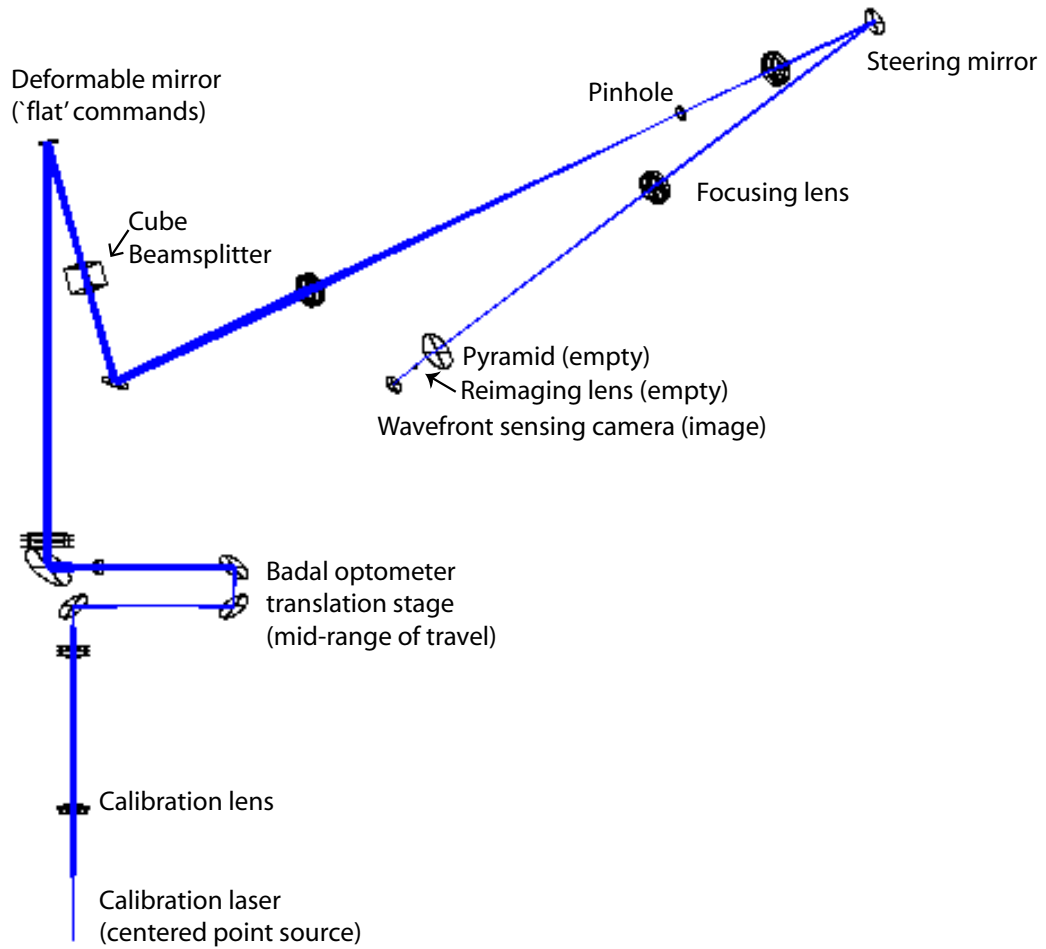
(a) Zemax 3D layout for definition of the modulation voltage amplitudes. Beam collimation between the deformable mirror and the focusing lens before the steering mirror is preserved contrarily to the displayed divergence which is related to the design export settings.
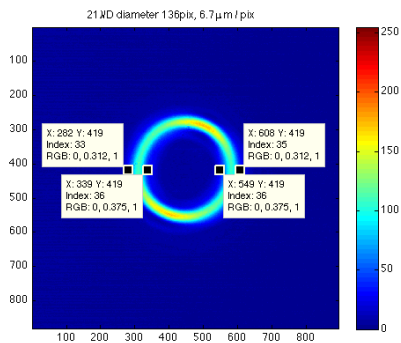
(b) Experimental CCD frame
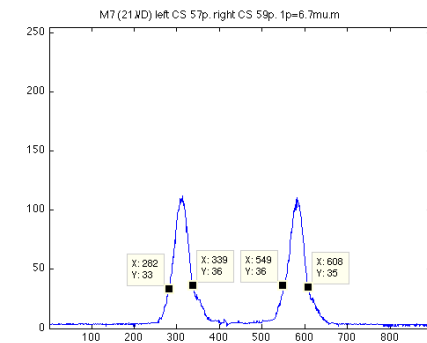
(c) Matlab cross section over the ccd frame

Figure 3.6: Zemax optical design and experimental results for the modulation factors, see text for details

44

width and the circle radius as the beam height at the pyramid plane. With 268 pixels between each side of the peak intensities in the cross section, the circle diameter is 2.2% less than the value of the design, thus the modulation voltages are calibrated. Repeating this procedure for the vertical direction and for other modulation amplitudes insures that the beam modulation is appropriately defined towards the optical design. Table 3.1 presents the experimental results of the voltages adjustments defining the circular modulation.

Table 3.1: Notations used for the modulation circles. The modulation radius at the pyramid is defined by the steering mirror surface deviation.

Parameter	Set #1	Set #2	Set #3
Radius (in $\times R_{Airy}$)	7	17	27
Radius (in $\times \lambda/D$)	9	21	33
Factor (in theory $\times$ 100mV)	(3, 3)	(7, 7)	(11, 11)
Angle (theory, $\times$100mV.2,62mrad.V^{-1}.180/π in deg.)	0.045	0.105	0.165
Factor (in practice (X,Y)$\times$100mV)	(2.1, 2.4)	(5.1, 5.9)	(8, 9.5)
Circle diameter, (in pixels, experimental)	118	274	430

A common center is defined for all the modulation amplitudes. The function generators voltages and phase adjustment is performed in order to image each circle according to its definition as in Figure 3.6b using the overlay tool at the camera using the Labview controls.

Positioning the pyramid

When inserting the pyramid prism and the relay lens in the optical system the modulation circles and the region of interest defined by the 4-pupils must share the same center onto the camera. This ensures that the optical assembly formed by the pyramid, reimaging lens and camera is aligned onto the optical axis of the system. The distance between the pyramid and the reimaging lens are aligned on a separate arm using a collimated beam, with the pinhole images repositioned onto the modulation circles center via transverse (X-Y) adjustment of the reimaging lens.

Pupil diameter

Either the laser power is lowered or alternatively a neutral density filter is added at the edges of the focusing lens so as to obtain a gray level clearly distinguishable from the background in the pupils (about $>$ 150 / 255) without saturation. Each of the 4 sub-pupil diameter is verified at $\pm$1 pixel on the frame using the Labview 'rectangle' overlay tool. This value must be constant for multiple modulation amplitudes. Another verification of the pupils diameters in pixels is performed when defining the

common mask for the sensing from the thresholded camera image, in Figure 3.7.

Pupil spacing
Locating the center of each of the sub-pupils in all modulations and pupil samplings considered, the spacing between the pupils is reinjected in Equation 3.3 using for (d) the focal length of the reimaging lens and n=1.5157. An experimental vertex angle is measured from the image camera.

Mask definition
Each pupil position on the CCD sensor is defined from an 8-bit thresholded ccd frame with respect to the frame reading indexing direction as on Figure 3.7.
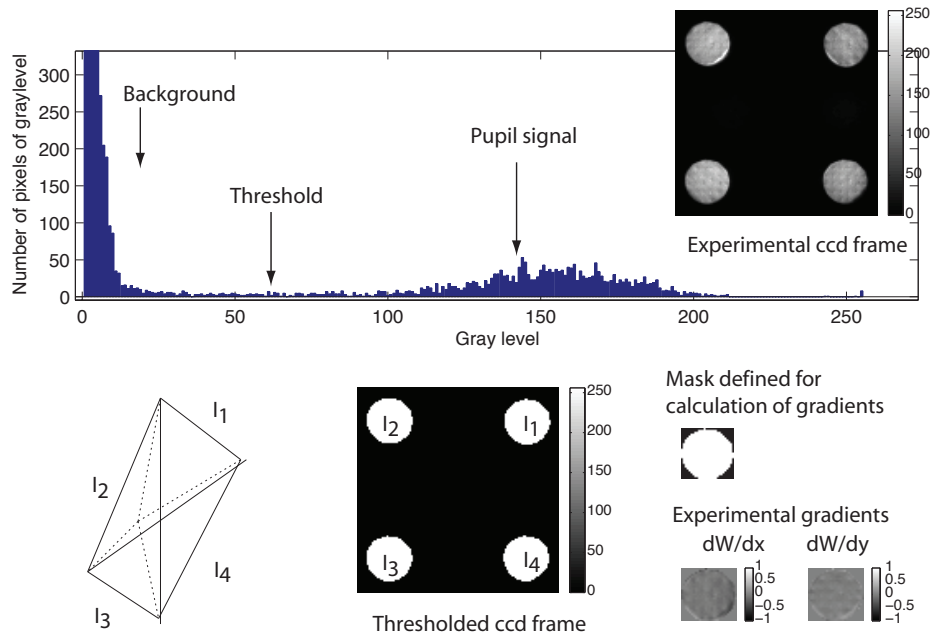
Figure 3.7: Sensing mask definition procedure, example with Binning 2, modulation 21 λ/D

The threshold is manually chosen at the level which differentiates the pupil signal from the background signal. A pupil signal of at least half of the camera graylevel scale (128 for an 8bit depth image) is preferable. Each pupil location on the camera frame is stored and indexed with regards to the wavefront sensing definition, as in the frame histogram of Figure 3.7. The pupil mask is the result of the nonzero pixels common to the 4 sub-pupils in the thresholded image. It is defined as much as possible for each modulation and each binning setting in our software to take into account the change in sensitivity with the modulation amplitude. The drawback of this method is that in low modulation amplitudes the pupils contour deteriorates and

it is better to use a mask defined in median modulation.

Pupil intensity balance

From the theory in Section 3.2.2.1, Equation 3.6, the sensor signals for a flat wavefront should be only composed of zeros given the equal distribution of the signal over the 4 facets of the prism. Due to the noise in the system instead the gradient signals spread around the zero-value into a Gaussian shaped curve as seen from Figure 3.8. As the 'flat' wavefront described here is taken as reference for further calibration of the influence functions for the closed loop the sensor must see it as free of aberration as possible. If the pyramid is not well centered on the modulation circle the gradients signal distribution is decentered from the zero, which is for the sensor equivalent to a wavefront tilt. The centering of the sensor signals thus define a 'flat' reference used as closed loop convergence criterion stability. For an open loop measurement this wavefront can be used as reference in subtraction only if the aberrated surface is placed in the pupil plane of the calibration arm. For ocular measurement however there would be no possible comparison, given the source of the sensor signal at the retina presents a different initial definition and is subject to different noise characteristics than the calibration wavefront.

An approximation of the magnitude of the signal deterioration due to the noise can be obtained by fitting the sensor signal to a Gaussian function. The characteristics of the fit contain information on the quality of the calibration in relation to the sensor pupil sampling and signal accuracy. The distributions of sensor signal for each orientation (horizontal and vertical) per pupil sampling (1-4) and modulation amplitude ($9\text{-}33\lambda/D$) is displayed in Figure 3.8. A single camera frame is considered, the sensor signal calculated from this frame for a pixel is counted as part of one of the 41 intervals of 0.05 width over the [-1:1] full interval of possible sensor signal values. Each histogram is normalised by the maximal number of counts and averaged over all the binnings. The resulting plot in Figure 3.8 represents the distribution profile for the three tests modulations, averaged over the pixel size in both directions. It can be approximated by a gaussian which standard deviation at the $1/e^2$ of the maximal intensity would be $\sigma \approx 0.1$.

The widening of the distribution around the maximal value for the small modulation amplitude is expected as the higher signal sensitivity of that dynamic range to small wavefront aberrations. For higher modulations the loss in signal sensitivity returned a signal similarly approximated to a Gaussian profile which standard deviation at
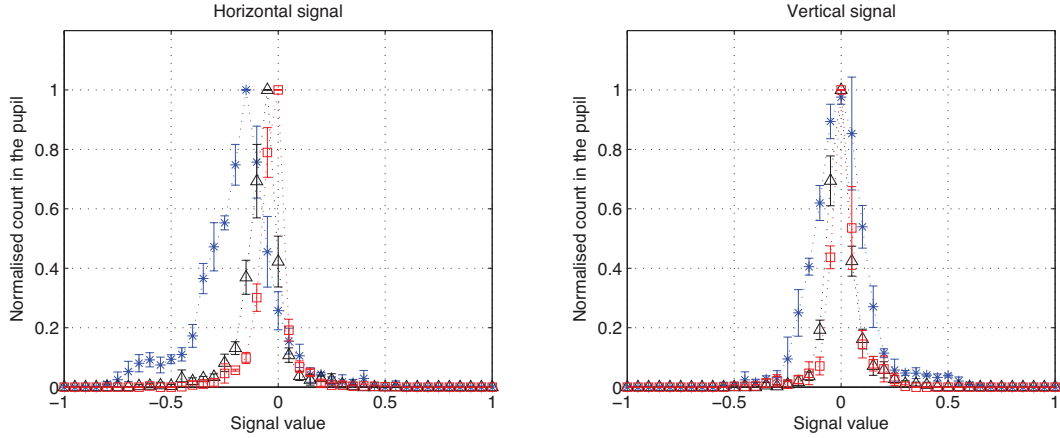
Figure 3.8: Distribution around zero value for flat wavefront, averaged over the binnings. Plots colors note respectively: $9\lambda/D$ in blue asterisks (*), $21\lambda/D$ in black triangles ($\triangle$), $33\lambda/D$ in red squares ($\square$)

the $1/e^2$ of the maximal intensity would be $\sigma \approx 0.06$. This lower value of standard deviation means a better uniformity in the pupil signal is reached than in the small modulation.

3.3   Sensor calibration

This section establishes the steps followed to obtain the reconstruction of the ocular wavefront and its decomposition in Zernike modes from the sensor signals defined in our system.

3.3.1   Sensor signal for circular modulation

In the general case, the local slope of the aberrated wavefront compared to the spherical wavefront is two-dimensional but is reduced here to a one-dimensional case. Figure 3.9 is used for the main derivation of the wavefront aberration obtained from the sensor signal in Equation 3.10 for a centered lens case. The aberration considered is the global wavefront tilt from the spherical wavefront. A perfectly spherical wavefront $[W_0(x,y)]$ and the same wavefront $[W_1(x,y)]$ uniformly tilted at the angle θ with regards to the propagation axis (vertical tilt) are represented. Both wavefronts are perfectly spherical thus the angle between the rays from the pupil plane to the pyramid is preserved at the pupil center $P_0=P(x=0,y=0,z=0)$ and whatever the pupil point $P(x,y,z)$ considered.
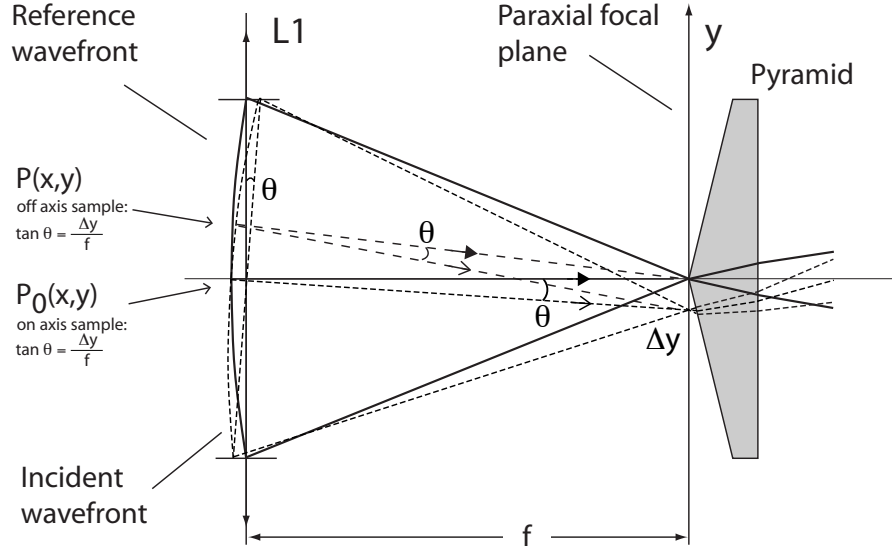
Figure 3.9: Spherical wavefront tilted of θ towards the propagation axis

The aberration calculation described in the following is illustrated in Figure 3.9. In the practical implementation the modulated beam was circling around the lens center, but the transverse aberration Δ_y and gradient of the aberrated wavefront $W_1(x,y)$ are of similar amplitude as in the centered case and the maximal modulation did not occupy the upper parts of the lens that would have added wavefront distortions.

Considering any wavefront $[W(x,y)]$ can be decomposed into elementary sources due to the principle of superposition of waves, we can express $[W(x,y)]$ as the sum of elementary wavefront samples (dW) located at positions $[P(x_i,y_j)]$ in the 2-D reference space. The orientation and normal vector of each elementary surface (dW) obtained by vectorial projection onto the 2-dimensional (X,Y) discretized space of elementary size (dxdy) characterizes the wavefront propagation. We can thus express in the discretized space the continuous wavefront $[W(x,y)]$ with

$$W(x,y) = \sum_{i=1}^{N_x}\sum_{j=1}^{N_y} W_P(x_i,y_j)\, dx\, dy \qquad (3.10)$$

with (N_x, N_y) the row and column number of the pixel W_P considered in the mask. Assuming the lens (L1) is focusing both wavefronts in its paraxial focal plane, $[W_0(x,y)]$ converges towards the center of the paraxial focal plane and the tilted wavefront $[W_1(x,y)]$ converges towards a point which is shifted of Δy in the same plane.

49

At the center of the pupil in P(x=0,y=0,z=0) the relationship

$$\Delta y = f \tan(\theta) \tag{3.11}$$

describes the transverse ray aberration in the pyramid plane for the tilted wavefront. For any wavefront element $[P(x,y)]$ of the pupil, the angle between the normal to the tilted wavefront $[W_1(x,y)]$ and the normal to the spherical wavefront $[W_0(x,y)]$ is (θ). The transverse ray aberration Δy defined in Equation 3.11 for the central point P_0 of the pupil is thus constant over the whole surface of the tilted spherical wavefront. At any $[P(x,y)]$ of the plane, the wavefront gradient is :

$$\frac{\partial W_1(x,y)}{\partial y} = \tan \theta \tag{3.12}$$

By using 3.12 into 3.11, we can relate the wavefront gradient to the transverse ray aberration :

$$\Delta y = f \frac{\partial W_1(x,y)}{\partial y} = f \tan(\theta) \tag{3.13}$$

We know from the use of circular modulation that the integrated signals s_x, s_y at the detector are linked to the transverse aberration Δy (originated from the tilt θ) by Equation 3.8 which we write here:

$$\Delta y = R_{mod} \sin\left(\frac{\pi}{2} s_y\right) \tag{3.14}$$

As Equation 3.13 and Equation 3.14 are equal, we obtain a relationship between the sensor signal in the vertical direction $s_y(x'_i, y'_j), (i = 1 : N_x, j = 1 : N_y)$ and the tilt presented by $W_1(x,y)$.

As the tilt is continuous and constant over W1, this gives using Eq. 3.10 into Eq. 3.12 and for $\tan(\theta)$:

$$\frac{\partial W_1}{\partial y} = \sum_{i=1}^{N_x}\sum_{j=1}^{N_y} \frac{\partial W_{P1}(x_i,y_j)}{\partial y} = \sum_{i=1}^{N_x}\sum_{j=1}^{N_y} \tan(\theta_{ij}) = \tan(\theta) \tag{3.15}$$

As the sensor signal is composed of all the signals of the pupils, from Eq. 3.10, the conjugated pupil plane can be discretized into (N = i x j) wavefront samples, we can

write for the ensemble of the conjugated pupil elements

$$\sum_{i=1}^{N_x}\sum_{j=1}^{N_y} \frac{\partial W_{P(x_i,y_j)}}{\partial y} = \sum_{i=1}^{N_x}\sum_{j=1}^{N_y} \tan(\theta_{ij}) = \sum_{i=1}^{N_x}\sum_{j=1}^{N_y} \frac{R_{mod}}{f} \sin\left(\frac{\pi}{2}s_y(x_i',y_j')\right) \qquad (3.16)$$

This relationship also expresses that the wavefront secondary sources are well described by the ensemble of local tilts θ_{Pij} given by the sensor signals obtained from the intensity in the detector region corresponding to P.

In the following, Eq. 3.16 in its single-element version will be the one mainly used to describe the relationship between a local wavefront departure and the sensor signal considering that any local wavefront departure from the 'ideal' spherical wavefront at $[P(x,y)]$ can be decomposed into 2 independently tilted elements.

This will lead to consider that any wavefront gradient at the conjugated pupil plane can be written by its decomposition:

$$\frac{\partial W_P(x,y)}{\partial i_{(i=x,y)}} = \frac{R_{mod}}{f} \sin\left(\frac{\pi}{2}s_{i,(i=x,y)}(x',y')\right) \qquad (3.17)$$

In general, the wavefront aberrations are not uniform over the pupil aperture, which creates the discrepancies of intensity distribution in the conjugated pupils at the ccd. Equation 3.17 however applies to each pupil element $(i)_{(i=1,N_{samples})}$ which leads to a distribution of wavefront aberrations θ_i and transverse aberrations Δy_i.

The sensor signal s_y is obtained by vertical differentiation of the detector pupil intensities $(I_i)_{(i=1,4)}$ for the pixel conjugated with $P(x,y)$ from development of Equation 3.6:

$$s_y(x',y') = \frac{[I_1(x',y') + I_2(x',y')] - [I_3(x',y') + I_4(x',y')]}{I_1(x',y') + I_2(x',y') + I_3(x',y') + I_4(x',y')}$$

The expression is similar for a tilt in the horizontal direction with the horizontal wavefront gradient $[\partial W(x,y)/\partial x]$ with this time s_x :

$$s_x(x',y') = \frac{[I_1(x',y') + I_4(x',y')] - [I_2(x',y') + I_3(x',y')]}{I_1(x',y') + I_2(x',y') + I_3(x',y') + I_4(x',y')}$$

We see that the sensor saturation occurs when the signal $s_i(x',y')$ reaches ± 1, that is

when the wavefront tilt displaces the signal onto only 2 facets of the prism.

In that case the aberration Δy of Figure 3.4 is larger than the radius of modulation R_{mod}, and in turn the sensor detects a zero-signal in the top (I_1=0),(I_2=0) pupils and a maximal signal in the down ones: (I_3=I_{max}), (I_4=I_{max}).
Hence :

$$
\begin{cases}
s_x(x,y) = \frac{[0+I_{max}]-[0+I_{max}]}{0+0+I_{max}+I_{max}} = 0 \\
s_y(x,y) = \frac{[0+0]-[I_{max}+I_{max}]}{0+0+I_{max}+I_{max}} = -1
\end{cases}
$$

This limits to s_{xy}=[-1,1] the range of values retrieved by the sensor, and means the saturation is occurring when the range boundaries are reached.

Reversing Equation 3.17, using the angular equality of Equation 3.16 we can access the sensor signal s_{xy} for a given tilt θ_t which defines arcsine(θ_t) $\leq |\pi/2|$. Outside these boundaries for higher angles Matlab defines complex numbers which, approximated by the equality arcsine(θ_t) = $|\pi/2|$ describe the sensor saturation. Equation 3.18 shows the theoretical sensor signal for an uniform tilt of the spherical wavefront is constant over the pupil.

$$
s_{xy} = \frac{2}{\pi} \arcsin\left[\frac{f}{R_{mod}} \tan(\theta_{ij}) \right]
\tag{3.18}
$$

Higher angles correspond to the saturation of the signal. The arcsine function is at $\pi/2$, that is that the angle θ_{ij} projects the modulated beam on a single side of the pyramid:

$$
s_{xy} = \pm 1 \qquad \Leftrightarrow \qquad \tan\theta_{ij} \simeq \pm\frac{R_{mod}}{f}
\tag{3.19}
$$

The sign of the gradients is linked to the tilt direction. Equation 3.19 is consistent with the configuration of saturation described using geometrical optics in Section 3.2.2.1, Figure 3.4. The theoretical signal defined by the tilt amplitude experimentally applied at the pupil of the eye is compared to the mean signal calculated over all pupil samples in Section 3.3.2, Figure 3.10.

3.3.2 Sensitivity range of the sensor

A flat wavefront at the pupil plane of the eye was defined by the Thorlabs fibre-coupled laser diode output with collimation lens assembly. Introducing a known

aberration at the pupil plane of the eye calibrated the sensor response and the aberrated point spread function. The sensor response and the wavefront aberration reconstruction calibration are presented in this section for low- and high-order aberrations (tip tilt, defocus and coma respectively).

3.3.2.1 Tip-tilt in the sensor signal

When the fibre laser mount is shifted in the back focal plane of the collimation lens in the calibration arm, the transverse shift of the point spread function at the science camera (measured in pixels from the central position) corresponds to the tilt introduced in the pupil plane at the edges of the calibration iris. Equation 3.18 computes with Matlab the theoretical value of sensor signal for a modulation radius considered.

As stated by Equation 3.19 for a tip-tilt θ the sensor signal saturation occurs at a value limited by the modulation amplitude. From the minimal modulation radius defined by the radius of the Airy function to the maximal modulation amplitude defined by the steering mirror cut-off for 100 Hz signals, the sensor sensitivity adjustment corresponds to factors M1 to M14. The modulations factors M3 represented in Figure 3.10 represented three values evenly distributed (M3 = $9\lambda/D$, M7 = $21\lambda/D$ and M11 = $33\lambda/D$) amongst the full range. From Figure 3.10, the maximal extension of sensing range is in pixels 9 times larger than the minimal sensor range.

(a) Average signal over tip and tilt   (b) Average signal (s_x) for tilt over pupil sampling
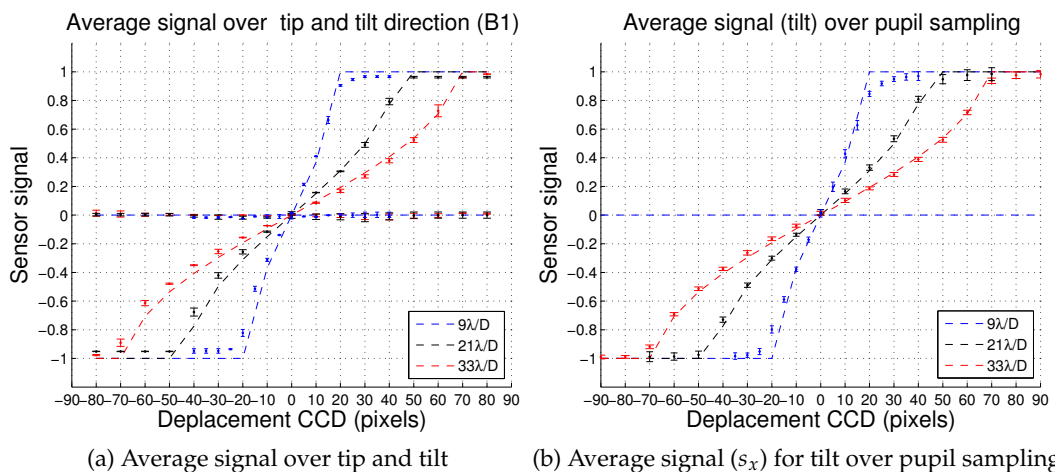
Figure 3.10: Sensor signal for modulation 9, 21 and 33 λ/D. Blue, red and black dashed lines model the sensor response for the tilt applied, marks note the average value measured over the sensor signal. Error bars are the standard error of the mean for 1 frame in each direction in (a) and for 1 frame in each binning in (b).

The comparison of the computed sensor signal with the experimental signal recorded over tip and tilt directions is presented in Figure 3.10a. The amplitude of the standard deviation of the mean shows that the sensor response is consistent with the theory in both directions of tilt. The same measurement performed over a single direction (tilt) but with a variable number of samples in the pupil is presented in Figure 3.10b. The amplitude of the standard deviation of the mean shows the measured signal is consistent with the theory for all the pupil sampling configurations. In turn, the comparison of the model with the experimental signal shows few errors for the direction parameter and the same is observed for the wavefront sampling parameter. In both cases the experimental data and the model are thus in excellent agreement.

3.3.2.2 Defocus in the sensor signal

As the derivative of the defocus aberration is a linear function of the pupil position [42], the limit sensor signal before saturation can be numerically computed as a linear distribution across the pupil. At the limit of the sensing range, the signal across the pupil s_{xD} is linearly distributed from (c = -1) to (c = 1). For higher defocus the (±1) boundary value overfills the pupil gradient with only (-1) and (1) values. For a given modulation amplitude, a computed sensor map as expressed in Equation 3.20 with $|c|$ = 1, simulates the defocus derivative along the horizontal direction with 56 wavefront samples (Binning 1) across the sensor pupil for the two modulation radii $R_{mod} = 9\,\lambda/D$ and $R_{mod} = 33\,\lambda/D$:

$$s_{x\Delta}(x_{pup}) = \frac{x_{pup}}{r_{pup}} \qquad \text{with} : x_{pup} = [-r_{pup} : +r_{pup}] \qquad (3.20)$$

$$\frac{\partial \varphi_\Delta}{\partial x} = \frac{2\pi}{\lambda} \tan\left(\frac{R_{mod}}{f}\right) \sin\left(\frac{\pi}{2} s_{x\Delta}\right) \qquad (3.21)$$

φ_Δ describes the phase aberration of the defocus value for which the limit of the sensing range is reached in the geometrical approximation. The notation Δ replaces in the following the conventional notation for the wavefront defocus in Dioptres units (D) here used to describe the pupil diameter for the modulation.

The sensor signal was acquired after implementation in the pupil plane of the calibration assembly of a convex ophthalmic lens of +0.5 Δ and +1.5 Δ power. The cross section of the horizontal and vertical gradient recorded at the three test modulations is represented in Figure 3.11 as a function of the sample position in the pupil. The ex-

perimental signal of Figure 3.11 is compared to the typical sensor signal for a defocus gradient at the saturation limit for the modulation amplitude considered (given by Equation 3.21).
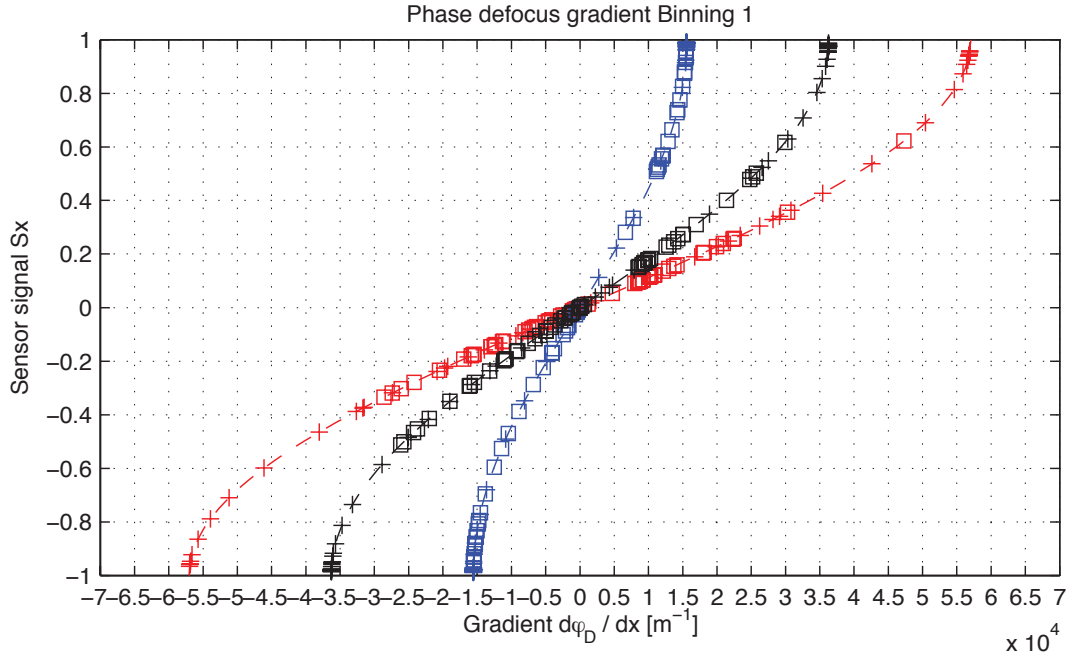
Figure 3.11: Sensor signal for defocus: sensor signal modelled for a given modulation, (dashed line from -1 to +1). The signals cross-sections for 0.5Dioptre(Δ) sphere lens (squared) show the same $\pm 2.7 m^{-1}$ gradient amplitude as the sensor saturation is not reached and show saturation is reached for 1.5 Dioptre(Δ) (crossed marks).

For a small aberration (± 0.5 Dioptre(Δ) square marks) the sensor signal is distributed between ± 0.8 in modulation $9\lambda/D$ and ± 0.4 in modulation $33\lambda/D$. The range boundaries are reached at ± 1.5 Dioptre(Δ) when the sensor signal are at ± 1. This highlights that 0.5 Dioptre(Δ) defocus remains in the linear range for the $33\lambda/D$ modulation while it saturates the $9\lambda/D$ range. This also shows that the sine function would be correctly approximated by its argument in the former modulation. However, for a higher sphere refraction power such as 1.5 Dioptre(Δ), given the gradient is distributed over more than the linear range the linear approximation would not be valid.

The second observation is that the sensor modulation ranges are appropriately chosen with regards to the generally accepted amplitude of refractive errors in the human population [95,96,97] as the range could again be extended for higher defocus amplitudes.

3.3.3 Wavefront reconstruction for high-order aberrations

In this section we explain the procedure followed for obtaining the values of the wavefront aberration measurement in ophthalmic terms. The wavefront decomposition in coefficients of orthonormal Zernike circle polynomials is first presented in relationship with a given wavefront sampling and sensitivity regime. This establishes the equivalence of signal processing in the Shack-Hartmann and the pyramid sensors for a known quantity of low-and high-order aberrations in single pass. The optical system for aberration measurements in the human eye in-vivo is described and the results are commented upon.

3.3.3.1 Aberration map reconstruction

Wavefront measurements are expressed in units of phase aberration (waves) or in metric units (μm), quantifying the wavefront departure from the reference sphere as the root-mean-square (rms) wavefront error. The guidelines [43] recommend the use of the Zernike circular polynomials towards other notations [98]. Matlab functions for the reconstruction are available on-line [99]. The conversion of the sensor signals into phase gradient maps is performed before the least-squares fit of the sensor gradients map onto the (1-N) vectors of the basis of Zernike maps derivative. The wavefront is reconstructed using the coefficients of the fit for each order N.

In this ophthalmic convention a Zernike term Z_n^m describes a typical aberration pattern in polar coordinates (ρ, θ) with $\rho = [0,1]$ the normalized radius of the pupil and $\theta = [0,2\pi]$ the angle made to the vertical axis, as a function of a normalization factor N_n^m, a radial-dependent component R_n^m, and an azimuthal-dependent component. The double indexing scheme (n, m) expresses the polynomial spatial content through the radial order index n and the pattern shape through the angular frequency m.

$$Z_j(\rho, \theta) = Z_n^m(\rho, \theta) = \begin{cases} \sqrt{(n+1)}R_n^0 & \text{for } m = 0 \\ \sqrt{2(n+1)}R_n^{|m|}\cos(m\theta) & \text{for } m > 0 \\ -\sqrt{2(n+1)}R_n^{|m|}\sin(m\theta) & \text{for } m < 0 \end{cases} \qquad (3.22)$$

The radial component $R_n^{|m|}$ in Equation 3.22 is given by

$$R_n^{|m|}(\rho) = \sum_{s=0}^{(n-|m|)/2} (-1)^s \frac{(n-s)}{s[(n+|m|-s)][(n-|m|-s)]} \rho^{n-2s} \qquad (3.23)$$

In this thesis the single indexing notation j was mainly used, as equivalently defining the decomposition order :

$$
\begin{aligned}
n &= roundup\left[\frac{-3+\sqrt{9+8j}}{2}\right] \\
m &= 2j - n(n+2) \\
j &= 0,1,2,...N
\end{aligned}
\tag{3.24}
$$

In the single-indexing notation the first terms of the decomposition (j=0, piston, j=1, tip and j=2, tilt) are usually excluded from the expression of the wavefront aberration. The wavefront aberration W is expressed using N polynomial terms of the decomposition:

$$
W(\rho,\theta) = \sum_{j=3}^{N} a_j Z_j(\rho,\theta)
\tag{3.25}
$$

In which the coefficients amplitude a_j in (μm) is given by the integrals of the inner product over the normalized pupil A.

$$
a_j = \int\int_A W_j(\rho,\theta)Z_j(\rho,\theta)d\rho d\theta
\tag{3.26}
$$

Given the Zernike polynomials are defined on an orthonormal basis, the terms of the decomposition are independent thus for an infinite number of terms only the wavefront root mean squared error (RMS) is the squared root sum of the squared coefficients a_j^2 [100]. As the wavefront is reconstructed over a finite number (N) of modes, the rms obtained by the Matlab sum of coefficients is only approximate.

$$
RMS = \sigma = \sqrt{\sum_{j=3}^{N} a_j^2}
\tag{3.27}
$$

Tip and tilt coefficients ($j = 1$, $j = 2$) were removed from the rms calculation so as to consider only the higher orders. The error on a Zernike term for the mean value presented was defined by the standard deviation of the mean of the term for a series of static measurements. This variation was very low for the calibration compared to the measurement of the dynamic ocular aberration.

The maximal number (N) of modes used for the reconstruction is usually determined by the number of actuators of the deformable mirror. The 52-elements electro-magnetically actuated membrane of the Mirao deformable mirror has numerically shown a diffraction-limited fitting of ocular wavefronts was obtained using 30 mirror modes [47] thus (N)

was set to 35 in the adaptive optics system. For faster computation the reconstruction of the wavefront aberration from the sensor signal was performed with 15 modes (order $n=4$) or with 35 modes (order $n=7$) for a best accuracy of the reconstruction as recommended by Hampson [101]. For reading clarity most decompositions were displayed in the following up to the 21^{rst} term (order $n=5$). Experimental adjustments towards this value for the adaptive optics are presented in Chapter 4.

3.3.3.2 Maximal measurable aberration for a Zernike radial order

In a Shack-Hartmann the pupil sampling is determined by the number of lenslets across the pupil while the sensitivity range depends on the focal length of the lenslets. The maximal wavefront aberration W_{max} measured by the sensor for a given Zernike radial order can be expressed in function of the lenslet array characteristics [102]:

$$\frac{W_{max}}{\lambda} = \frac{N_l\,N_{Fr}}{4n} \quad \text{with:} \quad \begin{cases} N_l & \text{Samples (lenslets or pixels) across the pupil} \\ N_{Fr} = \frac{d^2}{f'\lambda} & \text{Fresnel number of the lenslet} \\ d & \text{Lenslet (pupil sample) diameter} \\ f' & \text{Lenslet focal length} \\ \lambda & \text{Wavelength} \\ n & \text{Zernike radial order} \end{cases}$$

(3.28)

Equation 3.28 is useful for the design of an aberrometer as it can determine the choice of the lenslet array focal length and pitch. Provided indeed that an estimate of the measurement amplitude is known, the Shack-Hartmann parameters can be defined so as to sample properly the amplitude of the radial order (n). For an aberrometer of variable sampling and dynamic range such as the pyramid sensor used in this work we propose to apply these relationships to compare our sensor to other aberrometers.

In the pyramid, N_l the number of samples of individual size (d) across the pupil can be varied using the sensor camera binning. A given modulation R_{mod} determines the sensor dynamic range. Saturation means a sensor signal at ± 1 thus the sensor

equation for the transverse aberration Equation 3.17 becomes:

$$\frac{\partial W_P(x,y)}{\partial i_{(i=x,y)}}\Bigg|_{max(tiptilt)} = \frac{R_{mod}}{f}\sin[\pi/2(\pm 1)] \tag{3.29}$$

$$= \frac{R_{mod}}{f} \tag{3.30}$$

$$= \theta_{max} \quad \text{following Equation 3.15} \tag{3.31}$$

With f the focal length of the focusing lens before the pyramid and θ_{max} the tip/tilt amplitude at the saturation limit.

The wavefront aberration tilt for $\theta = \theta_{max}$ in the pupil plane is $W_{max(tiptilt)}$:

$$W_{max(tiptilt)} = d\,\sin\theta_{max} \approx d\,\theta_{max} \quad \text{if } \sin\theta \approx \theta \quad \text{(small angles approximation)} \tag{3.32}$$

A single pupil sample is of size (d), and the whole pupil of size (D). The angles measured in this experiment are well within the range that validate the approximation ($\pm 6°$) and Equation 3.32 thus applies for the pyramid.

For N_l samples in the pupil, $D = d \times N_l$. The binning factor and N_l are related by the minimal pupil subaperture size (N_0) in the camera minimal binning (highest pupil spatial sampling). Thus :

$$N_l = binning \times N_0 \tag{3.33}$$

Equation 3.33 expresses the change in the number of samples in the pupil with the binning factor for the pyramid, that is the equivalence with the change in the number of lenslets.

Replacing in Equation 3.32 the maximal angle by the modulation factor from Equation 3.31, the maximal wavefront aberration due to tip/tilt for the pyramid subpupil is :

$$W_{max(tiptilt)} = \frac{d}{f}\,R_{mod} \quad \text{in the small angles approximation} \tag{3.34}$$

As (f) the focusing length is fixed, and (d) is fixed for a given camera binning, Equation 3.34 shows that in the pyramid the modulation factor determines the limit for the

maximal wavefront aberration due to tilt.

The equivalence between Equation 3.28 for ($n = 1$ for tip and tilt) at a given pupil sampling (N_l) and Equation 3.34 considering a similar sampling and pupil size leads to a modulation radius value that describes the dynamic range of an equivalent Shack - Hartmann. For the tip tilt order n=1 thus $R_{mod} = R_{mod(n=1)}$:

$$\text{From } (3.28 \equiv 3.34) : \quad \left(W_{max(tiptilt)} = \frac{d}{f'} \frac{dN_l}{4} \right) \equiv \left(W_{max(tiptilt)} = \frac{d}{f} R_{mod(n=1)} \right)$$

$$\tag{3.35}$$

$$\text{We can identify:} \qquad \left[f \frac{dN_l}{4f'} = R_{mod(n=1)} \right] \tag{3.36}$$

$$\text{If } f'_{SHS} = f_{PWS} : \qquad \left[\frac{dN_l}{4} = R_{mod(n=1) \atop f'=f} \right] \tag{3.37}$$

If the focal lengths of the Shack-Hartmann and of the pyramid are equal and the pupil samplings are equal, as in Equation 3.37 then the modulation radius that leads to an equivalent Shack-Hartmann dynamic range for tilt is $R_{mod(n=1)}$. The use of a higher or lower modulation range is equivalent to a change in the Shack-Hartmann lenslet focal length (f') in Equation 3.36.

For any order and any sampling, we can use Equation 3.36 into Equation 3.28. The 'base' modulation radius of the sensor for any radial order appears for $f = f'$, and the change in sampling across the pupil N_l is also taken into account. For each case :

$$\text{If } f' \neq f : \quad W_{max(n)} = \frac{d}{n} \frac{f}{f'} \frac{dN_l}{4} \qquad \text{with thus } R_{mod(n)} = \frac{f}{f'} \frac{dN_l}{4n} \tag{3.38}$$

$$\text{If } f'=f : \quad W_{max(n)} = \frac{d}{n} \frac{dN_l}{4} \qquad \text{with thus } R_{mod(n)} = \frac{dN_l}{4n} \tag{3.39}$$

This means that for a given pupil sampling and modulation at the sensor the maximal measurable wavefront aberration of a Zernike order in the decomposition is known.

In our case the sensor was built before this study was performed, thus the huge focal length of the first lens of the relay from the steering mirror to the wavefront sensing camera turns this analysis into an irrealistic case for the Shack-Hartmann. However, simulations using pyramid sensor signals in the wavefront reconstruction code show

a good agreement with the experiment for the tip tilt case and for the defocus.

For the particular case of tip and tilt (n=1) and a pupil sampling of N_l=52 pixels across the pupil, with each pixel in the pupil plane of size $d = 0.067$ mm, and a focal length $f' = f = 250$ mm, we can find the pyramid modulation factor that retrieves a similar behavior as an equivalent SH. Replacing the values in Equation 3.37 gives $R_{mod(n=1)}\big|_{f'=f}$ = 15×R_{Airy} (M6.7 factor), that is almost the (M7) modulation. Using Equation 3.36 the modulation factor range of the pyramid system relates to the variation in the focal length (f') of the equivalent SH.

For further building of another pyramid system this set of relationships could be useful for the designer. The characterization of the sensor dynamic range built in this system is actually showing a large range for the base values, and small ranges that are not very sensitive to small aberrations.

3.3.3.3 Tip/tilt and Defocus in Zernike decomposition

In both Figure 3.12a and Figure 3.12b the wavefront aberration presented was experimentally determined after the average reconstruction over 5 single sensor acquisitions. Zernike tilt term was obtained from the sensor signal recorded after transverse displacement (tilt) of the fibre output at the back focal plane of the calibration lens as in Section 3.3.2 in steps of 30 pixels at the retinal imaging camera. Zernike defocus was tested using ophthalmic lenses of ±1.5 D sphere power in steps of ±0.5 D. Part of this dataset was used for Figure 3.11.

Theoretical Zernike tilt signal was modelled using geometrical optics to relate the lateral displacement of the point spread function at the science camera to the angular tilt at the pupil plane of the calibration arm and scaling for the pupil diameter to obtain the aberration in micrometers. Theoretical defocus amplitude was modelled using the conversion equations [103] from the refractive power of an ophthalmic lens into Zernike decomposition.

The standard deviations of the mean for each point was of the order of $10^{-3}\mu$m thus the measurement stability was verified for such static aberration. Sensor saturation at a given dynamic range corresponded to a constant value of the aberration. Sensor non-linearity was represented by the departure of the measurement from the theoret-
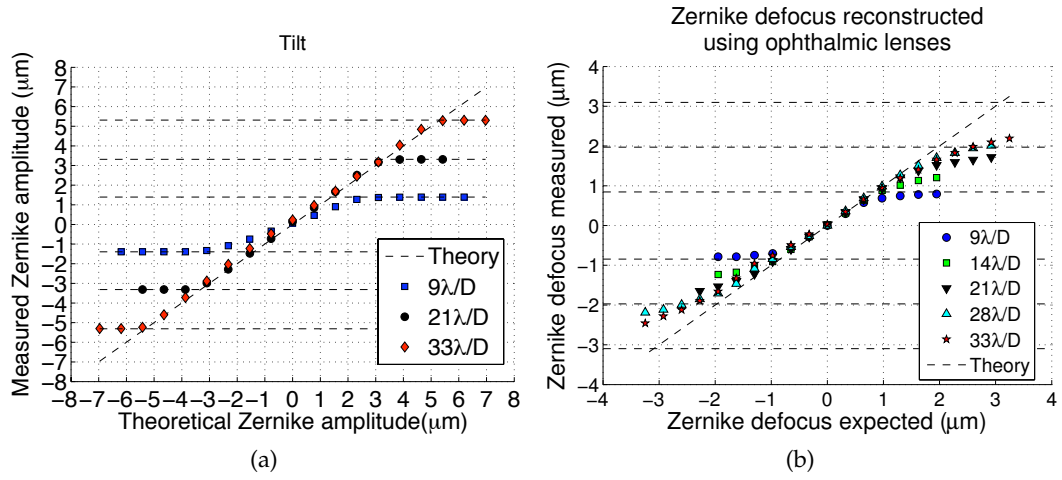
Figure 3.12: Tilt and Defocus measured at the highest pupil sampling (B1, 109μm per sample). Horizontal dashed lines show the saturation limits of the Zernike term for each dynamic range defined by the modulation factors 9, 21 and $33\lambda/D$. Linearity of the sensor response is satisfied when the theoretical and measured term amplitudes correspond. Sensor saturation for defocus is reached only at $9\lambda/D$.

ical value. The tip-tilt non linearity range coincided with the saturation range while the defocus non-linearity spread over a wider range of aberrations before the saturation value.

3.3.3.4 Higher-order aberrations in Zernike decomposition

The static response of the system to typical ocular aberrations was measured in placing in the pupil plane of the calibration arm plastic plates engineered with a resin substrate deposited in the shape of a known phase aberration [104]. Plate 1 and plate 2 were shaped as typical ocular aberrations of human eyes. Plate 3 and plate 4 were shaped in a known amplitude of known aberration, defocus (Z20) and trefoil (Z16).

The plates wavefront aberration was first measured using a Twyman-Green interferometer (Fisba Optik, Switzerland) which provided high-resolution surface characterisation of the patterns with 10 μm per wavefront sample over the 6 mm measurement pupil. The plates were then positioned individually in the pupil plane of the calibration beam and the phase was measured at each of the 4 sensor sampling settings for the 3 tests modulations. For each pupil sampling setting, 50 sensor measurements of the aberration were acquired and the respective wavefronts reconstructed. A 10^{-3} μm rms variability of the rms error over the 50 frames stated the stability of the sensor
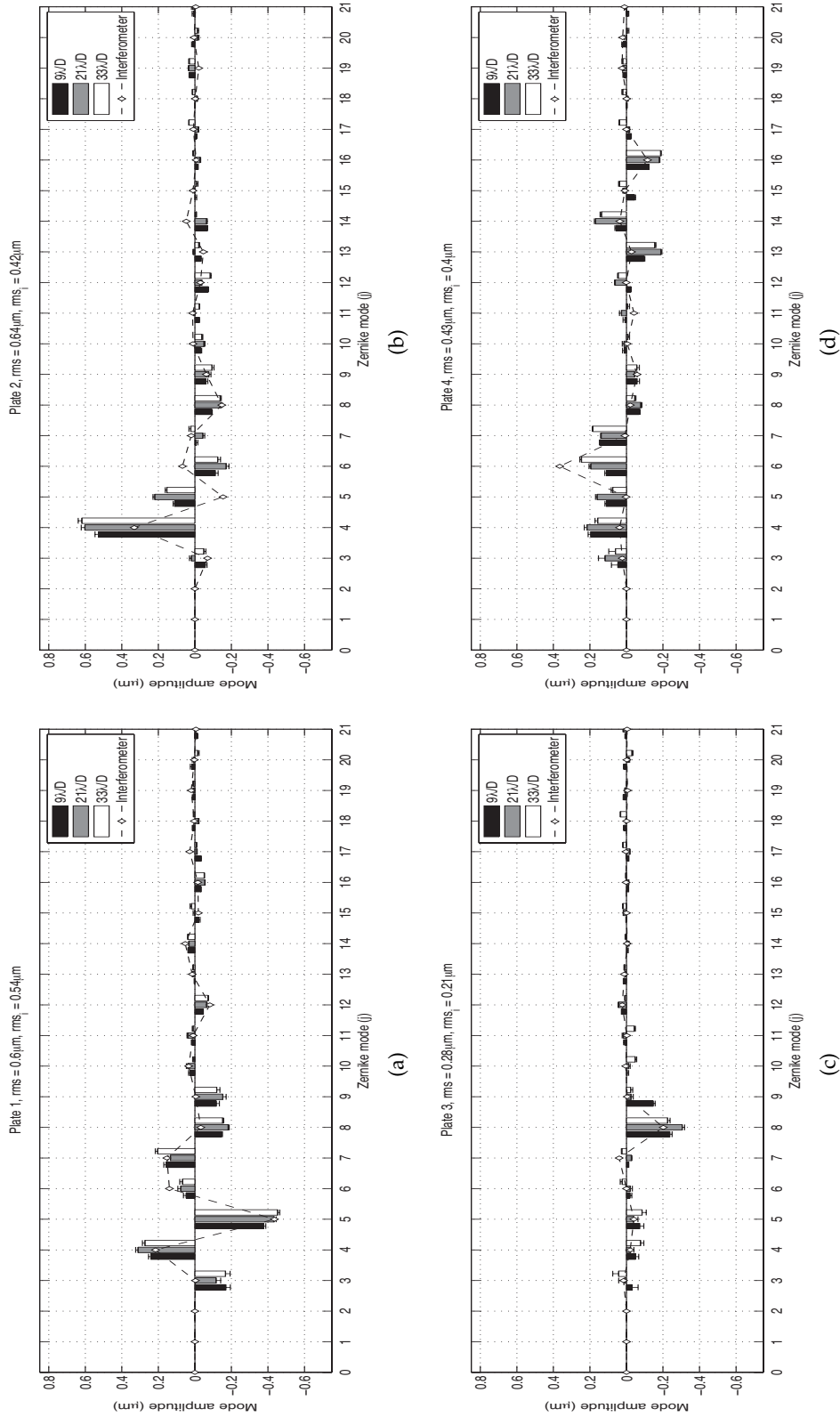
Figure 3.13: Zernike phase plates coefficients after wavefront reconstruction. Dashed line with diamond mark is the interferometer measurement, black, gray, white bars show 9, 21 and 33 λ/D modulation. rms is calculated from the coefficients root mean squared error of the sensor wavefront measurement averaged over the 3 modulations and rms_i is calculated from the interferometer single measurement. Error bars are the standard deviation of the mean over the 4 pupil samplings.

measurement for each pupil sampling. The aberration coefficients averaged over the sampling setting for each dynamic range for each phase plate are displayed in Figure 3.13 with the wavefront decompositions fitted from the interferometer measurement. The average wavefront rms for all dynamic ranges compared to the rms of the plate measured by the interferometer is presented in the title of the displays in Figure 3.13. Detailed values of rms for each dynamic range averaged over the binning are presented in Table 3.2.

For low order modes (defocus Z4, astigmatism Z3 and Z5) a higher coefficient variability with the pupil sampling was observed than for the higher orders. As the pyramid is considered as an appropriate sensor for these modes, this effect could be related to the change in the pupil sampling. Additional astigmatism in the pyramid measurement in plate 1 and 3 and defocus, and secondary astigmatism in plate 4 decreased the fit between the 2 measurement systems. These were attributed to the slight changes in the plate lateral positioning, pupil size and reference wavefronts in the respective setups [105].

Table 3.2: RMS of phase plates measured at modulation factors $9, 21, 33\lambda/D$ and with Fisba interferometer. Standard deviation of each rms corresponds to the variation over the pupil sampling setting.

rms (μm)	Plate 1	Plate 2	Plate 3	Plate 4
Interferometer	0.54	0.42	0.21	0.40
M3 = $9\lambda/D$	0.55±0.01	0.57±0.02	0.30±0.01	0.35±0.01
M7 = $21\lambda/D$	0.63±0.01	0.69±0.07	0.32±0.03	0.50±0.02
M11 = $33\lambda/D$	0.63±0.06	0.68±0.05	0.28±0.01	0.47±0.03
Mean (all M)	0.60±0.04	0.65±0.05	0.30±0.02	0.44±0.06

An average rms variability of ±0.03 μm with the pupil sampling was obtained for the aberration measurement by the sensor. The sensor pupil sampling change was thus not neglectible in the measurement of an aberration. The number of pupil samplings sets tested here (4) was not sufficient to determine a trend. An average variability of ±0.04 μm with the dynamic range was obtained for the aberration measurement by the sensor. This stated the influence of the sensor dynamic range on the aberration measurement. The average rms measured by the sensor for each plate was of 0.1 μm higher than the interferometer rms, which represented the differences in positioning of the plate in the pupil plane and the differences between the sensor settings and the interferometer settings. The suitability of the pyramid system built for these ranges of aberrations was confirmed by comparison of the aberration amplitudes measured

with the calibration curves for defocus in Figure 3.12b. The phase plates aberrations were well below the sensor limits for the modulation considered.

Influence of tip and tilt of the wavefront on the aberration measurement

The influence of the tip and tilt on the reconstruction of the wavefront is presented in Figure 3.14 and Figure 3.15. The emphasis was put on the shape of the wavefront reconstructed with or without account of the tip and tilt terms. A single sensor frame was recorded for 8 tilts tested between the centering of the fibre position and saturation of the sensor signal for the smallest modulation amplitude (M3=$9\lambda/D$) and the highest pupil wavefront sampling (56 samples across the pupil). Figure 3.14 represents the average Zernike decomposition determined over the 8 wavefront reconstructions. The 0.1 μm variability of the term amplitude for defocus (j=4), astigmatism (j=5), spherical aberration (j=6) and coma (j=7) is due to the tip tilt increase.
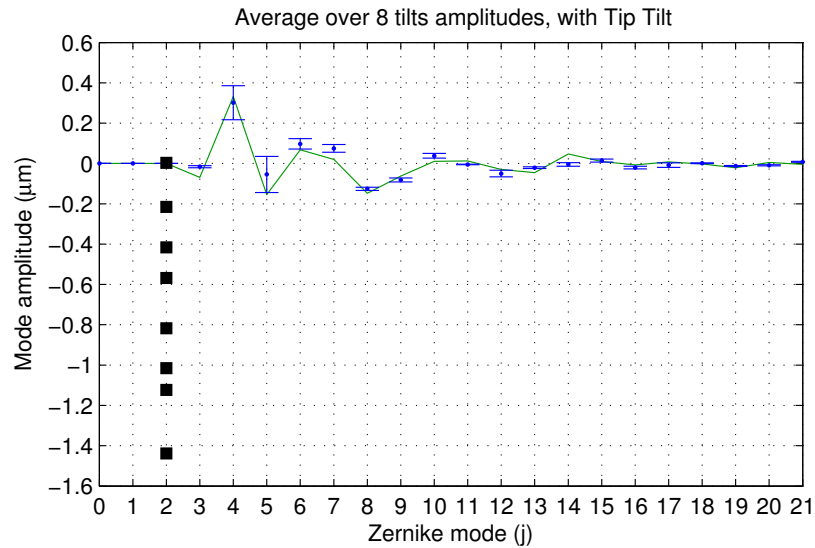
Figure 3.14: Plate 2 with increasing tilt measured by the sensor with 56 samples across the pupil and a modulation factor of $9\lambda/D$, (M3). Error bars are the standard deviation of the mean coefficient for the 8 tilt amplitudes measured. Interferometer coefficients in green. Black squares denote the tilt coefficients tested.

When applying progressively tip to the pupil plane by transverse movement of the laser fibre head, the sensor phase measurement evolution is shown in Figure 3.15. Figure 3.15a presented the on-axis measurement of plate no.2 in which the Zernike tip and tilt coefficients had a zero-amplitude. Figure 3.15b presented the wavefront reconstruction of the same phase plate for the highest tilt amplitude. Figure 3.15c represented the wavefront reconstruction of the phase plate measured with the highest

tip and tilt amplitude but reconstructed without those terms.
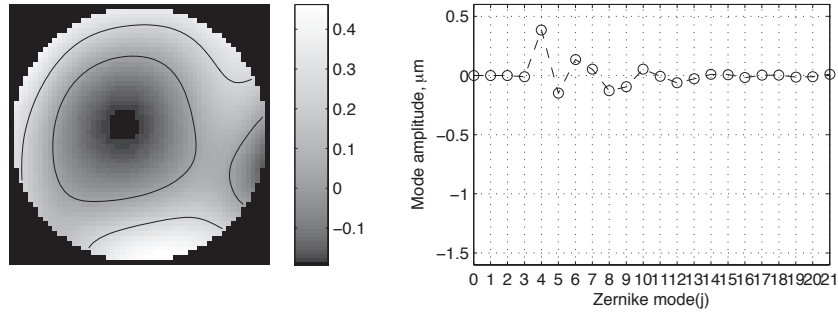
(a) On-axis
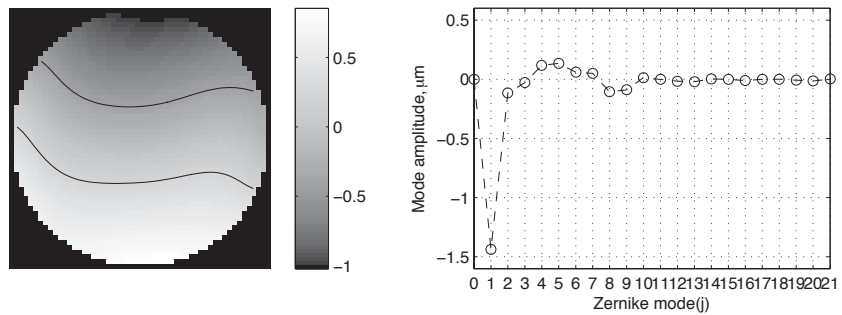
(b) Off-axis reconstructed with tip and tilt
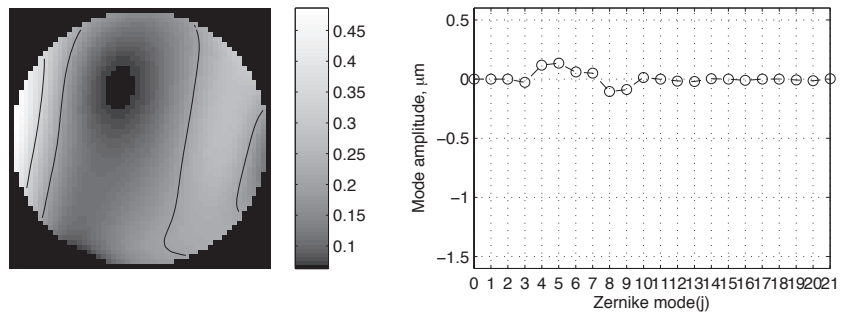
(c) Off-axis reconstructed without tip and tilt

Figure 3.15: Wavefronts and coefficients display with increasing tilt not accounted for in the reconstruction

From the wavefront maps including tip and tilt in the wavefront reconstruction, the aberration appeared to be shifted up as the tilt increased, but in reality the phase plate was static at the pupil plane of the system. When removing tip and tilt in the wavefront reconstruction however, the impact of these terms on other Zernike coefficients appeared more clearly. The peak to valley of the wavefront aberration evolved from (-0.6 μm, +1 μm) to (-2 μm, +2 μm) the more the phase was inclined. The coefficients amplitude depended on the shift of the aberration pupil but tended to zero as the

phase was progressively dominated by the tip/tilt.

A Zernike tilt term that corresponded to the sensor saturation - from calibration data in Figure 3.12a ($9\lambda/D$) was identified. A 0.15 μm decrease of the defocus term (Z4) was measured from the on-axis wavefront in Figure 3.15a to the off-axis wavefront in Figure 3.15b. Reconstruction of the off-axis wavefront with zero-amplitude tip and tilt was illustrated in Figure 3.15c. The phase aberration remained centered, but significantly differed from the wavefront shape of the on-axis reconstruction while the aberration was static. The defocus coefficient amplitude was identical to the reconstruction with saturated tip and tilt, and again of reduced amplitude compared to the on-axis (real) wavefront.

In conclusion the phase aberration out of the eye quantified from the Zernike decomposition of the sensor measurement was correctly described provided that the sensor tip/tilt saturation was not reached. Usually the tip and tilt terms in our wavefront sensor were estimated as coming from the direction of specular reflection of the probe beam onto the retina after scattering. Showing that these terms do not introduce error in the aberration measurement validated the wavefront reconstruction and highlighted its limits.

3.3.4 Wavefront and image camera point spread function

The laser fibre source at the back focal plane of the collimation lens was best observed when the deformable mirror reproduced the shape of a plane mirror. The image at the science ccd camera through the system optics was a perfect Airy disk in theory. The introduction of a wavefront aberration in the pupil plane of the calibration assembly such as the one of the phase plates deteriorated the point spread function. Comparison of the point spread function computed from the sensor measurement with the effective point spread function image recorded at the science camera aimed at showing whether the conjugation of the science camera with the pupil plane was satisfied.

Method

In a first approximation the 1360×1024 pixels ccd camera chip was simulated into a 1024x1024 array, in which each pixel represented a sample of the Fourier transform of the pupil aperture. An aperture of 512 pixels diameter centered on the 1024×1024 pixels array defined the computational pupil plane mask for the simulation. In this mask

a uniform amplitude was chosen for the wave describing the pupil plane. The sensor reconstructed wavefront was resized into 512×512 pixels and was rescaled from micrometric unit into phase units to define the exponential phase factor of this wave. The Fourier transform of the complex wave was performed with the Fast Fourier Transform (FFT) algorithm of MatlabR2010b. A window of 80×80 pixels (0.23°×0.23°, or 14.2×14.2 arcmin region of the calibration beam artificial retina) was defined in the simulated Fourier array at the same position as the region of interest selected in the science camera.

Figure 3.16 displays the wavefronts reconstructed from the interferometer measurement (first row), and from the sensor average measurement (second row). The point spread functions computed from the sensor average measurements and from the interferometer measurements are respectively presented in third and 4th row. 50 ms and 10 ms exposure images recorded at the science camera are respectively presented in 5th and 6th row.

Discussion

The agreement between the aberration measurements by the interferometer and by the sensor were discussed in Section 3.3.3.4. The sensor root mean squared amplitudes calculated from the Zernike decomposition were respectively defined in Table 3.2 and are of 0.60 μm, 0.65 μm, 0.30 μm and 0.44 μm for the plates 1, 2, 3 and 4. The interferometer rms wavefront error were respectively of 0.54 μm, 0.42 μm, 0.21 μm and 0.40 μm. The comparison of the aberrated point spread function imaged at the science camera and simulated in Matlab should be done by cross correlation, or by a pixel - to - pixel identification and not only visually.

For the experimental data presented in Figure 3.16, the science camera image and the simulated psfs presented similar patterns and similar extents, thus the science camera image was a Fourier plane for the pupil plane. Shorter exposure times of the camera presented better visual correspondence. An experimental Strehl ratio based on the maximal intensity in the open loop regime towards the maximal intensity in the closed loop regime for a constant exposure and gain at the camera could not be defined.

The differences between the science psf and the computed psf were most probably related to the non-common path errors between the science camera and the wavefront sensor camera. The correspondence of patterns however let estimate the non common path errors remained small in this system. The science camera psf image also
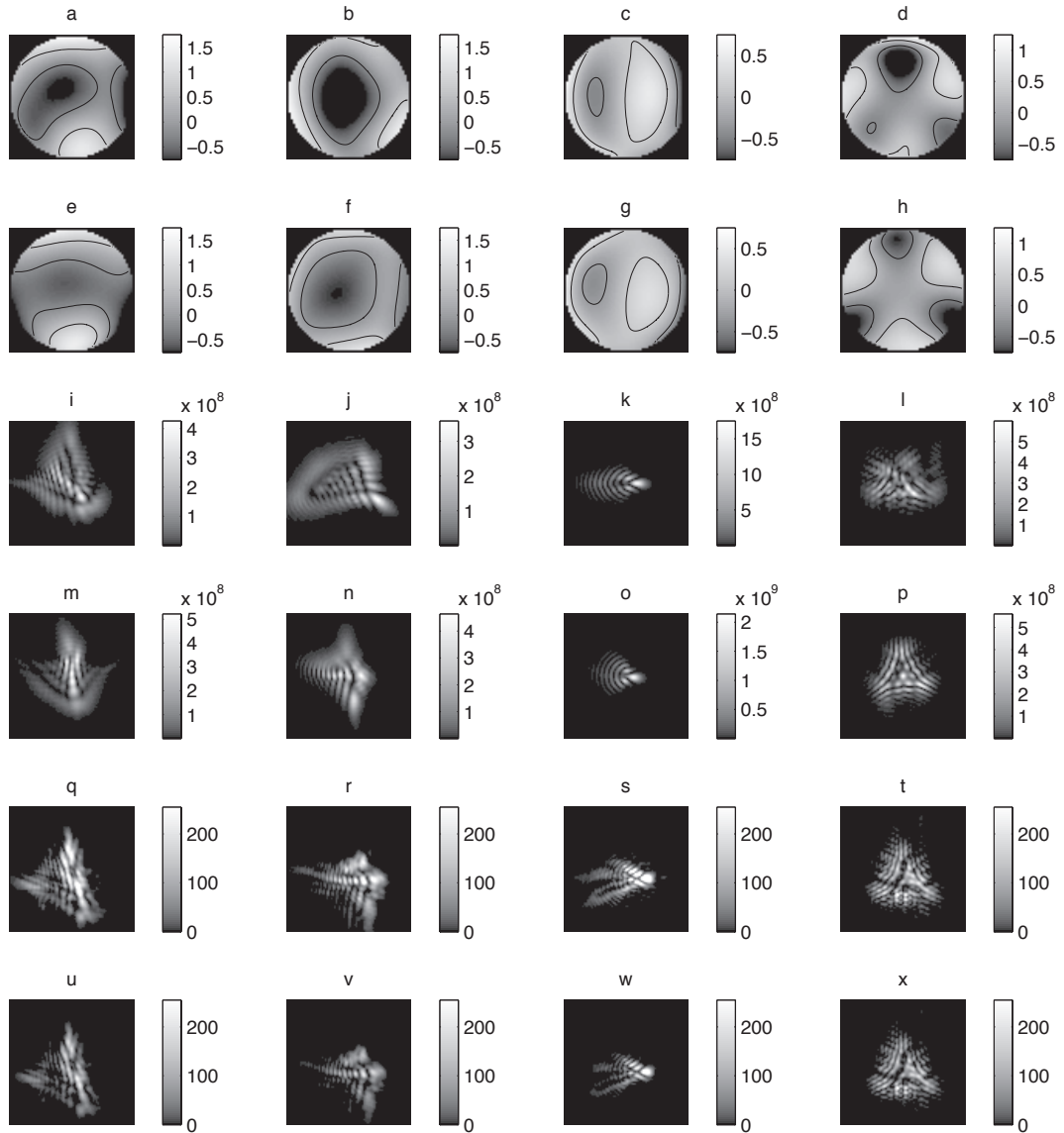
Figure 3.16: Zernike plates wavefront aberration measured by the Interferometer (a-d), measured by the wavefront sensor, after averaging over all samplings settings and dynamic ranges (e-h), computation of the psf from the sensor measurement (i-l), computation of the psf from the interferometer measurement (m-p). PSF recorded at the science camera, exposure 50ms (q-t). PSF recorded at the science camera, exposure 10ms (u-x). Image size in Figures (i-x) is $0.23° \times 0.23°$ (or 14.2×14.2 arcmin)

depended on factors such as the camera image exposure, gain, binning and the laser power used.

3.4   Summary

This Chapter described the implementation of the ocular aberration measurement with the pyramid wavefront sensor. Section 3.1 introduced the applications of the pyramid wavefront sensor. Section 3.2 described the mathematical basis of the wavefront sensor measurement and the optical system. All equations for the sensor sensitivity were derived assuming the focusing into an Airy disk pattern. The base sensitivity of the pyramid system was defined by the f-number of the wavefront sensing beam onto the pyramid, and the beam modulation extended the sensor dynamic range.

Section 3.3 demonstrated a calibration method for verification of our results in terms of Zernike coefficients. Using a set of phase plates calibrated with a high-resolution interferometer to introduce an aberration in the pupil plane of the calibration beam, the aberration reconstruction from the sensor measurement presented an rms increased of 0.1 μm compared to the aberration reconstructed from the interferometer measurement. The wavefront reconstruction from the sensor signal for 50 successive frames highlighted an rms standard deviation of $\pm 10^{-3}$ μm. This value characterized a high repeatability of the measurement and a low sensor noise. An average rms variability of ± 0.03 μm with the sensor sampling setting highlighted the pupil sampling influence on the aberration measurement. An average rms variability of ± 0.04 μm with the dynamic range highlighted the test modulations influence on the aberration measurement. In the particular case of defocus (Plate no.3), for which the comparison of the measurement with the sensor calibration curves is possible, the test modulations defined a large dynamic range of low sensitivity to the amplitude of the defocus to measure.

In Section 3.3.4, the point spread function computed using the Fourier transform of the wavefront reconstructed after the sensor measurement was compared to the optical Fourier transform of this aberration recorded at the science camera behind the imaging lens. The initial position of the science camera was at the plane which retrieved the best focus for the single pass point spread function, and then the phase

plate was added in the pupil plane of the calibration arm. The point spread function for the system at the pyramid was a scaled version of the direct recording of the single pass point spread function imaged at the science camera. The recorded point spread function was deteriorated only by the aberrations of the phase plate. The qualitative differences observed were not quantified. Contrarily to a numerical simulation the experimental point spread function image depends on the camera exposure and gain, and laser power. In-situ adjustments of those parameters were required to have a sufficient signal-to-noise ratio for both aberrated and aberration-free point spread function images. As described in Chapter 4 the same adjustments were necessary to image the ocular point spread function with adaptive optics correcting the aberration. The corrected point spread function image effectively quantified the static response of the system before use in the eye. Differences between the experiment and the simulation may also be related to the dichroic beamsplitter finite thickness and reflection/transmission coefficients separating the signal between the science path and the wavefront sensor path.

Chapter 4

Adaptive optics

Adaptive optics was initially developed in astronomy (Babcock, 1977) for improving the image resolution in ground-based telescopes by correcting the deviation of the starlight caused by the atmospheric turbulence. In a typical adaptive optics system the wavefront aberration is detected by a wavefront sensor which signal is sent to the control system. The phase correcting device shape (deformable mirror) is adapted following the correction calculated by the control system, resulting in a shaper image of the sky at the science camera.

The pyramid wavefront sensor used in this thesis was described in Chapter 3, and the science imaging system will be discussed in Chapter 5. The current Chapter presents the elements of the adaptive optics system, that is the correcting device, the magnetically-actuated mirror Mirao52-d (Imagine Eyes, France), the control algorithm, and the calibration of the adaptive optics reference wavefront. The adaptive optics aberration correction was then experimentally tested on static aberrations in the form of resin plates and in the eyes of 5 healthy volunteers. Images of the corrected point spread function and acquired simultaneously with the sensor frames are then presented.

4.1   Adaptive optics elements

In this section we will describe the adaptive optics system used in our instrument. The mirror for the new system was the Mirao 52-D magnetically actuated membrane mir-

ror. This mirror was assessed as suitable for the correction of ocular aberrations [47] following numerical simulations of ability to fit typical ocular wavefronts generated from measurements of ocular aberrations [96, 45, 106]. The specifications of the mirror are first presented in comparison to the former mirror. The direct slope algorithm control system for the adaptive optics operation used previously was preserved in the upgrade of the adaptive optics software, initially written by Chamot.

4.1.1 Deformable mirror

Wavefront correctors coupled with adaptive optics systems are either deformable mirrors, segmented phase elements, spatial light modulators (SLM) or liquid crystal devices (LCDs, [107]). The correction by an SLM is provided by phase shifting of the wavefront obtained by control of the polarisation state in the liquid crystal elements of the SLM. Those systems do not "mechanically" control the wavefront phase contrarily to a reflective surface as a mirror. Still the action on the wavefront is physical, in contrast to post processing algorithms of deconvolution, image recentering and filtering. The usual representation for mechanical correctors is schematically reproduced in Figure 4.1 from Hardy [108]. Discrete action on the wavefront is similarly provided by segmented mirrors which consist of an array of reflective elements fixed on an actuator structure with three degrees of freedom; two axes of tilt plus piston motion. Those however suffer from diffraction effects related to the inter-actuactor spacing. Single facesheet surfaces are thus preferred, such as bimorph mirrors made into a multilayered structure in which the reflective surface is bonded to flatdisk piezoelectrical actuators.

Deformable mirrors similarly present a single continuous membrane of reflective materials which deflection (or stroke) is controlled by the action of underneath microelectromechanical systems (MEMS). MEMS systems are based on piezoelectric (PZT), electrostrictive (PMN) and magnetic actuators, depending on their type of physical interaction with the membrane. Piezoelectric control of the actuator to which is attached the mirror facesheet defines a surface deformation in which hysteresis is non negligible. This effect is partially compensated for by recalculation of the mirror commands in the adaptive optics control loop. Micromachined devices (MMDM) are not physically linked to the actuators but the aluminium-coated membrane is attracted (pull-only) by the control electrode. The fixation of the mirror membrane to the mirror edges limits these mirrors typical stroke to ± 5 μm. Using the magnetic force

Piston only   Piston plus tilt

Segmented mirrors

Position actuators   Force actuators

Deformable mirrors

Reflecting coating and common electrode

Two piezo layers

Addressing electrodes

Bimorph mirror

Transparent glass
(optional window)

Membrane mirror   Reflecting membrane

Actuator electrodes

Liquid crystal cell

1/4 wave plate

Mirror substrate

Liquid crystal on tip-tilt mirrror

Figure 4.1: Different types of mechanical wavefront correction systems, from [108].

generated by the drive of an electric current in an actuator coil to attract and repulse a magnet fixed under the mirror facesheet, a push-pull operation of the mirror surface is obtained and thus increases the mirror available stroke.

The Mirao52-d (Imagine Eyes, France) used in this thesis is shown in Figure 4.2. This is a magnetically-actuated mirror of very large stroke compared to the typical operational range of typical deformable mirrors with a ± 25 μm deformation ability from the manufacturer specifications. The 15 mm diameter mirror active pupil contains 52 actuators distributed in a squared array with a 2.5 mm pitch between neighboring actuators and 8 actuators across the pupil diameter. Its suitability for ophthalmic applications over the optimal 15 mm clear aperture was demonstrated [47, 109] and is very similar to the performance estimated over the 12.5 mm aperture [91] of the initial design.
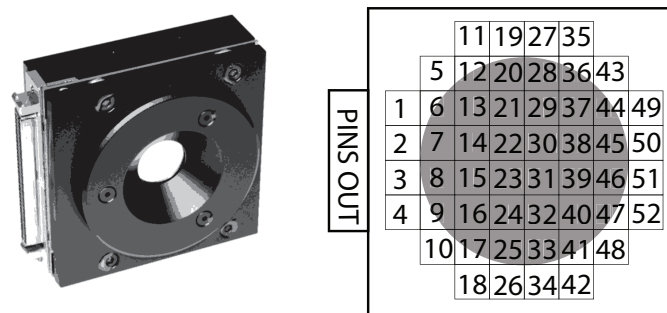
Figure 4.2: Mirao52-d™ mirror and optimal pupil (photography courtesy of Imagine Eyes, France). The mirror active pupil (15mm diameter) is shadowed in gray.

In one configuration of the optical system the 6 mm diameter of the eye was conjugated at the deformable mirror into a 14.4 mm diameter pupil. The mirror influence functions displayed in Figure 4.3 were recorded using a Twyman-Green interferometer (FISBA OPTIK μphase). The mirror surface deflection was reconstructed by this instrument from a stack of successive interferograms measured from a reference position over a 15 mm pupil diameter. The set of influence functions presented was measured using actuator voltages of ± 0.1 V added or subtracted from the initial set of commands defining a "flat" wavefront. This represented $1/10^{th}$ of the voltage range indicated by the manufacturer. Each influence function corresponded to the actuator as numbered in Figure 4.2 from the rear view of the mirror.

The interferometer measurement highlights that the outer ring of mirror actuators is out of the clear aperture of the mirror but nevertheless impacts on the surface shape
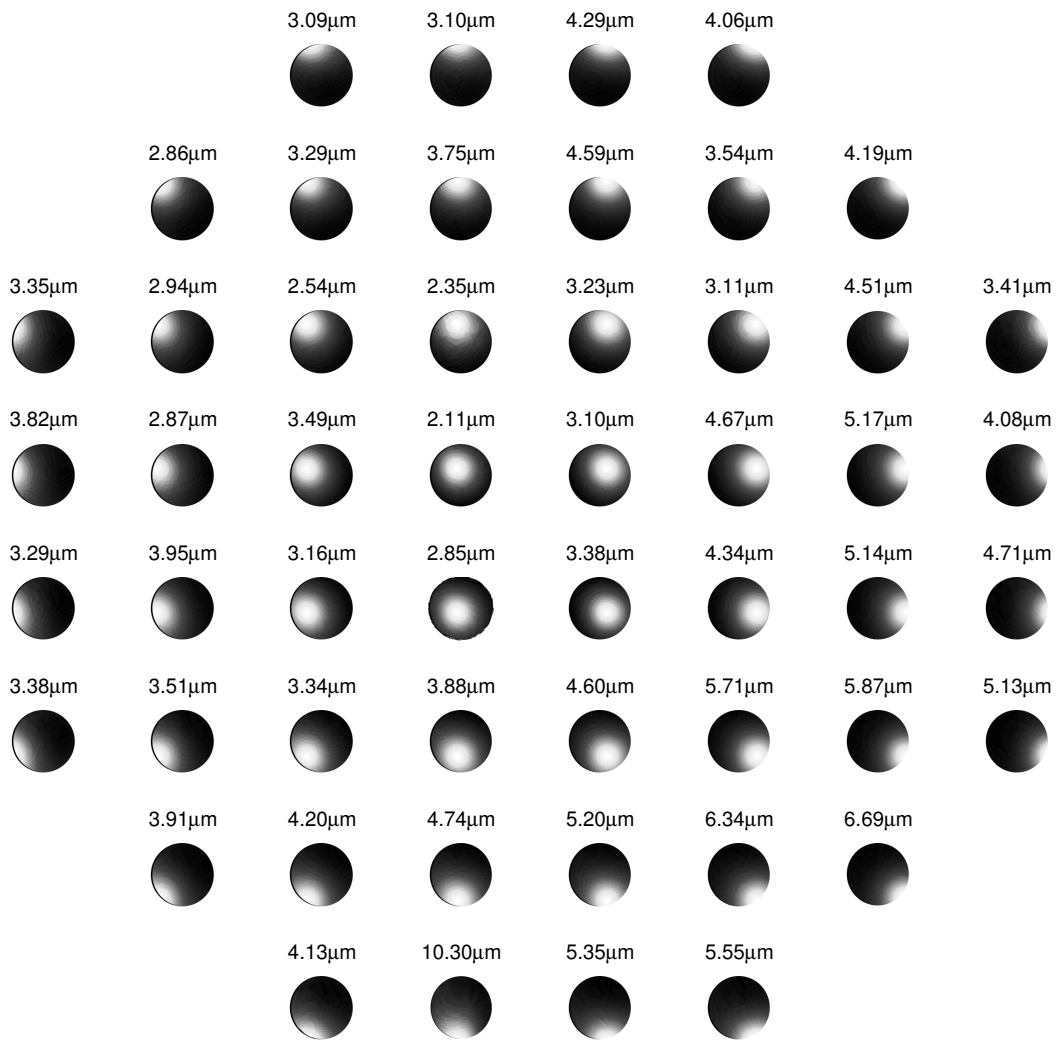
Figure 4.3: Mirao52-D influence functions for surface deflection ± 0.1V from a flat surface. One disk corresponds to the mirror surface measured by the Fisba at the location of the actuator poked. The top numbers are the wavefront peak-to valley for each influence function of the matrix measured from the flat mirror.

when active. The values on top of each influence function are the wavefront peak to valley for $1/10^{th}$ of the maximal mirror stroke, thus the full range (40 μm) stroke is under the manufacturer specification for this configuration. A linearity test was performed for one central actuator over a defocused wavefront until saturation of the interferometer detection range, but not extended to other actuators or to the full range, which might have confirmed the membrane hysteresis measurements (manufacturer, and [110]).

With only 8 actuators across its pupil the spatial resolution of the mirror is limited to the correction of higher orders aberration patterns up to the 7th order (52 modes) and this work was mainly using its large stroke is to correct for high amplitudes of low-order aberrations (3rd order). Previous observations [1] had suggested the new design could benefit from a lower number of pupil samples than used (16×16 samples at the highest binning). The new system at the highest binning presented 14×14 samples across the pupil, thus following the Nyquist criterion per actuator. For a turbulence of the Kolmogorov type in a standard noise configuration those settings are suitable for the Mirao deformable mirror [111]. For ocular aberrations, the experimental determination of the optimal condition number must be performed.

4.1.2   Direct slope control algorithm

Adaptive optics algorithms reconstruct the wavefront from the sensor measurements to determine the mirror deformation required for its correction. In the direct slope algorithm, the sensor signals are used as input for the closed-loop control. The closed loop sensor signal is defined by the calibration beam propagated in the system in which the deformable mirror commands forms a 'flat' surface.

The sensor signal (s_{ref}) is dependent on the 'flat' mirror commands set (c_{flat}) in that :

$$M\,c_{flat} = s_{ref} \tag{4.1}$$

M is the influence function matrix of the system. Each element of M is defined from the difference between the reference signal and the mirror surface deviation obtained after adding to each mirror actuator a unitary voltage (or command) from the initial 'flat' command (mirror bias).

For P the total number of actuators, and N wavefront samples in the sensor pupil

the influence function matrix M is written as per Equation 4.2:

$$M = \begin{pmatrix} s_{11_x} & \cdots & s_{1j_x} & \cdots & s_{1P_x} \\ \vdots & \vdots & \vdots & \vdots & \vdots \\ s_{i1_x} & \cdots & s_{ij_x} & \cdots & s_{iP_x} \\ \vdots & \vdots & \vdots & \vdots & \vdots \\ s_{N1_x} & \cdots & s_{Nj_x} & \cdots & s_{NP_x} \\ s_{11_y} & \cdots & s_{1j_y} & \cdots & s_{iP_y} \\ \vdots & \vdots & \vdots & \vdots & \vdots \\ s_{i1_y} & \cdots & s_{ij_y} & \cdots & s_{iP_y} \\ \vdots & \vdots & \vdots & \vdots & \vdots \\ s_{1_y} & \cdots & s_{Nj_y} & \cdots & s_{NP_y} \end{pmatrix}_{2N \times P} \tag{4.2}$$

In Equation 4.2, (s_j) is the column vector containing the wavefront sensor x- and y-slopes recorded for the jth actuator. The initial sensor signal for the 'flat' mirror (s_{ref}) is the sensor signal towards which the closed loop will converge. Its optical flatness is comparable to the one of a plane mirror that would be placed instead of the deformable mirror.

In a classical control system, the jth column is the measurement vector corresponding to the maximum voltage applied to the jth deformable mirror actuator, that is, to the jth actuator influence function.

For an aberration described by a sensor signal (s) the ideal mirror command set for correction (c_{corr}) would be given by inversion of Equation 4.1:

$$c_{corr} = M^{-1}s \tag{4.3}$$

However, as M is not a square matrix its direct inversion is impossible. Only using the pseudoinverse of M after singular value decomposition of M retrieves a mirror command that corrects for (s).

The singular value decomposition of M is Equation 4.4:

$$M = USV^T \tag{4.4}$$

In Equation 4.4, $U_{(2N \times P)}$ is the orthogonal base of sensor signal maps, $S_{(P \times P)}$ the ma-

trix of singular values (λ_i) for the decomposition of (s) onto all the modes of $V_{(P \times P)}$ the orthogonal base of mirror commands.

The sensor signal (s) is the phase aberration horizontal and vertical gradient measured with respect to the reference signal (s_{ref}). Tip and tilt aberrations can optionally be removed from (s) by subtracting the mean of each gradient signal. Thus :

$$s = s_{aberration} - s_{ref} - (s_{tiptilt}) \tag{4.5}$$

Assuming tip and tilt do not affect the closed loop image quality, this term ($s_{tiptilt}$) was usually not subtracted in Equation 4.5.

The closed loop algorithm seeks to minimise the signal (s), that is to drive the mirror towards a set of commands for which the sensor sees no difference between the measurement and the reference wavefront. The ideal mirror command for correction of (s) is thus given by Equation 4.6:

$$c_{corr} = V S^{-1} U^T s \tag{4.6}$$

However in practice this correction is implemented using only a finite number of mirror modes and in several iteration steps.

The limit on the number of modes used for the correction is set by the condition number (CN), which is the ratio of the highest singular value to the lowest singular value used in the correction. All singular values of (S) are set to zero beyond this chosen limit singular value. Low condition numbers are recommended for loop stability and speed [112], typical values used were between 20 and 30 modes in our case. With this limit the new singular value matrix (S) is noted (Λ), and the correction c_{corr} becomes :

$$c_{corr} = V \Lambda^{-1} U^T s$$

A code-based clipping of the correction amplitude to half of the maximal voltage is recommended as the large mirror stroke could lead to the membrane break up if two neighboring actuators have an opposite signal or if the actuators voltages remain of high amplitude for more than a few seconds. For security, the manufacturer had

equipped the mirror with an automatic shutdown system avoiding this problem.

At each iteration of the loop a new sensor vector is calculated as in Equation 4.5 and the adaptive optics closed loop updates the mirror as follows in Equation 4.7 :

$$c_{i+1} = c_i - g c_{corr} \qquad (4.7)$$

As the sensor signal measured tends towards the reference signal, the correction required tends towards zero, the mirror commands are stabilized, and the wavefront aberration is corrected.

As seen in Figure 3.8, Section 3.2.2.2, the experimental realization of the pyramid reference signal presents a Gaussian distribution while the theoretical reference sensor signal set expected consists in a uniform zero-amplitude. The mirror shape is controlled by 52 actuators with 16 actuators outside the active pupil, which means the number of actuators (or mirror modes) used in the closed loop control performance requires to be experimentally defined. The membrane deflection formed by a single actuator activation at full amplitude-voltage leads to the sensor saturation. In consequence, the calibration of the influence functions matrix must be performed taking a maximum value what is only a percentage of the actuator full-poke (arbitrarily chosen at 10%). The adaptive optics control law defined by Equation 4.7 however does not account for this mirror command rescaling and in the Mirao 52-d the adaptive optics loop effectiveness revealed dependent on the stabilization time of the voltage applied to an actuator. In turn when the correction voltages were applied too fast to the mirror the adaptive optics diverged, requiring an user-defined adjustment of the gain parameter (g) to a value allowing a stable closed-loop. The usual g=[0,1] gain range of an adaptive optics system is in this work rescaled to g=[0, 0.1]. The notation is adjusted in the following for the reader understanding but the actual values are sometimes mentioned.

The following section is intended to illustrate the dependence of the adaptive optics efficiency towards the reference wavefront, the condition number and gain value used in the control.

4.1.3 Adaptive optics control parameters

This section illustrates the influence of the parameters mentioned previously on the adaptive optics efficiency. The latter is based on the wavefront reconstruction code, a dynamic display of the Zernike coefficients slowed down the acquisition. On the other hand, the off-line reconstruction of long acquisition sequences limited the $in-situ$ experimental adjustment of the parameters value that would have been required. Based on the system point spread function image at the science camera during the calibration and during the ocular experiments, the aberration correction is characterized by the narrowing of the point spread function.

The reference wavefront defines the ultimate closed loop correction quality that can be achieved. Simulations of closed loop efficiency as a function of the condition number value for this mirror have shown a diffraction-limited rms error could be obtained without the need of using all the mirror modes [47]. This point was verified experimentally with a practical test of correction of a typical aberration. The loop destabilization for the correction of a typical aberration with increasing values of adaptive optics gain is presented through the observation of the sensor signal with the closed loop.

4.1.3.1 Reference signal

The reference signals were defined as 'open loop' reference and 'closed loop' reference, which corresponded respectively to the mirror command set used for calibration of the sensor signal and to the mirror command set achieved after implementation of the adaptive optics.

Open loop reference.
The open loop reference wavefront corresponds to the sensor signal recorded with the alignment optics placed at the pupil plane of the eye. The collimated beam at the pupil plane of the eye is propagated to the sensor and thus contains the optical system aberrations. The ocular aberration measured by the system can be expressed including the system aberrations (without subtraction of the reference) or with account of this reference (subtraction of the reference wavefront). In an adaptive optics system these aberrations can be cancelled by an initial bias of the deformable mirror surface experimentally defined. The initial mirror commands 'flat-IE' provided by the man-

ufacturer defined an aberration-free reference wavefront for the commercial system. For an adaptive optics system based on another sensor type a new definition of the 'flat' command was required to correct for the optical system aberrations.
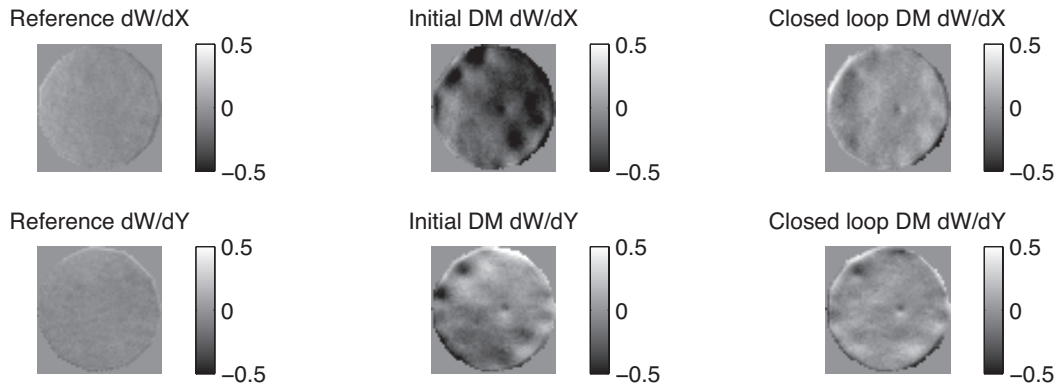
(a) Sensor signals created from 10ms exposure wavefront sensor camera
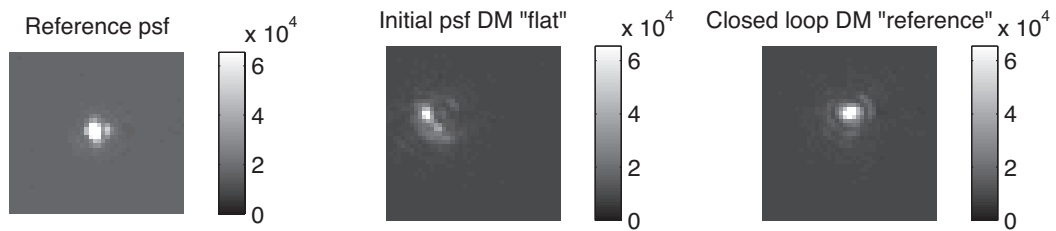
(b) 0.5ms exposure science image

Figure 4.4: Sensor reference signals for the definition of the deformable mirror 'flat' shape in the adaptive optics system with 55samples across the pupil and a $6\lambda/D$ modulation factor. This flat mirror was then removed and the deformable mirror was implemented instead in the conjugated pupil plane. The manufacturer mirror commands defining the 'flat' mirror shape were set up as initial mirror surface bias. A slight shift of the closed loop psf can be observed compared to the reference psf. The uniformity of the reference signal cannot completely be reproduced by the deformable mirror. Edge effects at the pupil are more visible for the deformable mirror than in the pupil signal.

This reference was based on the signal of a plane mirror of $\lambda/10$ optical quality positioned at the deformable mirror plane and using the light of the alignment beam. The sensor signals and psfs for the plane mirror, and deformable mirror 'flat-IE', and 'flat' are presented in Figure 4.4a. Closing the loop on the plane mirror set of reference signals corrected for both the system and the calibration optics. This new 'flat' defined an open loop reference wavefront from which the ocular aberration is measured. The initial calibration of the influence functions was performed using the 'flat-IE' command set and the surface deflection defined using a $\pm 0.1V$ command from this bias.

The adaptive optics closed loop convergence was defined by the plane mirror reference signals. The closed loop was based on 36modes and operated at a gain of 0.01. The quality of the closed loop point spread function was the criterion of success for the adaptive optics.

In the science camera image of Figure 4.4b, one pixel corresponds to 5.36μm of the alignment laser output fibre placed behind the 100mm focal length lens. Each image is 44$\times$44 pixels wide (235$\times$235 μm at the fibre mount). The reference psf diameter was thus 10% higher than the value defined by the Airy function for this wavelength (26μm). Very short camera exposures (0.5ms) were used to record the psf as the calibration laser power was relayed without losses to the science camera. The mirror commands at the end of the closed loop corrected for the optical system aberrations, thus were defined as the 'flat' reference wavefront.

At each initialization of the system the new 'flat' mirror is defined as reference wavefront. After calibration of the influence functions and application of the adaptive optics the closed loop point spread function at the science camera and the sensor signals at the wavefront sensor camera are expected to be similar to their value without adaptive optics. For the quantification of the ocular aberration measurement, the reference wavefront does not need to be subtracted as the system aberrations are already cancelled by the 'flat' command voltages.

Closed loop reference.
The reference signal s_{ref} of Equation 4.1 loaded in the direct slope control algorithm defines the convergence of the adaptive optics. In the pyramid sensor the theoretically 'best' reference signal is $s_{ref} = 0$, which corresponds to an aberration-free wavefront which sub-pupils have an equal intensity. However, this condition also defines a case in which the aberration signal is equally distributed between the 4 subpupils. For the calibration beam, the condition $s_{ref} = 0$ is sufficient to define the 'new flat'. For the eye, light backscattered from the retina and scattered by the ocular media interferes constructively and destructively at the pupil plane to form speckles. The closed loop convergence defined by the equalization of the pupils signal redistributes the speckles in a balanced way within the pupil but does not cancel them. An approximation of the aberration correction with speckled light at the pupil is obtained in an artificial eye with a paper card retina that forms a diffusive media. The retinal image quality after correction was similar for the reference system based on the $s_{ref} = 0$ condition or based on the $s_{ref} = s_{flat}$ condition. The same result was therefore expected in the

eye despite the differences of speckle statistics.

In a Shack-Hartmann, an aberration-free wavefront without speckles at the pupil forms spots centered on the centroid window of even intensity in the focal plane. Aberrations introduce signal non-uniformities due to the signal spread and add local displacements within the centroiding window. Pupil speckles are detected as an additional aberration for a high sensor sensitivity. The Shack-Hartmann fixed pupil sampling and dynamic range parameters limit the aberration measurement to the amplitudes which are not overtaken by speckle strength. In the pyramid sensor, speckle and slight wavefront non-uniformities both appear as wavefront errors at high sensitivity (small dynamic range). The modulation factor increase reduces the aberration measurement sensitivity and in turn the sensor sensitivity to the speckle. This adjustment is major in that the adaptive optics correction can be initiated at a large dynamic range and refined at a small dynamic range when the aberration is small at the pupil.

4.1.3.2 Gain

For most mirrors, the calibration of the influence functions is recorded applying the maximal and minimal voltage amplitude (or command) to each actuator. However, in the case of the Mirao this command leads to such a large stroke of the mirror surface that over the modulation range the sensor measurement is saturated if a voltage of this amplitude is applied. To prevent this, the calibration unitary command is set to only $1/10^{th}$ of the voltage. The correction matrix singular values are thus at $1/10^{th}$ of their value if a unit amplitude was chosen as calibration voltage, which introduces a $1/10^{th}$ factor in the gain value of the software. In an ideal adaptive optics system, the mirror commands correcting for the aberration would be applied in a single step (gain of $g = 1$ in Equation 4.7). However, due to the mirror actuator stroke limit and to the time required to reach the stabilization of the actuator to its defined position, the correction applied in a single step leads to an unstable closed loop.

On a typical static aberration in Figure 4.5 the mean sensor signal over both gradient directions before and after adaptive optics is displayed. The correction observed for increased gain values in the range $g = [0.01, ..., 0.3]$ ($g = [0.1, ..., 3]$ with the rescaling) was showing a limit gain of $g = 0.5$ beyond which the closed loop could not stabilize. To insure a stable correction in the eye, the closed loop gains were thus limited to very small values ($g \leq 0.5$). The typical timescales to correct ocular aberrations were thus within the range 2-5s; a long delay for a dynamic correction with adaptive optics.
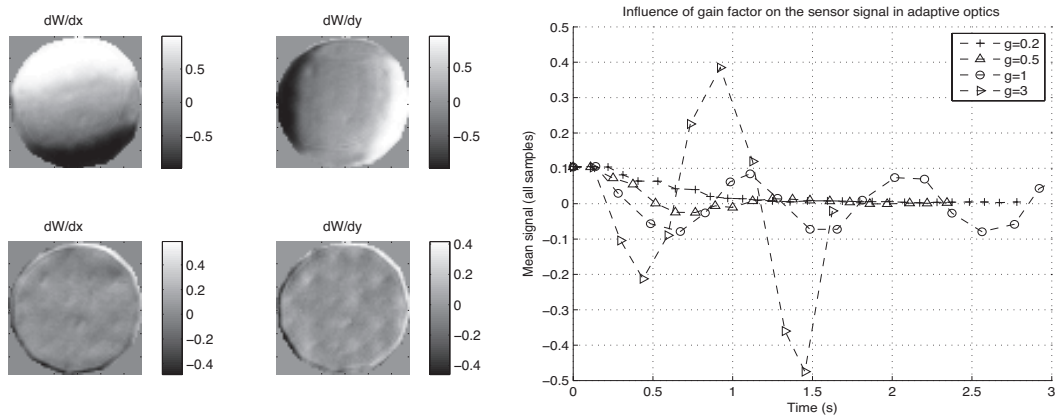
Figure 4.5: Initial and final sensor pupils signal (left) and mean signal (right) with time for adaptive optics applied with varying gain and condition number 40, high-resolution pupil sampling (B1), median modulation ($21\lambda/D$). For low gain value ($g = 0.2$) the convergence is reached in 1.5s while the convergence is reached in 0.5s for a higher gain ($g = 0.5$). The loop destabilization is seen by the oscillation of the signal ($g = 1, g = 3$).

The closed loop gain limit before destabilization should be determined from the system open loop and closed loop transfer functions and bandwidth. Adjustments towards the calibration value $g = 0.3$ value were performed to account for the changes in experimental parameters used as described in Appendix A.

The mirror actuators spatial oscillations resulted in a vibrating membrane and in turn into an additional image blur and loop destabilization factor at the science camera. The timelag between the voltage command application and the actuator positioning was observed only with short-exposure science images acquired with static aberrations and artificial retinas. In long exposure images such as in the eye the mirror oscillations effects on the image were overtaken by the ocular blur. Upgraded versions of the mirror (Mirao-e, [113]) have corrected this effect.

4.1.3.3 Condition Number

In astronomy the generally accepted optimal condition number is given by the number of actuators within the wavefront pupil, that is the number of modes of the correction, or to use for the wavefront reconstruction [114]. For ocular aberration, as the aberration statistics are different from the Kolmogorov model applied to atmospheric turbulence, the mirror characteristics have to be taken into account [45]. For the Mirao, numerical simulations have shown an rms amplitude below 0.1μm is reached if more than 30 modes are taken for the correction [46].

In practice, the computation of a new control matrix or calculations with a large control matrix slows down the adaptive optics. In consequence the control matrix is computed once with a condition number of 30, afterwards only loaded in the experimental sessions. On a single standard aberrated wavefront presenting defocus and astigmatism, the influence of the condition number on the correction of the adaptive optics system is presented in Figure 4.6 for the most commonly used sensor settings (highest wavefront sampling (B1) and median modulation range $21\lambda/D$). As the sensor signal amplitude after correction is constant, it seems that the use of a higher condition number does not improve the correction obtained with 30 modes.
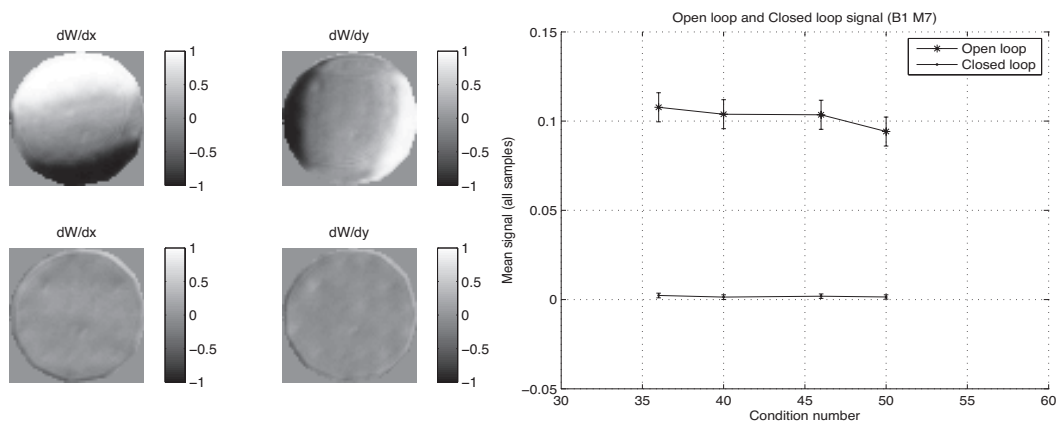
Figure 4.6: The mean of both sensor signals for a single frame describes the amplitude of the wavefront aberration. The amplitude of the standard deviation of the mean show the closed loop wavefront uniformity around zero compared to the open loop signal. A similar efficiency for all condition numbers is reached in the closed loop signal, thus the closed loop convergence for this static aberration is not dependent on the number of modes in the adaptive optics.

4.2 AO system description

The wavefront sensing system and the corrective element of the adaptive optics system have been described previously. In the following, the different subsystems around the adaptive optics are presented. These consist of the pupil monitoring system, the probe beam system, and the Badal optometer. The imaging camera and illumination system are presented further in this work.

4.2.1   Zemax design

In the Zemax design established for the calibration of the modulation amplitudes presented in Figure 3.6a of Chapter 3, the optics of the calibration beam were replaced by a model eye of characteristics designated by the Emsley reduced eye [115]. Due to the adjustments required to increase the pupil diameter at the mirror, or to implement new illumination system, it was difficult to represent the experimental reality with the optical design. An example of use of the design is presented in Figure 4.7. The raytracing aperture stop defining the exit pupil of 6mm diameter was placed at the separation between the ocular media and air. The ocular media was designed as an object of refractive index $n = 1.333$ (as that of clear water), of length 22.222 mm, and of 60 diopters power.

The rays defining the light propagation direction from the aperture in the form of point sources inclined from the optical axis were originated from the back surface of the eye model. The software calculated the resolution limit of the system in the form of the Airy radius parameter for the main wavelength and displayed the rays distribution at the plane considered with regards to this parameter. In Figure 4.7a the point spread function at the science camera corresponded to the Airy disk radius size parameter at 26.9 μm at 530 nm for a 14.4 mm diameter pupil at the imaging lens of 300 mm focal length in Figure 4.7a. In Figure 4.7b, the point spread function at the pyramid did not correspond to the Airy disk radius parameter which was due to the specific design of the pyramid element. The spot diagram in Figure 4.7b showed that the rays remained within the limit defined by a psf of 18.5 μm radius for a 632.8 nm beam and a 4.8 mm diameter pupil at the focus of a lens of 115 mm focal length.

The imaging system was diffraction-limited if the rays distribution remained within the Airy disk. This criterion allowed for example the identification of the angular subtense of the retina imaged at the science camera, limited by the CCD sensor finite size such to $\pm 1.45°$ as in Figure 4.7a for the 632.8 nm wavelength. In Figure 4.7b, an inclination of $\pm 0.5°$ (± 2.2mm at the pyramid) from the model eye optical axis verified the diffraction-limit validity at the pyramid for a 632.8 nm source. This calculation confirmed the modulation at the pyramid did not introduce aberrations for the model eye.

The design confirmed the theoretical magnification and calculation of the resolution limit for the system, based on the definition of the photoreceptors mosaic at the retina of the model eye as an hexagonal pattern which density from in-vitro data [116] was
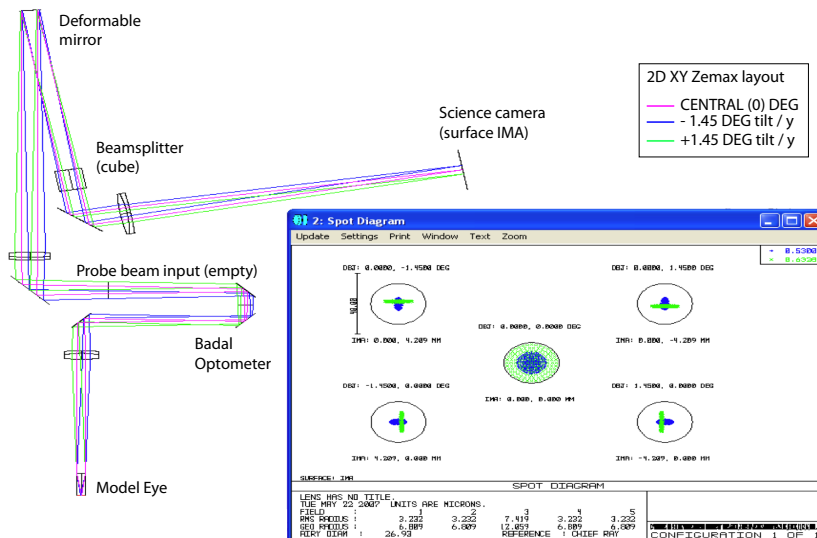
(a) Science design for image subtense in the model eye at the CCD
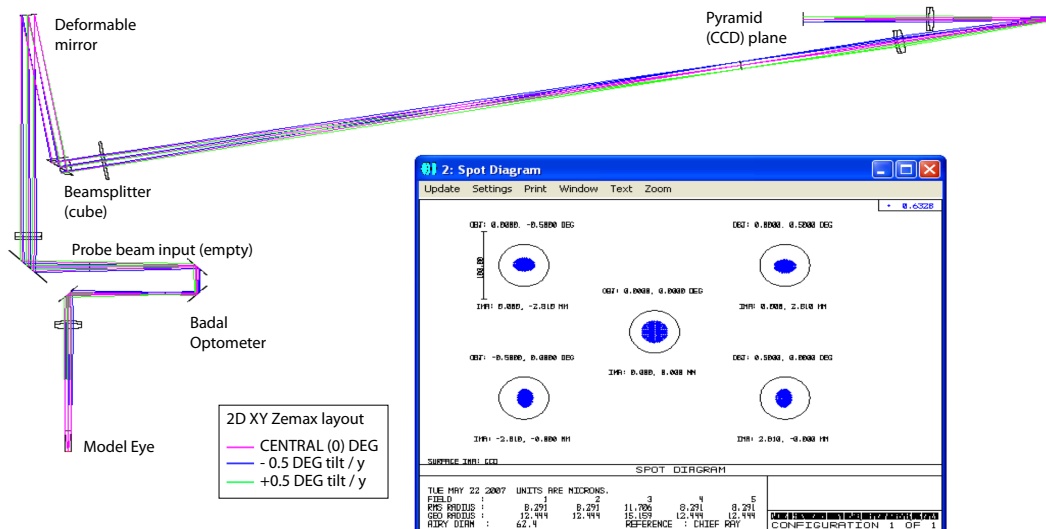
(b) Diffraction limit and angular orientation in the model eye at the pyramid

Figure 4.7: Examples of science and sensor designs realized for the Emsley model eye at 632.8 nm for the wavefront sensing and 530 nm for the imaging wavelength. Adjustments towards the design parameters and plans had to be performed for the practical implementation.

corresponding to a regular pattern of size between 3 μm (density 96 cones/mm^2 at 1°) from the fovea) and 4.2 μm (density 44 cones/mm^2 at 2° from the fovea). This distance corresponded to a resolved pattern for an optical system with a 6 mm circular pupil diameter and a 17 mm focal length in air, which resolution limit was defined respectively by Airy disk radiuses of 2.2 μm and 1.83 μm for 635 nm and 530 nm wavelengths. From the system magnification factors defined between the conjugate retinal planes defined by the eye pupil aperture, the minimal distance between two adjacent point sources in the retina of the model eye was defined by the camera pixels size. For our camera, the distance between two adjacent pixels corresponded to 6.7 μm. The ccd pixels seen from the eye through a circular aperture of infinite size corresponded to a spacing of 0.9 μm in the eye. The two pixels of the imaging system were thus estimated as sampling at the Nyquist limit (2.4 pixels for the 635 nm wavelength and 2.0 pixels for the 530 nm wavelength) the smallest distance between two sources in the eye defined by the 6 mm numerical aperture.

The inversion of the wavefront sensor arm and of the science arm revealed necessary on the bench as the dichoic beamsplitter reflected preferentially the green wavelength. The science camera image plane in Figure 4.7a represented the plane of best focus for both wavelength considered. The longitudinal chromatic aberration for this system was stated from the focusing change between both wavelength. Implementation of a green filter in the science path and defocusing the science camera [5, 6] from the imaging lens was implemented to compensate for this chromatic aberration.

4.2.2 Experimental setup

The wavefront data presented in the following sections were acquired using the system presented in Figure 4.8. The wavefront sensor system has been described in Chapter 3. The retinal imaging system has been described in Section 4.2.1 and will be developed further in Chapter 5 along with the retinal illumination system. The cameras were similar to that described in Chapter 2, Section 2.2.1.

A single computer unit was dedicated to the control of the deformable mirror, retinal illumination and retinal image acquisition, via custom-written software detailed in Appendix A. The probe beam direction and power were defined manually. The pupil illumination and pupil monitoring system remained manually implemented and depending on an additional unit.

Pupil illumination system

The pupil illumination was provided by an assembly of 880 nm infrared LEDs mounted in a ring-shape. The pupil axial position was determined when the iris of the eye was in focus on the pupil camera monitor. The pupil image was captured by an infrared ccd (Thomson, 640x480 pixels) then transferred via a frame grabber to a separate PC operating system. Single frame acquisition only could be realised with this frame grabber. This light source was switched off during the wavefront sensor signal and retinal image acquisition to avoid the presence of an additional source of background light for the wavefront sensor. The pupil monitoring was then based on the backreflection of the probe beam from the retina out of the eye.
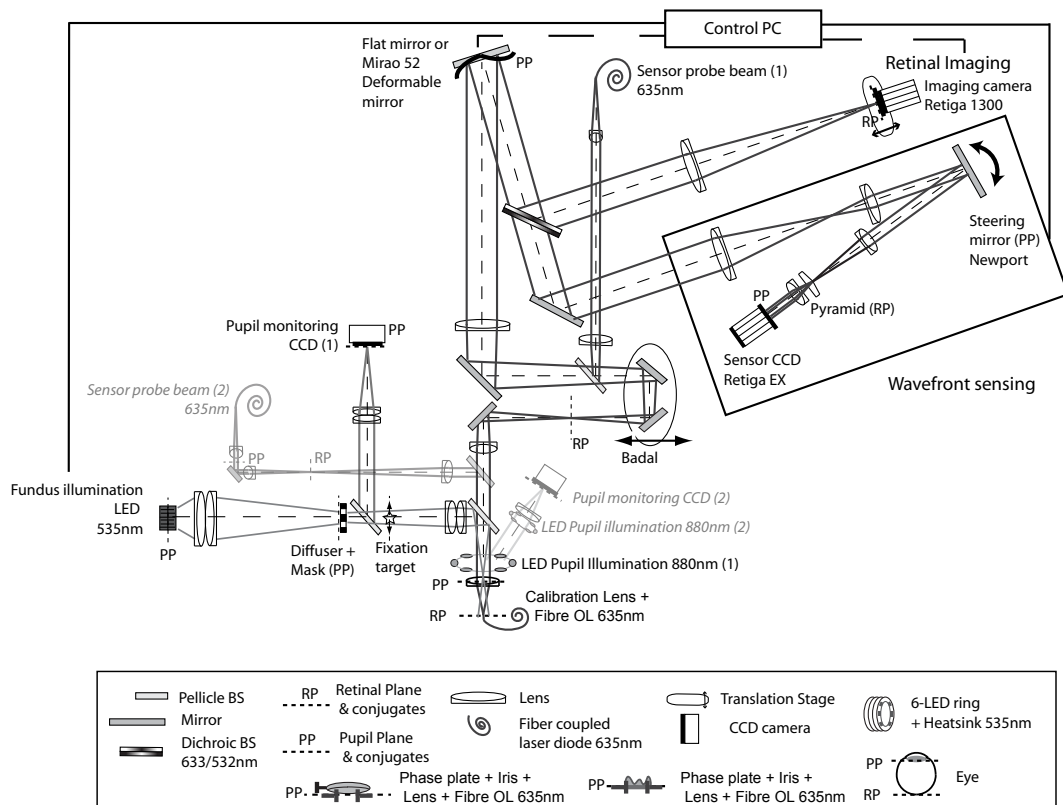
Figure 4.8: Schematic of optical bench with probe beam through Badal stage labeled (1) and pupil monitoring path of Figure 3.5 (Chapter 3) were used for calibration of sensor signal and for closed loop calibration and use in the 5-subjects aberration measurement and psf imaging of Chapter 4. After alignment of the pupil the beamsplitter after the eye was removed as a flip mirror. LED system, grayed out probe beam (2) and pupil monitoring (2) represent the system optics used in Chapter 5.

4.2.3   Wavefront sensor probe beam

The sensor probe beam (adaptive optics beacon) in Figure 4.8 corresponded to a 635 nm fiber coupled laser diode (S1F635C, Thorlabs, USA) collimated by an aspheric lens (Thorlabs FC230FC-B) into a Gaussian beam of 0.9 mm waist diameter after collimation. The beam was demagnified into a 0.45 mm waist diameter at the pupil of the eye by the focusing lens before the Badal and by the first lens after the eye in the system of Figure 4.8. Its input position at the eye was decentered by 1 to 1.5 mm from the center of the optical axis adjusted with the mechanical transverse controls. Its incoming defocus in the eye was set via optical path length adjustment in the relay optics provided by the Badal mirrors. In an ophthalmic system the probe beam replaces the laser guide star used in astronomy, in which light from the object that is observed is often not sufficient for operating a closed loop system in a ground-based telescope. An additional laser (laser guide star) pointing near the star or the light from a brighter and nearby star (natural guide star) can be used for the adaptive optics closed loop systems. The collimated probe beam of small diameter (1-2 mm diameter) sent into the eye exited the eye through a wide pupil (6-8 mm diameter). The central part of the probe focus created the source for the backscattered light and for the sensor signal.

A known technical issue with the laser guide star is an overall tip-tilt of the wavefront sensor signal related to the atmosphere effect on the laser beacon. The effective location of the star is deviated the on the upward and downward paths. The adaptive optics often contains a tip-tilt mirror correcting this effect. In the eye, due to the shift between the visual axis and the optical axis, the probe beam focus was not centered on the optical axis of the system defined by the calibration. As the optics of the eye are not perfect, the sensor measurement contains the aberration of the eye on the forward pass (from the entrance pupil to the retina) and of the exit pupil after scattering, which we designate as the double pass ocular aberration [3]. For the sensor, the wavefront at the exit pupil presented a global tip and tilt in a similar way as the laser guide star backscattered by the atmosphere. The adaptive optics system corrected this wavefront aberration as a whole with regards to the reference of the system, that is including the tip and tilt.

In an artificial eye, a localized high intensity region observed at the pupil was due to the backreflection of the 1-2 mm diameter probe beam from the front surface of the lens. This signal formed a local sensor saturation that represented a region of large wavefront slope, and in turn consisted into an artefact of measurement. In the eye

backreflections due to the tear film and cornea towards the sensor were similarly observed. In both systems the positioning of the probe with a lateral offset from the center of the pupil and with an inclination towards the optical axis direction could be used to project this backreflection out of the system. This configuration also corresponded to the point of entrance leading to a maximal light backscattering from the retina known as Stiles Crawford effect [117]. An overall pupil contrast decrease and a central intensity saturation would be expected from the use of a large diameter probe beam entering the eye parallel to the optical axis and compensated by implementation of a central pupil mask.

4.2.4 Defocus pre-correction by the Badal mirrors

The position of the science camera was initialized at the mid-range of travel for the stage holding the Badal mirrors, retrieving the 'best' image of the calibration beam point spread function. For a dilated eye with the accommodation paralyzed, the collimated probe beam is seen as being at an infinite distance. For a myopic or hyperopic eye, given the aberration shifts the far-point fixation, the conjugation of the collimated beam with the retina is lost. The adaptive optics compensates all aberrations as long as the mirror stroke is not a limit, but the Badal adjustment releases the mirror from defocus correction. The conjugation of the far point with the retina is recovered if the probe beam passes through the optometer. Otherwise the eye sees a defocused probe beam and the wavefront sensor is using a larger probe beam width at the retinal image.

The sensor response to the defocus introduced by the Badal stage on the 6mm diameter exit pupil of the calibration beam was recorded at several modulation factors. Figure 4.9b presents the comparison of results from the sensor and independent measurement of defocus, successively recorded using a set of ophthalmic trial lenses, a Zemax design, and a phase-shifting interferometer :

- The defocus introduced in the calibration beam by the stage micrometric displacement was observed at the science camera. The position of the science camera was initialized at the mid-range of travel for the stage holding the Badal mirrors, retrieving the 'best' image of the calibration beam point spread function. The correction of the point spread function defocusing after the stage displacement quantified the amount of defocus introduced by the Badal displacement.

Inserting at the pupil plane of the calibration beam an ophthalmic lens of appropriate inverse spherical power retrieved the correspondence between the Badal stage reading and dioptres units. The correspondence between the sensor measurement and the ophthalmic refraction had been established in Section 3.3.3.3. Experimentally, the Badal stage displacement was covering over ± 1.5 dioptres of spherical equivalent refraction.

(a) Measurement system for defocus introduced by the Badal with the interferometer

(b) Zernike defocus term measured with the Fisba interferometer and with the pyramid sensor. The squares are the Fisba measurements and the triangles stars mark the pyramid sensor measurement for different modulation (sensitivity) levels.
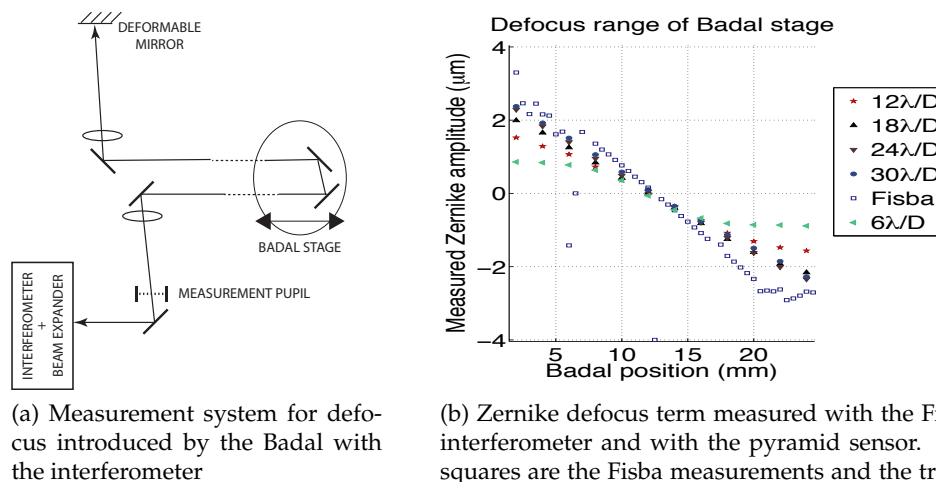
Figure 4.9: Amplitude of Zernike defocus introduced by the Badal stage displacement measured by the sensor compared to the measurement with a phase shifting interferometer. The sensor saturation is consistent with the theory, in the large modulation amplitude a good correspondence of the sensor measurement with the interferometer measurement shows the benefit of the increase in the sensor dynamic range.

- In the optical design software Zemax, the Badal positions that refocused at the science camera the beam issued from several depths in the Emsley model eye were noted. As each depth corresponded to an equivalent shift of the model eye power in dioptres, a relationship between the defocus in dioptres for a 6mm diameter eye pupil and the Badal displacement correction range was established. The simulated correction range in dioptres was consistent with the experimentally measured range.

- Replacing the deformable mirror with a plane mirror of $\lambda/10$ optical quality and implementing at the pupil plane of the eye a phase shifting interferometer system (FISBA OPTIK, Switzerland) as in Figure 4.9a quantified the defocus introduced by the optometer independently of the sensor. The interferometer

beam propagates through the system once to reach the conjugated pupil and once to reach the measurement pupil, thus the defocus at the interferometer pupil is twice the defocus introduced by the Badal shift from the measurement pupil to the deformable mirror pupil. A decomposition of the measurement interferogram into Zernike terms in the Born and Wolf notation is provided by the interferometer acquisition interface (FISBA OPTIK μPhase). The Zernike term for defocus in this decomposition and in the VSIA/OSA guidelines is similar thus the correspondence of the interferometer measurement with the wavefront reconstructed from the sensor measurement for a Badal position can be compared, as in Figure 4.9b. For the modulation amplitudes (6, 12, 18, 24 and 30 λ/D), the Fisba coefficients of the Zernike decomposition are seen as consistent with the wavefront sensor reconstructions of defocus. If the interferometer measurement is considered as the reference, the sensor measurement in the myopic case (positive Zernike amplitude) followed well the interferometer measurement. The difference observed in the hyperopic case (negative Zernike amplitudes) was seen as a normal phenomenon for this optometer type [118].

This observation showed clearly that the sensor measurement was consistent with the ophthalmic refraction, and as well that the sensor measurement was consistent with the optical design. The correction of the defocus over the 6mm pupil of the eye with the Badal was thus demonstrated. The correction of the defocus with the science camera displacement was also quantified, which shows that an in-depth imaging should be possible with the science camera.

4.3 Static correction of phase plates

In this section we show the system response with adaptive optics applied to the phase plates for the configuration of Section 3.3.3.4. The aberration and the point spread function are measured with and without adaptive optics on the four phase plates with the four pupil sampling settings for three dynamic ranges.

The aim of the experiment is to illustrate the sensor closed loop repeatability over the aberration type defined by the plate and over the system parameters (pupil sampling, dynamic range). Repeatability of the measurement for the static aberration is quantified both before and after AO. If a valid approximation of the aberration measurement can be obtained by its average over a series of frames, the measurement is only de-

pendent on the sampling setting and of the dynamic range. This data illustrates the theory developed in Section 3.3.3.2.

4.3.1   Closed loop measurements of phase plates

With adaptive optics, the final wavefront correction depends on the sensor dynamic range, spatial resolution, condition number and gain settings of the control loop. The Zernike coefficients (orders) amplitude describe in that case the sensor noise for this particular mode. In a dynamic measurement with a real eye, a larger variability by Zernike order can be expected given the sensor acquisition can be affected by ocular movements. For a static measurement, the software speed is not an issue and a variability σ_{RMS} of the order of $10^{-3}\mu$m was observed for the open loop wavefronts in Section 3.3.3.4. This stated that the study of one frame or of a set of frames was equivalent for the open loop measurements (that is that the isotropy of the measurement is verified).

Root-mean-square wavefront errors are presented in Figure 4.10 and Figure 4.11 with 50 frames before and 70 frames after the adaptive optics is started for each plate. For all datapoints the rms is calculated without tip and tilt. The mean rms (rms CL) for each dynamic range indicated in the legends are calculated by averaging over 60 rms data reconstructed from corrected frames acquired after the adaptive optics correction (10 frames after the '0'). The closed loop rms quantified the wavefront sensor error in the set of parameters used. The adaptive optics was not always successfully stabilized in the low resolution pupil sampling and high dynamic range. Four of the 48 closed loop measurements were unstable, even after several trials of adaptive optics not all displayed here.

As the adaptive optics initially seemed to correct the phase plate aberration, the destabilization is possibly due to the low pupil sampling resolution and high dynamic range. In those settings, it might be that the sensor does not recognize the aberration after correction as 'corrected' and converges towards a unstable regime (plates 2, 3, 4 binning (3), plates 3 and 4 binning (4), that is in 5 tests over 9). The loop unstability could also be related to the adaptive optics gain and condition number of the control matrix. The adaptive optics gain was 0.03 for all sets thus low enough to expect a stable mirror response. The condition number chosen for all settings was of 30 in input of the adaptive optics control in Equation 4.2, but was effectively of 44±4 after the
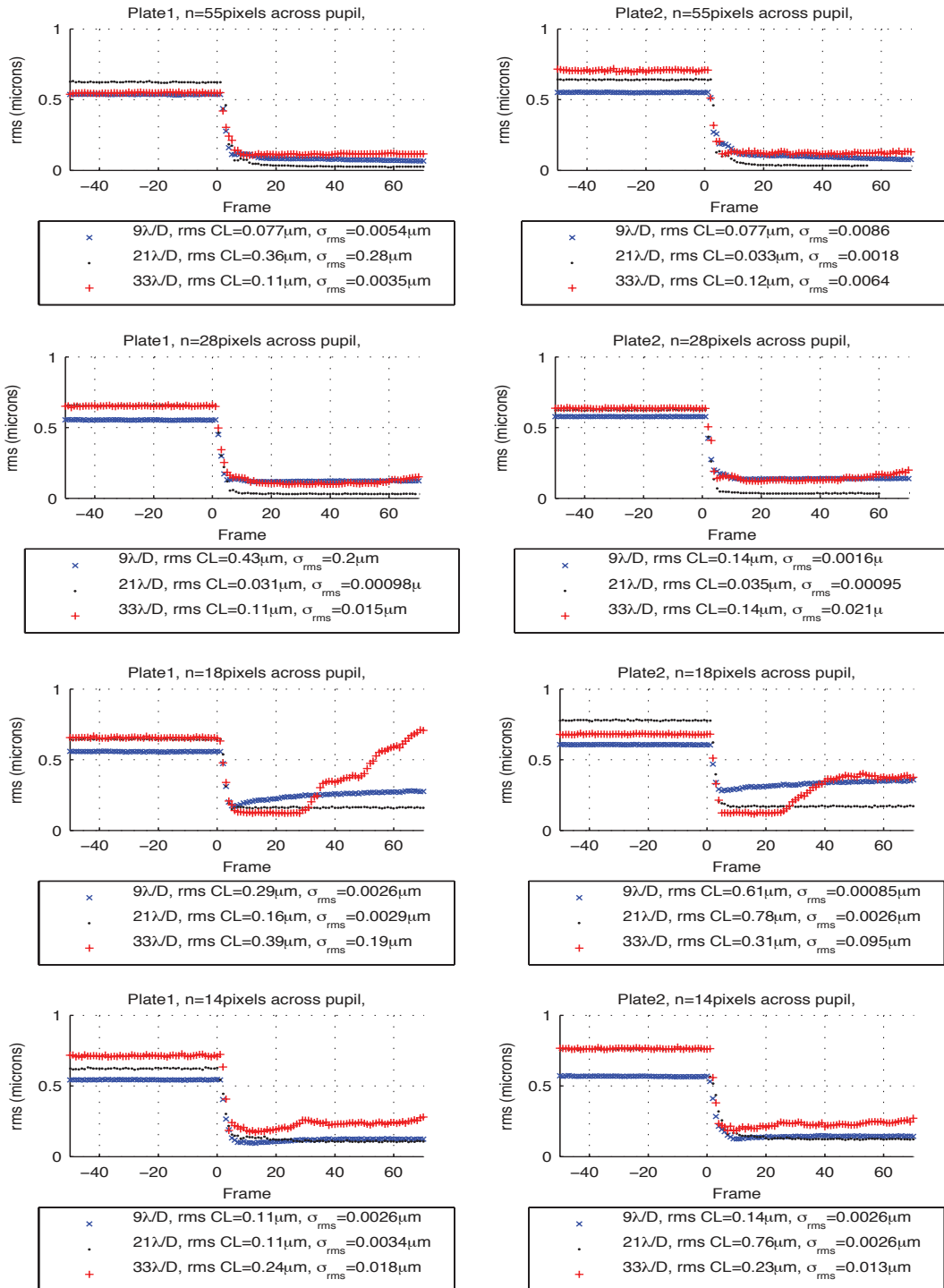
Figure 4.10: Rms timeline for adaptive optics applied to a typical ocular aberration shape in the pupil plane of the eye. Each column is a phase plate. The four rows are four different sensor binnings corresponding to the variation in pupil sampling setting. In each graph the three test sensitivities 9, 21, and 33 λ/D are represented with blue stars, black dots and red crosses.
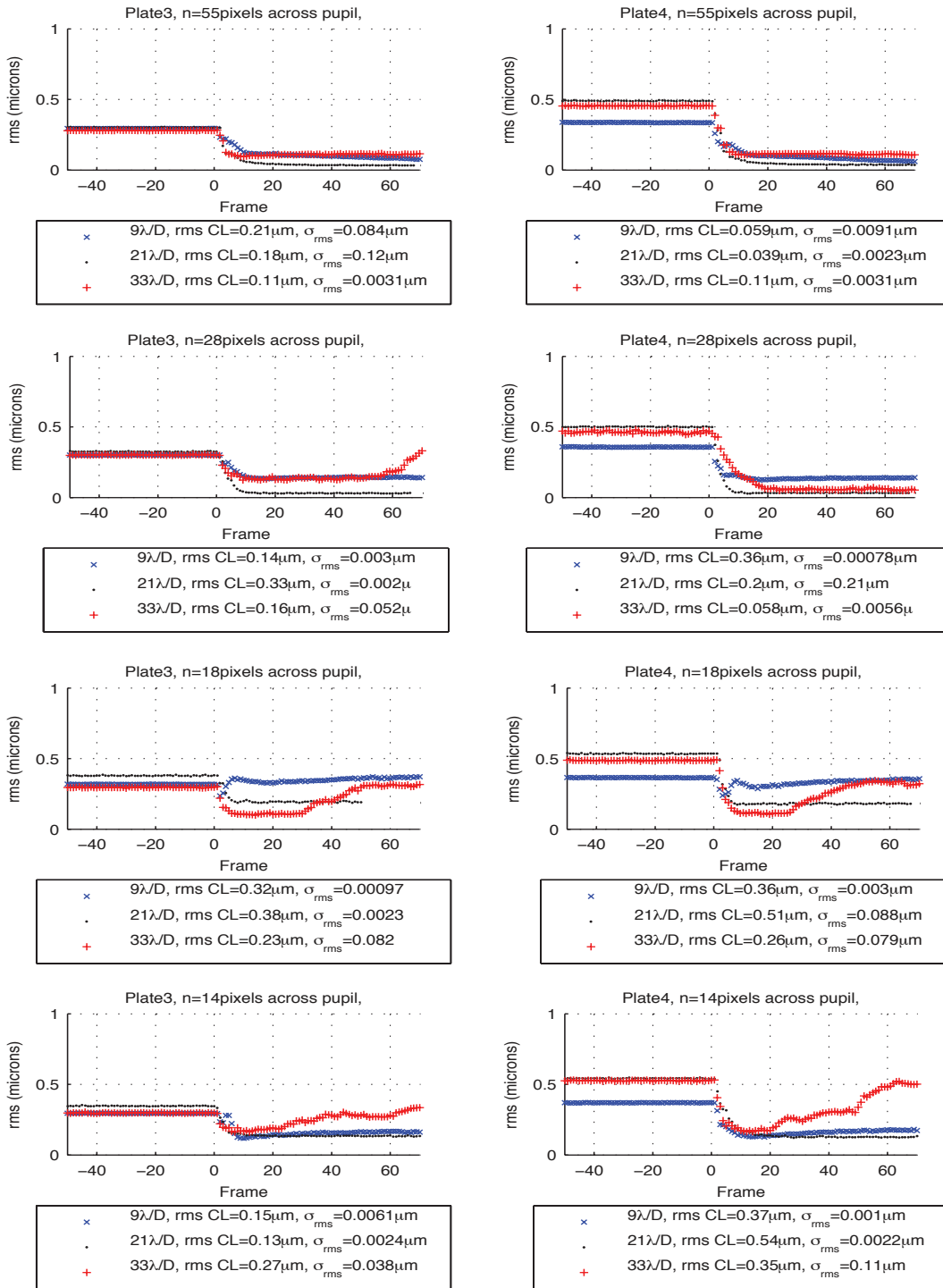
Figure 4.11: Rms timeline for adaptive optics applied to a typical aberration shape in the pupil plane of the eye. Each column is a phase plate. The four rows are for four different pixel binnings corresponding to the variation in pupil sampling setting. In each graph the three test sensitivities 9, 21, and 33 λ/D are represented with blue stars, black dots and red crosses.

97

control matrix was computed. This effective number of mirror zonal modes should have been appropriate, even with the variation due to the small change in sensitivity for each set of binning (B) and modulation amplitude (M).

4.3.2   Closed loop point spread function analysis

For each sequence and each plate, the point spread function before and after the adaptive optics was recorded synchronously with the sensor data so as to possibly relate the closed loop psf quality with the pupil sampling and modulation parameters. The ratio of the psf intensity maximum before and after adaptive optics at constant camera exposure gives an experimental Strehl ratio value quantifying the efficiency of the adaptive optics on the phase aberration. To determine if the closed loop efficiency can really be characterized by the science camera point spread function, a representative closed loop psf was selected for an adaptive optics wavefront at each dynamic range and spatial resolution setting. The average acquisition frequency of the science camera was 10.14Hz±0.27Hz.

The results are presented in Figure 4.12 for 1.6ms camera exposure (8 bits image depth) images acquired at the highest sampling setting (Binning 1, 1360×1280 pixels, 6.45 μm/pixel) and largest dynamic range setting ($33\lambda/D$). A common region of interest was defined around a pixel manually chosen in each closed loop frame as the central reference point. A common area of 50x50 pixels (0.26x0.26 mm area at the back focal plane of the collimation lens in the calibration arm) is defined around the psf centre. As the closed loop point spread functions areas superimpose, it seems that independently of the dynamic ranges and pupil sampling settings the closed loops all converge towards the same type of correction quality. The very small psf width in the high-binning regimes is related to the decrease in the laser power that was meant to keep a constant signal-to noise ratio at the sensor camera. This lack of power could be the cause for the closed loop destabilization in Figure 4.10 and Figure 4.11, in particular at the highest modulation regime in which the light is spread over a larger area at the pyramid than a small modulation regime for a constant laser power.

The two-fold variation in the point spread function size presented in Figure 4.12 shows that a better solution than decreasing the laser power would have been to filter the beam at the sensor - even at the risk to introduce additional aberrations. In addition, the constant area observed for all dynamic ranges after correction at a given

Plate 1, Binning1 Plate 1, Binning2 Plate 1, Binning3 Plate 1, Binning4

Plate 2, Binning1 Plate 2, Binning2 Plate 2, Binning3 Plate 2, Binning4

Plate 3, Binning1 Plate 3, Binning2 Plate 3, Binning3 Plate 3, Binning4

Plate 4, Binning1 Plate 4, Binning2 Plate 4, Binning3 Plate 4, Binning4
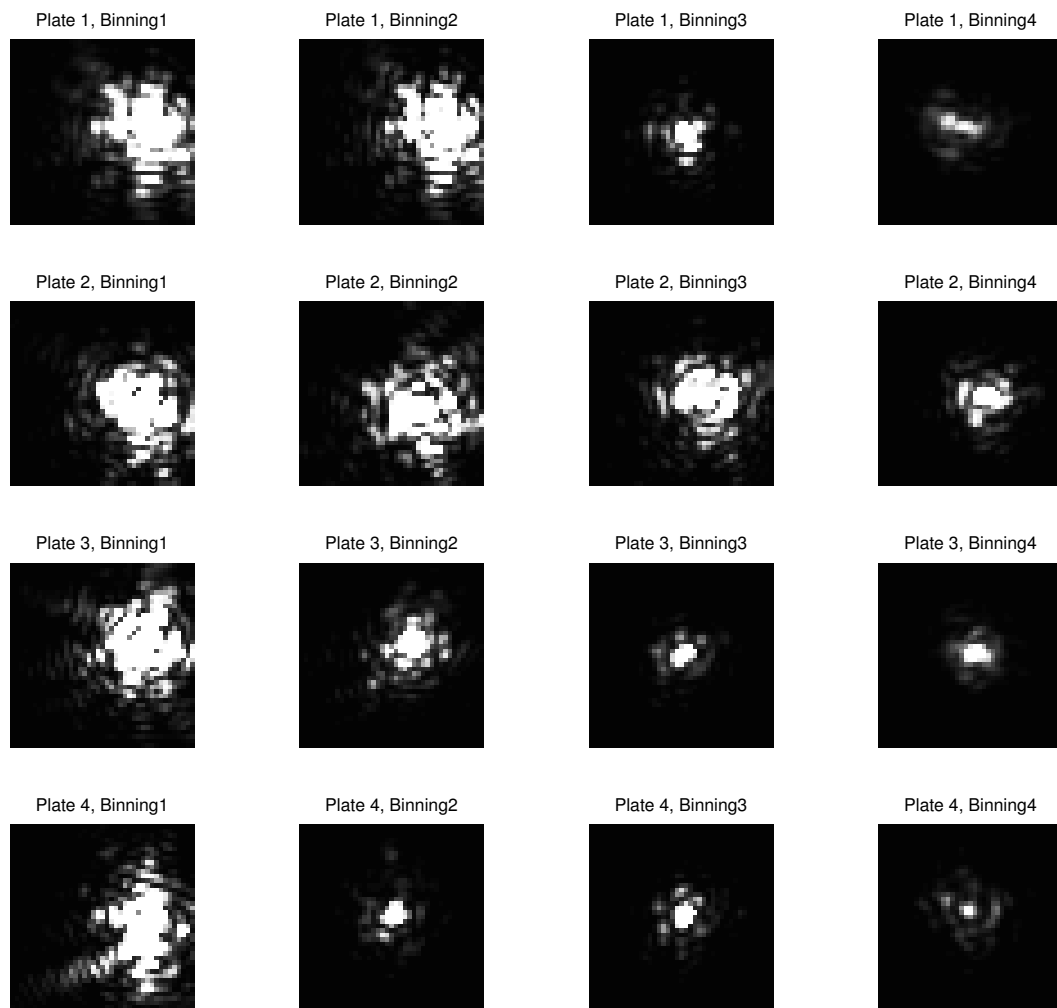
Figure 4.12: Examples of closed loop point spread functions of the Zernike plate no. (1,2,3,4) at modulation $33\lambda/D$ displayed in four rows over a similar colorscale (8 bit range). The four columns correspond to four different pupil samplings. Exposure times at the imaging camera are all 1.6ms except 4.4ms for all binnings of plate No.2. Imaging camera resolution is constant with 1pixel=5.2 μm and Airy radius expected at 635 nm of 2.4 pixels.

pupil sampling seems to show in a first approximation that a similar closed loop correction quality is reached at all dynamic ranges and pupil samplings.

4.3.3   Conclusion: static phase aberration correction

In this section we have seen the adaptive optics correction applied to a set of phase plates presenting typical aberrations. The influence of the pupil spatial sampling and of the dynamic range on the single pass aberration measurement of the phase plate did not seem to limit the sensor measurement. For two of the four plates tested however the tip and tilt of the wavefront amplitude was so important that the aberration measurement was possibly underestimated. The reconstructed wavefront Zernike decomposition was showing only a small variation in all dynamic ranges, thus the sensor was not saturated by this phase amplitude.

The closed loop rms after adaptive optics for each dynamic range and pupil sampling defined the sensor error at those settings. The adaptive optics rms in the high resolution wavefront sensing was generally lower than in the low-resolution sampling, which corresponds to the loss in measurement accuracy with the wavefront sensor binning. The closed loop unstability in the binned settings of the wavefront sensor camera corresponded in our view to the lack of light for an appropriate sensor operation. The laser power decrease was illustrated by the presentation of the adaptive optics point spread function observed at the science camera showing the reduction in laser power at 1.6ms exposure was significantly decreasing the psf image width.

4.4   AO in the eye

To further validate the aberration measurement variation in the eye the measurement of the ocular aberration across the dynamic range was performed with the results for 4 subjects presented here, and for an additional subject in which the ocular aberration was recorded on another set of modulation factors and that was discarded from this study.

4.4.1   Wavefront aberration measurement

The eye was dilated using a drop of Tropicamide 1% ophthalmic drug. During the time delay of 5-30 minutes when the pupil was dilating the subject's bite bar was made. Putty paste or wax bite bars were used, both consisting of a solid dental impression of the subject designed to maintain the head's position stabilized over the measurement duration. Once the accommodation was frozen the subject's head was aligned through positioning of the bite bar mount installed on a 3-axis translation stage itself fixed to the optical bench, which fixed its position relative to the optical axis of the system.

Sequences of 5 seconds of open loop measurement and 5 seconds of closed loop measurement were recorded for 3 values of modulation factor within the sensor maximal and minimal modulation range. The rms traces over time were initially calculated including all the terms of the Zernike decomposition - that is also with tip and tilt. These data for the 4 subjects are presented in the upper part of Figure 4.13. In the average Zernike decomposition over 10 frames in open-loop the tip and tilt amplitudes were identified at their saturation values and thus as taking over on all other terms in the rms traces here. The tip and tilt amplitudes are respectively presented in the lower part of Figure 4.13. As mentioned in Section 3.3.3.4, for aberrations measured with tip and tilt saturation amplitudes, the Zernike decomposition was maybe not properly characterized.

To know if the aberration measurement in open loop at a given modulation was saturated the relationship between the maximal measurable wavefront amplitude and the decomposition term is necessary. The dynamic range adjustment of the pyramid sensor for the ocular aberration was in turn highlighted. To identify if a range measures reliably the aberration, the amplitude must also stand above the measurement noise. In this system, the closed loop amplitude of a Zernike term was defined as the noise level for this term at the modulation amplitude considered. The difference between the higher-order terms amplitude before and after closed loop was however too small to all the identification of if the maximal wavefront aberration was reached for this order.

With only 3 modulations factors tested it is possible that the best sampling dynamic range for the aberration would not appear. The wavefront tip and tilt amplitudes were determined by the position of the probe beam on the retina from the closed loop reference, thus the pre-correction of the beam position should have been applied. In-
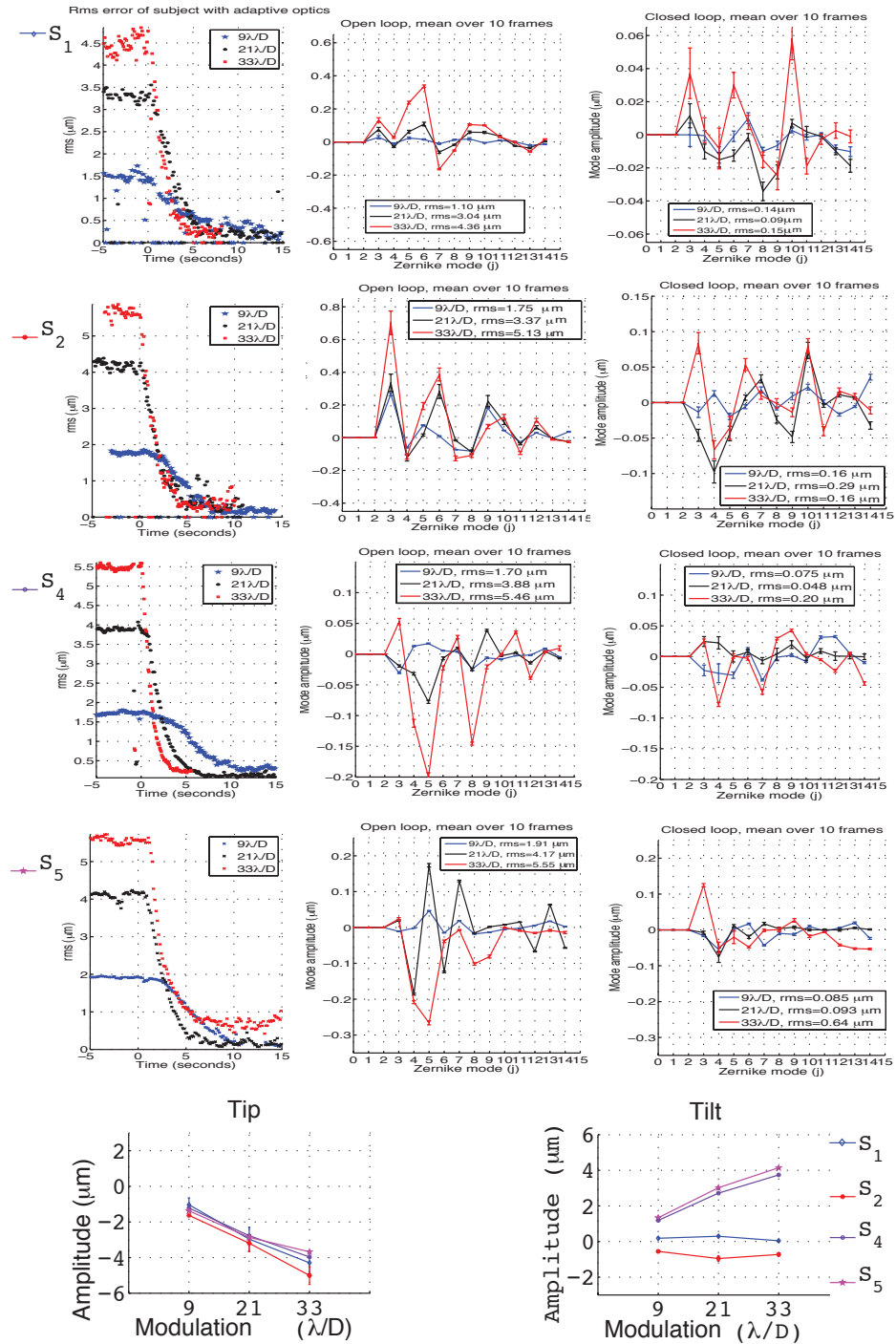
Figure 4.13: Column 1: RMS error over time. Column 2: Open loop Zernike decomposition for 4 subjects. Column 3: Closed loop decomposition for 4 subjects. Each order of the decomposition corresponds to a 10 frames average taken within the rms in open loop and in closed loop for Column 1. Tip and tilt amplitudes for open loop in each modulation factor are presented in the lower part for each subject $S_{1...4}$. Tip-tilt saturation amplitudes for 9, 21 and $33\lambda/D$ are respectively $|1.4|$, $|3.4|$ and $|5.3|$ μm.

stead of maintaining the same probe beam orientation for all subjects, a customed adjustment of the probe beam direction in the pupil and position at the pupil should have been performed by adjustment of the probe beam assembly transverse controls. Nevertheless, due to the deformable mirror stroke amplitude, the sensor saturation did not stop the adaptive optics to operate. The lack of saturation detection did not represent a problem for the adaptive optics given the high stroke of the mirror corrected most of aberrations. However, this had the disadvantage that the experimental parameters adjustment required to obtain a proper ocular aberration quantification was not performed before the closed loop was started, and second, that the closed loop sometimes revealed unstable .

In conclusion the mirror wavefront correction capability corresponded to the expectations. Given the amplitude of the error bars in this dataset, the assumption that the sensitivity range evolution is of benefit for the measurement of a given azimuthal order of aberrations cannot be verified. For the low speed of the acquisition system with typically 5 Hz to 10 Hz for the 56 samples across the pupil (each sample measuring 107 μm at the eye), it is likely that the temporal variations of an order would introduce errors in the characterization.

The second probe beam system was designed so that the probe beam tip and tilt could be readjusted on the retina in order to limit the aberration correction to the higher-order terms. The incoming defocus could not be controlled as finely. A wider closed-loop probe beam image in the eye was observed.

4.4.2   Point spread function

Due to the diffusive properties of the retina, the probe beam image was widened when observed in the eye compared to its observation after reflection onto a glass substrate, a metallic surface, or a paper card. During the system alignment, closing the loop on the probe beam shined on the metallic mount and acquiring the flashed-image of the closed-loop image consisted the proof that the science camera was aligned with the adaptive optics. The best image plane for the adaptive optics on the calibration beam in the red thus corresponded to the best focus plane for the red in the retina.

In the eye the adaptive optics was recorded without changing this camera position. The assumption was that the adaptive optics system was taking the highest level of

intensity to calculate the correction, and bring the focus to the corresponding layer of the retina. The point spread function images for the 4 subjects presented in Section 4.4.1 are presented in Figure 4.14. The first two subjects S1 and S2 were imaged using a 16 bit depth science camera image at the highest camera image resolution at 50 ms and 20 ms exposure and default camera gain (1016/4095 arbitrary units) while subjects S4 and S5 were imaged using an 8 bit image depth, the highest camera binning and 5 ms exposures. The lower signal to noise ratio observed in S5 is attributed to its darker eye color compared to the three other subjects as the laser power was set constant at 2.5 mW power. All images show a 48×48 arcmin field in the eye using a higher zoom factor for the subjects S4 and S5. The shift between the open loop position and the closed loop position pointed by the centroids is of similar amplitude for all the subjects and of 12.6 arcmin (63×63 μm for an eye length of 17 mm).
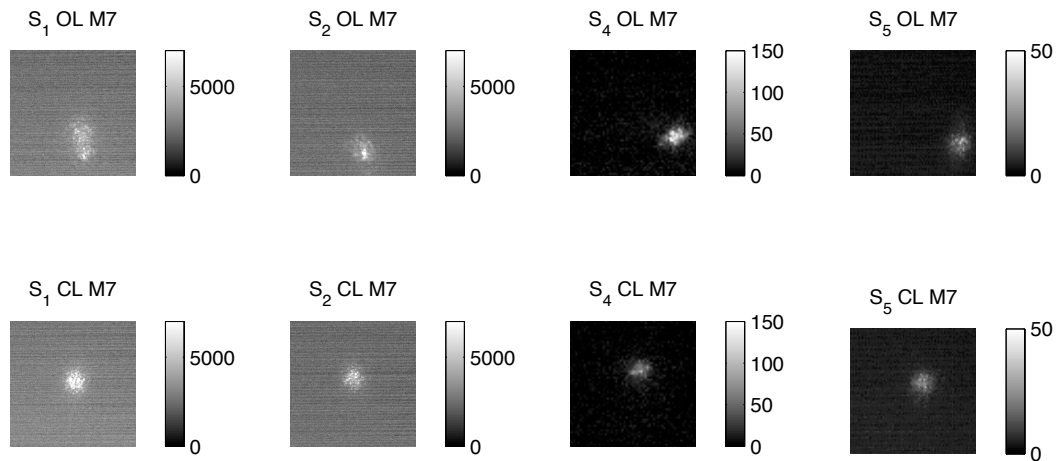
Figure 4.14: PSFs displacement for the 4 subjects without adaptive optics (OL) and with adaptive optics (CL). The lateral shift of the double pass closed loop measured with a centroid algorithm corresponds to tip and tilt amplitudes leading to the wavefront sensor saturation. Closed loop signal diameter measured with a centroiding algorithm of 40μm ($\simeq$8arcmin).

This constant shift was consistent with the constant laser position and angular shift that was measured for all the subjects in this configuration and that had been fixed after measurement of the first subject (S3, treated separately in the following of this Section).

The adaptive optics was run in the eye of subject S3 for the highest pupil sampling (56 pixels), a condition number of 30 modes, a gain of 0.01 and an initial science camera exposure of 100 ms. The modulation amplitudes used in his measurement were different from the amplitudes used in the eyes of other subjects, and are thus

presented separately in Appendix C. The defocus correction was achieved with the Badal optometer by translating the mirrors stage in the direction of the psf compactness, then the rest of the aberrations was corrected with the adaptive optics. The camera exposure was then reduced down to 10 ms, a level that avoided the camera saturation.

Figure 4.15 shows the psf improve at the science camera. Without adaptive optics the laser light is spread over a large area and contains speckles (an image pixel in Figure 4.15 is 3.6 μm in the eye) thus a white bright speckle of 4 pixels diameter is 14.5 μm diameter (3.2$\times$3.2 arcmin or 0.05°$\times$0.05°). At shorter exposure, the psf signal out of the background image is reduced to a 61$\times$61 μm (12$\times$12 arcmin or 0.24°$\times$0.24°) zone pointed by the red square centered around the maximal gray level pixel.

(a) Open loop 100ms   (b) Closed loop 10ms
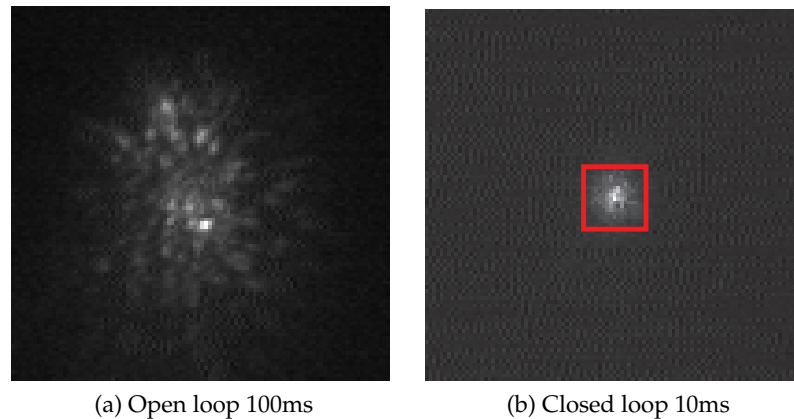
Figure 4.15: Adaptive optics in the eye of 1 subject with deformable mirror at 100ms open loop and 10ms closed loop. Image field 360$\times$360 μm in the eye. Red square represents a 61$\times$61μm psf signal out of the background gray level.

Given the camera exposure times used and the size of the camera pixels, the signal of the open loop image cannot be attributed to the photoreceptors. In closed loop, the psf size corresponds well to the Airy radius of a diffraction-limited beam of 0.45μm diameter observed behind a 17mm model eye length at 635nm. The psf profile however does not fit to an Airy shape unless buried in the noise.

The double pass point spread functions before and after adaptive optics were then recorded at various settings of exposure (20, 25, 50ms) and camera sampling (B1,B2, B3). From these observations the open loop point spread function presented constant intensity distribution patterns and the closed loop point spread function compactness was constant.

4.4.2.1 Single frame exposure dependence

For the modulation factor $9\lambda/D$ the camera frame was binned into a 2x2 scheme during the experimental acquisition. Each frame was imported in Matlab and resized into the dimensions of the camera chip (1x1 binning) by bilinear interpolation for consistency with the camera chip highest resolution. A graylevel value from an unexposed corner of the camera is subtracted from the image levels.

A common region of interest of 100x100 pixels was defined around the first maximal image pixel graylevel detected by Matlab. From geometrical optics each pixel of the camera represented 0.9μm (or 0.18arcminutes) in the eye, the frames were thus cropped over a region of 20x20arcminutes in the eye. The Matlab image display was performed over the graylevel image range, from the maximal level to the minimal level. The signal did not fill completely the 2^{16} level image range, but was distributed in open loop over $1/6^{th}$ of the range and in closed loop over $4/6^{th}$ of the range. This improvement in signal to noise ratio was due to the adaptive optics. The increase in exposure for both the open loop and closed loop image presented less speckle in the long exposures. Long exposures thus acted as an averaging effect for the image signal.
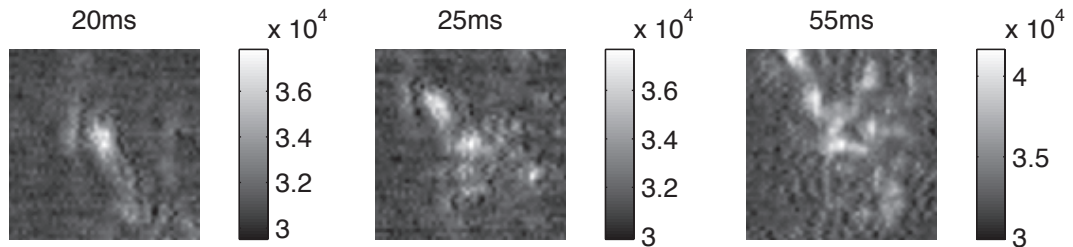
(a) Open loop PSF
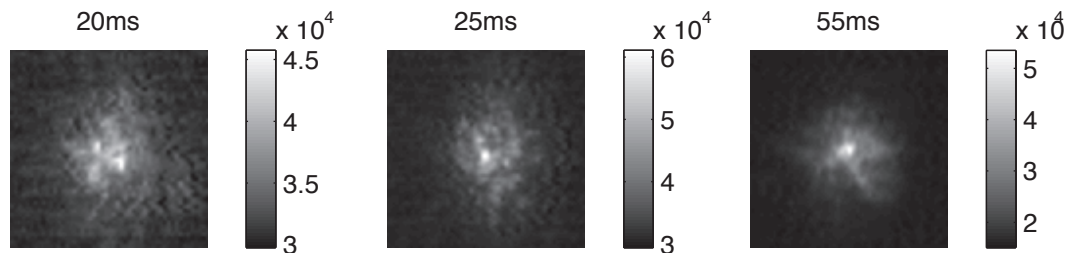
(b) Closed loop PSF

Figure 4.16: Single frame open and closed loop psfs images acquired at exposure 20ms, 25ms, 55ms. Each pixel of the image is 0.9μm in the eye. Each frame represents a 20×20arcmin region in the eye.

4.4.2.2 Single frame modulation dependence

Single frames extracted from a sequence were used to observe the closed loop effectiveness as a function of the modulation factor. 20ms exposure frames recorded at a constant laser power of 2μW were studied. The science camera binning factors for modulations M3 and M7 were respectively 3x3 and 2x2, while for the M11 factor the full camera chip was recorded. A graylevel value from an unexposed corner of the camera image was subtracted from the raw frame resized by bilinear interpolation into the size of the full camera chip. A region of interest of 20x20arcminutes was defined around the pixel of maximal intensity detected in the frame, in Figure 4.17a for the open loop and in Figure 4.17b for the closed loop.

In open loop for all modulation factors a similar psf elongation and division into two secondary sources was observed. As the binning decreases the signal to noise ratio decreases in the camera image, and the double pass psf is more difficult to distinguish from the image background signal. The binning reduced the speckles as each pixel was the result of the averaging over NxNpixels of the camera chip.

(a) Open loop PSF
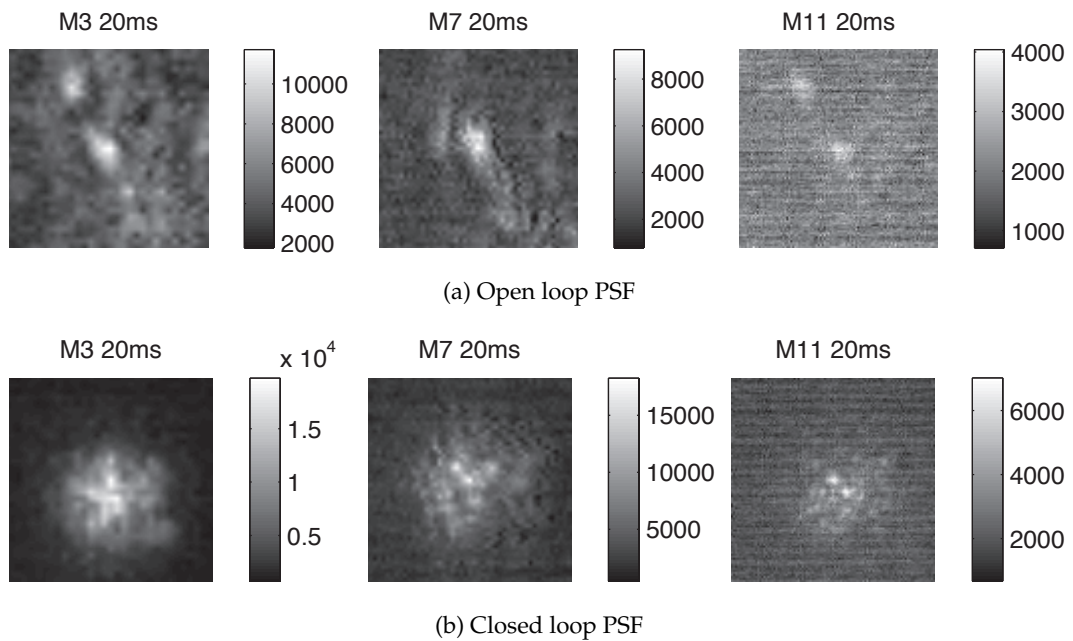
(b) Closed loop PSF

Figure 4.17: Single frame open and closed loop psfs for M3($9\lambda/D$), M7($21\lambda/D$), M11($33\lambda/D$). Each pixel of the frame is 0.9μm in the eye.

The doubling of the psf core in the frames studied could disappear due to the binning in the other frame or due to the closed loop quality. The quantification accuracy im-

provement theoretically obtained after average over several frames revealed limited by the recentering method chosen in the averaging process, not presented here.

4.5 Conclusions

This Chapter presented the corrective element of the new adaptive optics system, and its implementation in an adaptive optics loop. The adaptive optics efficiency was tested on a set of static aberrations. The optical system for the measurement and correction of the ocular aberration was described. The influence of the defocus pre-correction with the Badal mirrors was discussed. Preliminary images of in-vivo correction of the double-pass ocular psf were presented.

Wavefront sensing measurement
For a dynamic operation the aberration pattern measurement for a young and not very much aberrated eye was performed in three typical dynamic ranges of the sensor. The aberration patterns showed to be relatively similar in all dynamic ranges but the Zernike decomposition study could not lead to determining for sure if a dynamic range was better suited for describing the particular amplitude of one Zernike mode for the pattern observed. Assuming that more frames would better characterize a variation of the Zernike term with time, a faster acquisition would be of interest.

If the adaptive optics system correction efficiency must be expressed only in terms of point spread function extent at the science camera image, for the system presented here the correction obtained here is much more efficient than in the initial system [1]. Given both systems used a similar number of lenses, the aberrations introduced by the system were of similar amplitude. For a similar exposure used at the science camera the improve in the psf size confirmed the deformable mirror was able to correct the full ocular aberration.

The closed loop average rms was of 0.1 μm after correction. This relatively high value was related to the choice of adaptive optics control parameters of gain, condition number, influence function calibration, and reference wavefront, which were experimentally defined. Those amplitudes however seemed close to the values of rms error expected according to the simulation studies [47] for the number of modes used. At 38 Hz maximal speed during coupled acquisition of the imaging camera and wave-

front sensor signal, instead of 55Hz acquisition of the wavefront sensor signal only, the code speed for the adaptive optics was slowed down by the science camera acquisition. Use of high-speed CMOS sensors or other CCD sensors to replace the cameras was not feasible in this work.

Adaptive optics efficiency

The adaptive optics efficiency has been observed for a single frame and for several subjects at multiple camera exposures in the eye. The science camera binning (imaging resolution) reduced the signal speckles detected in the high-resolution image of the static point spread function by introducing a blurr effect. In open and closed loop it was impossible to state from the single frames if the use of a more sensitive modulation factor led to a better or more compact point spread function. The AO efficiency was therefore said independent on the dynamic range of the sensor for the aberration studied and for the frames considered.

The improvement in the signal to noise ratio for a single modulation factor (dynamic range setting) at long exposure resulting from an averaging over several single frames was shown to be beneficial only if the average frame was obtained by selection of typical AO-frames. In that case the psf signal could be compared to the focus of a gaussian beam backreflected by the retina, and the speckle structures appearing in the average image were observed to be of similar size as other observations of outer segment cells.

Chapter 5

Imaging with the adaptive optics fundus camera

5.1 Imaging system

We present in this section the retinal imaging system that has been built for imaging in the eye. The aims of this system are to retrieve a retinal image of sufficient light level to allow the focusing of the science image at the appropriate layer in the retina, and to acquire a sequence of flashed images. The short exposure flashed images sequence is a requirement for image post-processing operations to be performed and a good signal-to-noise ratio image of interest for the clinician.

5.1.1 Design of the retinal imaging

The cone mosaic at the retina is considered as an array of hexagonal sources of side 2μm at the highest density (fovea) and 10μm in the periphery of the fovea, from 2 to 10 degrees. From the object plane to the image plane, the system's ability to transmit information is defined by the optical transfer function (OTF). Assuming the system is linear in intensity as the illumination of the LED is spatially incoherent, and that the image field remains within the isoplanatic angle of the system, the transmission of the spatial frequency content is expressed by the convolution of the object function (H) with the system point spread function (P).

For (I) the image signal :

$$I = H \otimes P \qquad \xrightarrow{\widetilde{F}} \qquad \widetilde{I} = \widetilde{H} \times T \tag{5.1}$$

where $\otimes$ defines the convolution, $\left(\xrightarrow{\widetilde{F}} \right)$ the Fourier domain transformation and $\times$ the scalar multiplication. The Fourier transform of the point spread function (P) is the optical transfer function (T). Its modulus is the modulation transfer function MTF which defines the optical system's ability to transfer optical information. The highest spatial frequency of the system, defined by the cutoff frequency of the optical transfer function, is the size of the smallest feature of the object that appears in the image observed through the generalized pupil. Following the Nyquist criterion, the highest spatial frequency of the object must appear onto at least two image samples in the image plane [119]. For an object like the cone mosaic a pixel of the camera must in turn represent a maximum of 1μm in the eye.

The light comes from the specular reflection of the illumination of the hexagonal array of photoreceptors, which become secondary sources forming the image. A first optical relay formed by the first lens of focal length (f=125mm) after the eye and the lens of the eye creates a conjugate retinal plane in the system before the Badal optometer. For the Emsley reduced model eye, the length is l=22.2mm and the vitreous refractive index n=1.33, thus the equivalent focal length in air is of f'=16.7mm. In this conjugate retinal plane the magnification of the retina is given by the ratio of the focal lengths:

$$\frac{f'}{f} = \frac{125}{16.7} \approx 7.5 \times \tag{5.2}$$

The smallest image detail visible in this conjugate image plane is defined by the spatial frequency cutoff (f_c) of this optical system. Any information beyond this frequency content is blocked by the eye lens. Thus :

$$f_c = \frac{w}{\lambda f} \tag{5.3}$$

In Equation 5.3, w is the radius of the pupil, $f = 16.7$ mm the model eye lens, and λ the wavelength.

For a 6mm diameter eye pupil in the green (540 nm), this gives $f_c = 332$ cycles/mm. In the Gullstrand Eye model, for $f = 17$ mm the conversion factor between cycles/mm

and cycles/degree is 0.3 mm/degree. The cut-off frequency in degrees is thus $f_c =$ 332 cycles/mm $\times$ 0.3 mm/degree which corresponds to a periodic pattern of approximately 99.6 c/deg [120]. For a 6 mm diameter eye pupil in the red (635 nm), following the same principles, f_c = 283 c/mm, and in degrees f_c = 85 c/deg.

Comparing the cutoff frequency of the imaging system with the cutoff frequency of a system used for imaging the photoreceptors power spectra which presents an intensity peak at 150 c/deg [2], this means our system should be able to sample the retinal mosaic as f_c is beyond the Nyquist criterion for an array of retinal cells of 2 μm spacing.

A better sampling would be obtained by an increased number of pixels in the image only possible with a smaller pixel size at the camera or by optically increasing the magnification and decreasing the field-of-view. We note that when analyzing the retinal mosaic across the field the size of the analysed part of the image must be chosen carefully given its high variability across the retina, shown in Figure 5.1, first observed by histology and confirmed by in-vivo studies [116, 121].

The frequency cut-off means the smallest feature that can be relayed through the eye optics are also limited by the numerical aperture of the eye. If one wants to observe a cellular feature of higher spatial frequency than these cutoff frequencies the only solution is to design an imaging system whose point spread function in the eye is smaller than the natural values. This is performed to a certain extent in a confocal system using a pinhole in a conjugate retinal plane or at the plane of the photodiode cell. The pinhole squares the Bessel first order point spread function signal and in turn the smallest spacing required to resolve 2 adjacent neighboring sources is reduced. Without pinhole the diffraction limited point spread function of the imaging system is classically defined by the Airy disk.

5.1.2   Illumination

The illumination path design is presented in a general manner here, as the several versions were implemented. The optical design is similar to the Köhler system used in microscopy, using the conjugation of the source to the cornea to illuminate the retina in Maxwellian view. An iris in a conjugate plane defines the retinal extent of the illumination at the retina, and a custom-designed fixation target printed onto a
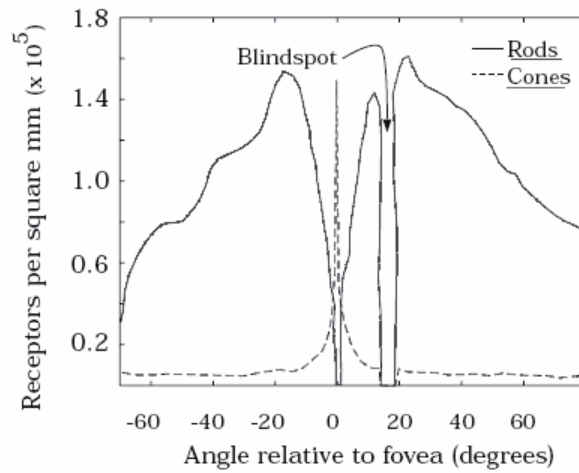
Figure 5.1: Distribution of the retinal cones density, from [122]

transparent plate defines the retinal extent imaged at the camera.

Figure 5.2 shows the principle of the reimaging system. Lens arrangements (L_1, L_2) and (L_3, L_4) have equivalent focal lengths f'_{eq0} and f'_{eq}, and the eye is approximated by a sphere of refractive index (n). The field iris defines the angular illumination at the retina. The fixation target defines the position imaged in the retina after the eye is rotated to observe the fixation mark. The movement of the eye is admitted equal to the angular distance defined from the optical axis center. The mask external radius h_{ext} is reimaged into a mask image of external radius h'_{ext} at the cornea. The field iris aperture size Φ_w and output divergence angle α_{wanted} sets the size and divergence Φ'_w and α'_{wanted} of the illumination at the retina.
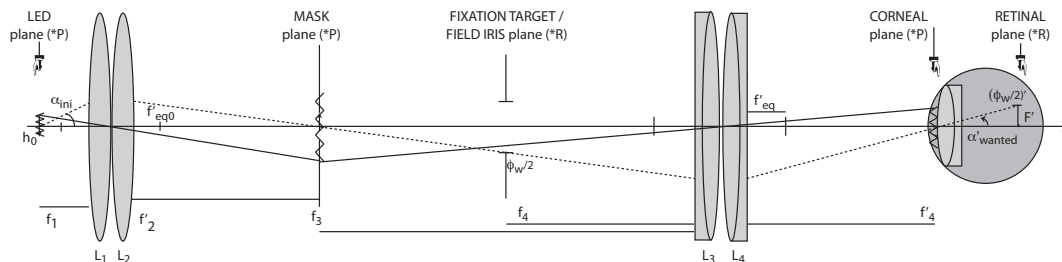
Figure 5.2: Schematic illustration of the illumination system designed using a geometrical optics. First relay of the LED is based on singlets as the intensity transmission is the main concern while second relay is based on doublets for better viewing of the fixation target.

The fixation target as presented in Figure 5.3 is made of a set of crosses positioned in

steps of 1 degree around the centre of the image field in the conjugate retinal plane. The central part of the field is kept clear of any cross to observe at best the image within the isoplanatic angle of the adaptive optics correction. Its size in the conjugate retinal plane is calibrated using a mark printed at 1mm of the centre of the optical axis onto a transparent support. At the retinal plane of an artificial eye is placed a Linos reticle that verifies the conjugation of the retinal plane with the camera plane. Rescaling the angular extend behind the artificial lens and a model eye lens, the target defines a $1°$ fixation mark.
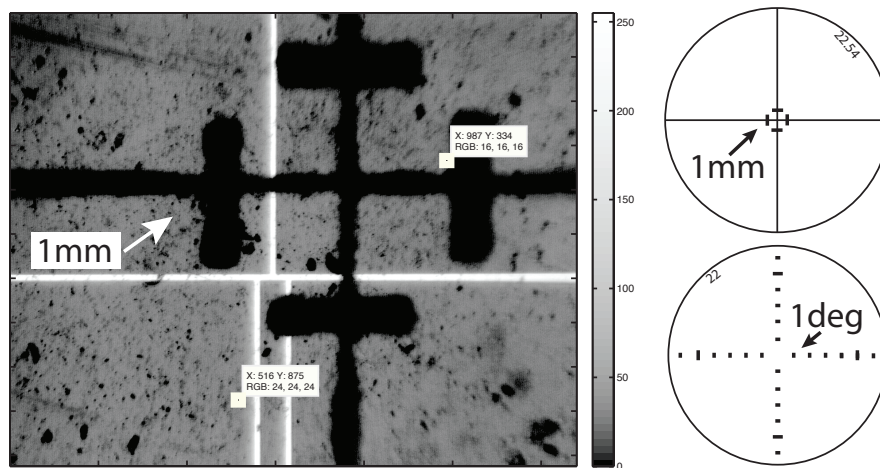
Figure 5.3: Fixation target defining $1°$ off-axis in the eye defined from experimental measurement of optical magnification with calibrated reticles in artifical retinal plane.

The primary source for the illumination is a light-emitting diode (LED Luxeon V star, Philips, USA) emitting in the green at 540nm±50nm. The LED ring system was assembled with 6 Luxeon Rebel LEDs. LED light is by nature incoherent and very divergent, so the illumination on the retina should be free of speckle, contrarily to the probing beam. Given the retinal scattering, the directionality of the illumination is not very critical given the system will only recover the light scattered in the direction of the optics.

The angular extent of the illumination on the retina needs to be defined so as to cover fully the imaged field. As this field is quite extended in our system the safety limits are decreased but this means more light into the eye is required to get an image, thus to avoid any damage to the cornea or to the retina, short exposure times are neces-

sary. The LED activation and the camera acquisition are triggered using an electronics board 8051 with software written to control the illumination power and flash duration. When the acquisition is not triggered with the illumination the camera acquires the image with a light level averaged over time and thus presents an overall lower intensity. Figure 5.4 shows the in-house heatsink built to prevent the burnout of the LED junction in continuous operation, that is to improve the LED efficiency and lifetime. The mask used to block the central part of the illumination was also made at the university.
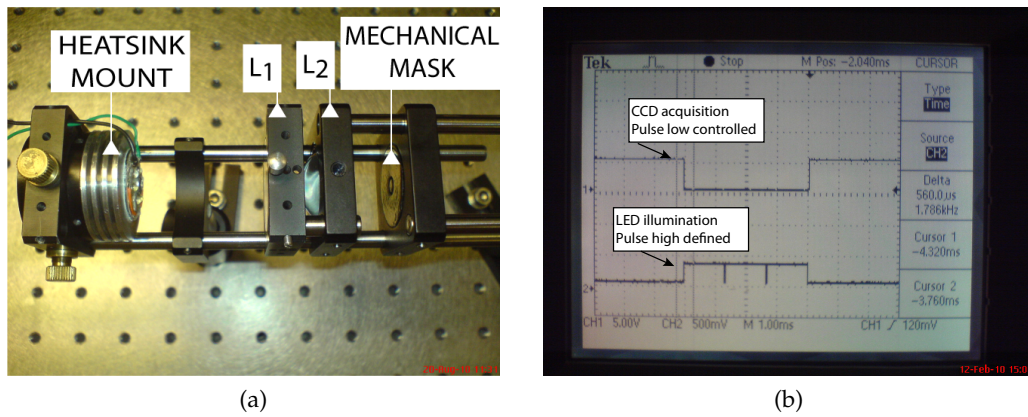
Figure 5.4: a. Condensed version of the 6-LED illumination system, with relay optics L_1, L_2 and mask. b. Oscilloscope signals of single-source emission triggered with CCD camera acquisition for a 4ms flash and image exposure.

From the average power P_{avg} measured at the corneal plane and the time of the pulse Δ_t the pulse energy E illuminating the retina is calculated by :

$$E_{pulse} = \Delta_t \times P_{peak} \tag{5.4}$$

The illumination power E_{pulse} in Equation 5.4 was designed so that its power at the eye was at least $10\times$ below the levels of Maximum Permissible Exposure (MPE) safety levels defined by the EU Standard 60925-1:2007. Those calculations are presented in Appendix B.

A calibration of the imaging system light collection efficiency was performed with a paper target in the artificial eye retinal plane illuminated by the light source. A test eye made of rubber was used with the maximal average power, which is equivalent to the flash intensity. In such an object adaptive optics is required for deblurring the initial high-resolution image. The rubber eye rear side structure is made of granulated

structures which appear in the retinal image.

5.1.3 Experimental set up

Calibration of the image resolution and retinal imaging with adaptive optics has been performed with the system presented in Figure 5.5. It is essentially identical to the system described in Chapter 3 and Chapter 4, except that the probe beam system has been implemented out of the Badal optometer. The probe beam diameter at the eye was magnified from 0.9 mm at the aspheric collimator output to 1.05 mm at the pupil plane of the eye. The 635 nm source of 3 μW power at the eye was replaced by an infrared diode laser (Thorlabs S1FC780) of 10 μW power at the eye. Pre-correction of the subject defocus was in turn impossible with this system. Calibration of the image resolution was performed with the single-source system based on a Luxeon V Star (Philips Lumileds, USA) flashing synchronously with the image acquisition. Retinal imaging was performed with the 6-source system based on Luxeon Rebel diodes (Philips Lumileds, USA) continuously illuminated.

5.2 Resolution targets imaged by the system

In the system considered here, the high magnification of the retina in the first conjugate retinal plane was also coupled with a good light efficiency provided by the first lens small focal length. However the long optical path of the relay from the first conjugate retinal plane to the science camera introduced some unwanted light from the computer monitor or the desktop lamp. Isolation of the science camera optics using black absorbing cardboard reduced noticeably this background signal. A large amount of losses were due to the numerous optical elements and in particular due to the beamsplitters separating the different system parts. To optimise the light coupling to the science camera a dichroic beamsplitter (CVI Melles Griot Long Wave Pass Unpolarised, 99 % reflective for 532 nm and 80 % transmittive for 633 nm) was placed after the deformable mirror.

As all the lenses of the system were achromats, the optical design with the model eye presented almost no difference in the focal plane position of the red wavelength and of the green wavelength. This problem was different when observing the eye due to the longitudinal and transverse chromatic aberrations [5,123]. The aberration pattern corrected by the deformable mirror at the conjugate pupil plane was assumed to be

Figure 5.5: Schematic of optical bench with probe beam out of Badal stage labeled (2) and pupil monitoring path (2) were used for calibration of imaging resolution and retinal imaging. Light-gray probe beam (1) and pupil monitoring (1) represent the optics used in the aberration measurement of Chapter 4.

117

scaled with the wavelength under the assumption that its correction was performed by defocusing the imaging lens towards the pupil plane [6].

Most of the retinal images were acquired in the green (530 nm), using the LED illumination system. Calibration of the image resolution was performed using either microscope reticles (Meiji, Japan), either USAF resolution targets on glass media (Edmund Optics, USA), as in Figure 5.6. All these systems showed a resolution conforming to the theoretical expectations, but highlighted the effect of the illumination power, and of the camera gain, offset, binning, exposure and image bit depth on the image quality. The illumination provided by the single LED-system was the most often used in these tests. A few images however were acquired using the flash-triggered system given the mechanical evolutions of the system.
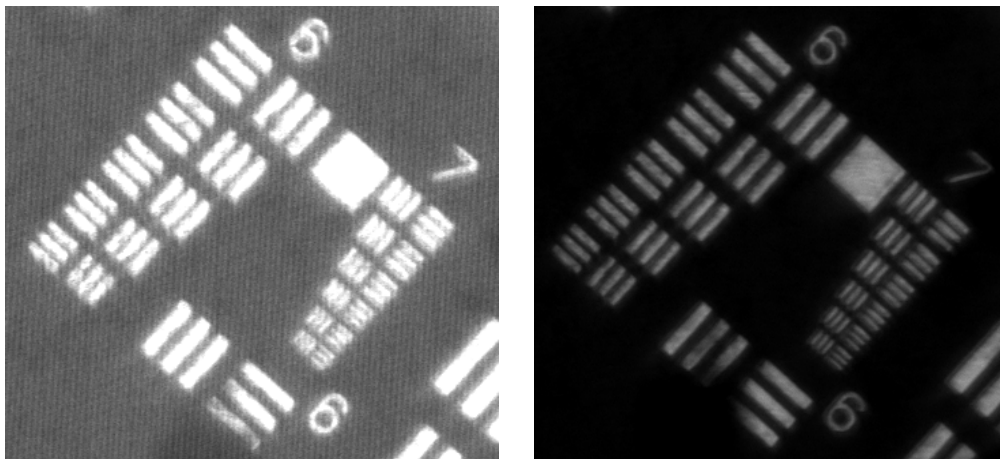
Figure 5.6: US Air Force resolution target on glass substrate imaged at highest resolution setting with flashing system at 2ms, 8-bit image, highest gain (left) and 10ms, 16-bit image, low-gain (right).

5.2.1 USAF target

The imaging of the last bar group of the USAF resolution target (228 c/mm) behind an f = 16 mm lens (6mm aperture) with the mirror correcting for the aberrations of the system confirmed the imaging designed for our system was appropriate as seen in Figure 5.6. A complete study of the system's static MTF as measured from this object is possible.

5.2.2 Microscope reticle

Figure 5.7 illustrates the resolution loss with the camera binning using a microscope reticle placed behind a 16 mm focal length lens. The reticle was composed of 100 bars engraved on a glass slide. Each reticle bar was of 2 μm width and the spacing between each bar of 10 μm. Every 5 bars a longer bar marked a 50 μm spacing. The total reticle length was 10 mm.
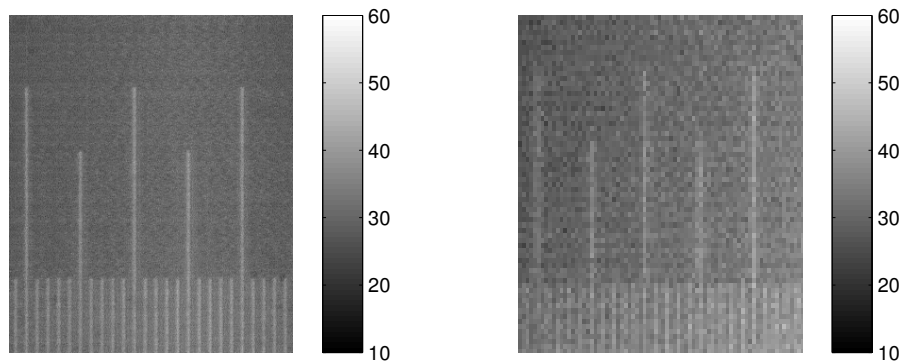
Figure 5.7: Microscope reticle image in the highest camera resolution B1 at 100ms camera exposure (a) and lowest camera resolution B4 at 10 ms camera exposure (b). The loss of resolution resulting in the camera binning is visible in the definition of the single micrometric spacing bars. The deformable mirror corrects for the aberrations of the system.

Using an f′ = 16 mm lens of good optical quality (Linos) but relatively small aperture (6 mm diameter) some field distortion can be expected at the edges of the image. The resolution of such an artificial eye is similar as the one calculated for an equivalent eye in air. The effect of the camera binning on the resolution is highlighted in Figure 5.7. The 10 μm spacing between the reticle bars was clearly visible for the highest image resolution at 100 ms exposure but disappeared with the binning at 10 ms image exposure. In this configuration the change in exposure from 100 ms to 10 ms was meant to avoid the saturation resulting from the camera pixels averaging. To balance intensity increase obtained by the formation of a pixel from a 4x4 pixels area, the exposure after binning should be calculated from the irradiance received on the camera chip. Gain and light level at the camera must remain constant.

Adjustment of the figure scale in the second image of Figure 5.7 is performed so as to display both images using a similar size. The camera exposure was experimentally adjusted so as to obtain a similar gray levels distribution as in the 100 ms exposure image. Both images are presented on a similar colorscale. The loss in resolution results in a blurred image of the reticles bars after the contrast decrease between the

reticle bars and the background illumination is observed between two reticle bars.

A typical problem encountered by our system with glass and metallic supports is that the image plane is much more reflective than the human eye, thus the experimental parameters used during the calibration of the image quality need adjustment in the eye. The deposited substrate in the case of the USAF target is also more reflective than an engraved pattern such as the reticles bars. Over the image field we can also see a non-uniform illumination distribution in those targets.

5.2.3   Rubber eye

The rubber eyeballs used in this demonstration are made of a soft plastic membrane containing a transparent liquid meant to model the vitreous of the eye (n=1.44, from the manufacturer's specifications). The image is acquired from the front of the eyeball through a smooth plastic type that forms an artificial cornea and eye pupil. The light backscattered by the plastic eyeball shows a network of artificial blood vessels converging towards an equivalent artificial optic disk. The curvature and semitransparent nature of the artificial eyeball makes this object interesting for calibration of the imaging system response to an absorbing and non-planar surface presenting in-depth internal structures in a media of different refractive index than air.

A piece of white paper card placed at the back of the artificial retina is used to increase the light return in the system. The result for a constant image field with and without the reflector is presented in Figure 5.8 for a constant illumination level, camera exposure and camera resolution. A sharp contrast improvement between the artificial blood vessel network and the background retina results from the white paper implementation. The image acquisition range is filled in the second configuration which means the white paper card replaces the choroid in the human eye. The static nature of the object allows long exposures to be used without any blurring due to the eye motion. The adaptive optics performance is also left free of constraints of speed or dynamics. The initial 1.2 μm wavefront rms measured in open loop for the ocular aberration of the rubber eye is corrected down to 0.05 μm without the additional reflective paper and down to 0.015 μm with the additional reflective paper as presented in Figure 5.9. The optical quality after closed loop is better when more light is returned to the sensor. This seems to validate that for a static element formed by a dense media, the correction of the ocular aberration is realized down to very low

values of rms error, improving consequently the distinction of the artificial retinal features.
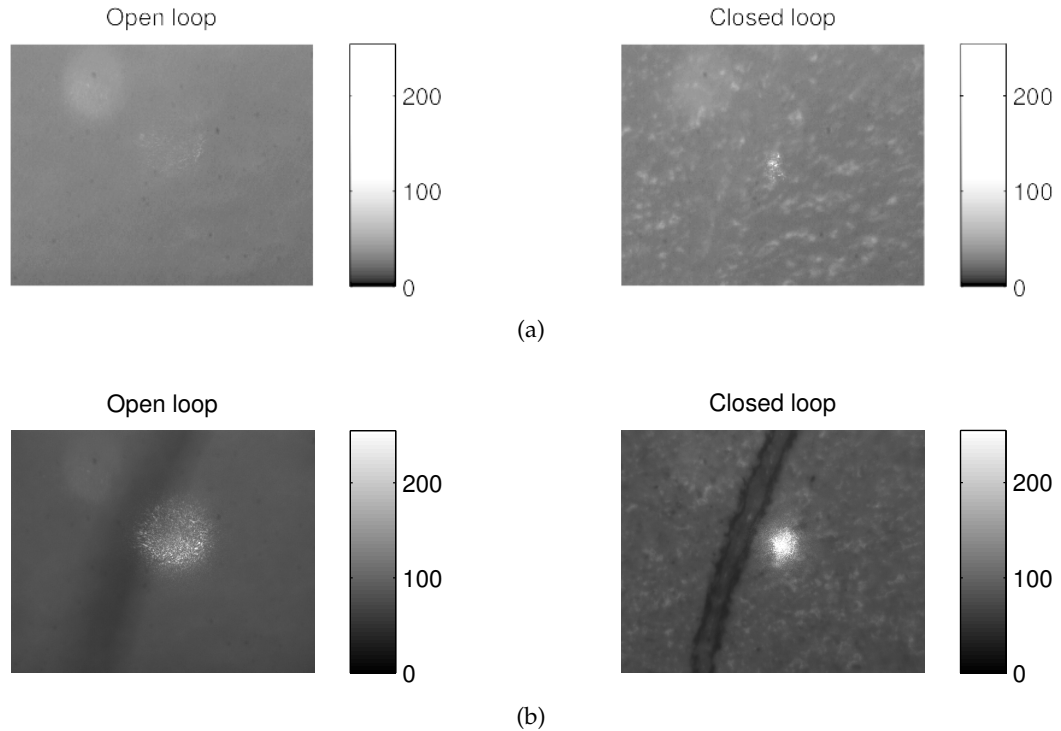
Figure 5.8: Highest resolution image at 50ms before and after adaptive optics for the rubber eye, without (a) and with (b) paper piece showing improvement of the light efficiency. The double pass point spread function apparent widening is related to the paper, showing the difficulty to quantify its effective extent from an experimental signal-to noise measurement.

The improvement in the retinal image quality with the change in the sensor dynamic range and / or pupil sampling can be evaluated with the rubber eye. The strength of the rubber eye 'ocular' aberration was indeed making it an appropriate test object for the highlight of the sensor saturation in a small dynamic range. However the result of this study was that the adaptive optics performance was about constant with the dynamic range, as shown in Figure 5.10.

The first row of Figure 5.10 shows the adaptive optics image obtained with the highest pupil resolution setting in the correction, while the second row shows the adaptive optics image obtained with the smallest pupil sampling at the sensor. In this configuration for our system it seemed as neither the change in pupil sampling nor in dynamic range was impacting on the retinal image quality after adaptive optics. In particular towards the change in dynamic range this means the increase in the

(a) RMS without reflecting paper

(b) RMS with reflecting paper
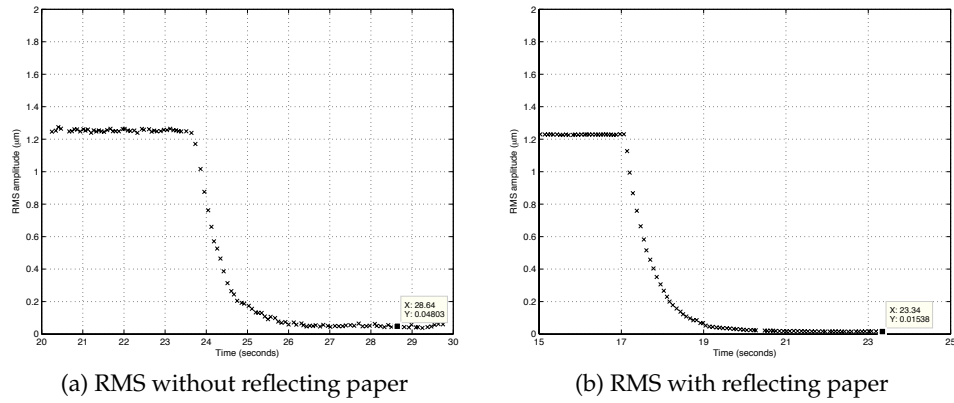
Figure 5.9: RMS timetrace for the rubber eye without and with the static reflector paper placed behind the eye. More signal is beneficial to the closed loop as presented in the case that has the reflector. Modulation $21\lambda/D$, 20modes used in the correction, 7 pupil samples /actuator at the sensor
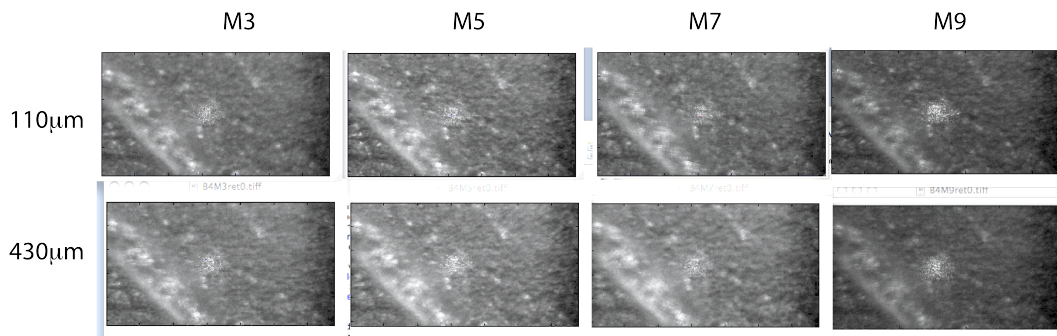
Figure 5.10: An increasing dynamic range (M3, M5, M7, M9 from left to right) and two settings of pupil sampling (110μm/sample, top row and 430μm/sample, lower row) after adaptive optics in a plastic eye at 50ms camera exposure. The lack of visual variation in the definition of the background rugosities means independence towards the sensor parameters for this aberration.

122

rotation amplitude at the pyramid doesn't lead to a sensible defocusing of the retinal image that could be related to the finite inclination of the pyramid facet. This means that the position of the retinal plane imaged would not be dependent of the modulation amplitude. The variation in the image overall gray level is related to the asynchronous operation between the camera acquisition and the illumination system.

After the adaptive optics is started, axial movement of the science camera adapts the plane of conjugation to bring the camera focus to a different depth in the artificial retina. Based on a visual assessment of the 'best focus' for a chosen structure of the image the science camera displacement indeed retrieved a sensation of in-depth imaging over the range of travel. These results are presented in Figure 5.11 for the transition through the range of the electronic stage (25 mm) which is equivalent to 0.75 D dioptres defocus at 635 nm (or to a 100 μm through focus in the retina of an emmetropic eye). The lack of visual change in image quality with the modulation amplitude or the pupil sampling was confirmed in these data. The evolution in focus is mainly visible from the plastic blood vessel appearance and from the loss of the details in the retina background, as the probe beam narrow size at the pupil provides a very long depth of focus for this beam.

In this configuration we also see the light losses related to the transparency of the rubber structure, which could be solved by positioning a white paper behind the artificial retina such as in Figure 5.8, or by using a flash-based illumination scheme. The average darkness of the scene due to the absorption was however not considered as problematic as the image contrast was rather sufficient to distinguish the rubber features for an average power of illumination ranging 50 μW and only a 40 % light efficiency out of the object. The in-depth acquisition stated that the through-focus was operational by axial displacement of the camera towards the imaging lens but was of very small effect on the image details.

The sizing of the retinal features imaged was identified by implementing a fixed-size reticle behind the rubber eye instead of the paper card, of the same type as presented in Figure 5.3 and presented in Figure 5.12. Provided the thickness of the artificial retina was not modifying the magnification by the change in refractive indexes. The global magnification from the rubber eye retina to the imaging camera acquisition plane could be calculated from the manufacturers' specifications for the reticle.

The rubber eye thus proved a convenient tool for the calibration of the adaptive optics
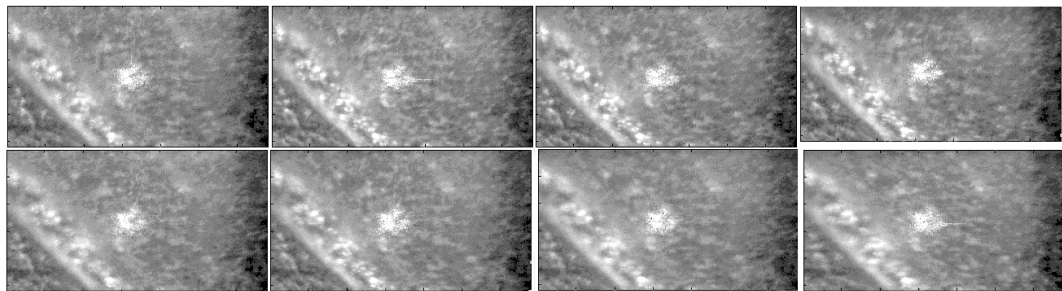
(a)
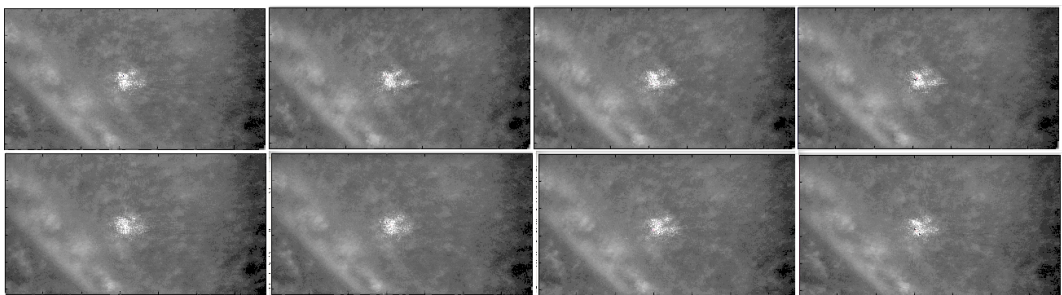
(b)

Figure 5.11: Axial translation of the science camera for the rubber eye retina. All images are 230×184arcmin in the rubber eye, at 50ms exposure image and highest image resolution. Sensor settings present an increasing dynamic range (M3, M5, M7, M9 from left to right) and two settings of pupil sampling (110μm/sample, top row and 430μm/sample, lower row) after adaptive optics. From Figure 5.10 in which the retina speckles are in focus the translation highlights progressively the blood vessel structure in (a) then the focus is lost (b). The probe beam constant shape relates to its small diameter at the pupil of the eye and consequently lengthened depth of focus.
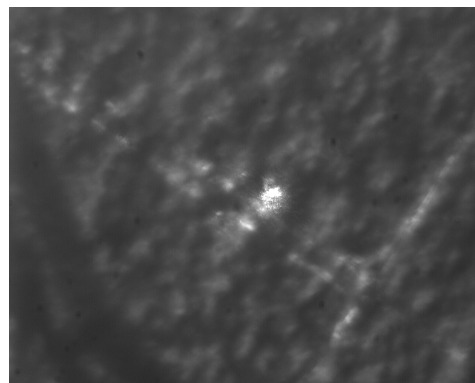
Figure 5.12: 100ms and highest imaging camera resolution acquisition of the reticle of Figure 5.3 placed behind the rubber eye retina after correction with adaptive optics.

124

efficiency in a static configuration and to obtain an overview of the retinal image quality improve resulting from the aberration correction.

5.3 Retinal imaging with adaptive optics in a real eye

In the procedure for imaging the eye with adaptive optics the initial position of the retinal camera was the one for which the calibration fibre point spread function was best imaged. Given the chromatic aberration of the eye, even after adaptive optics an axial displacement of the camera should be required between the plane of observation for the ocular point spread function and the plane of observation of the retinal cells. This displacement is equivalent to the application of a defocus in the image plane, and has been quantified in Section 3.3.3.3 to be correctable by displacement of the electronics translation stage [5].

In eyes with a good optical quality the adaptive optics performance is not obvious but still the signal to noise ratio improvement is observed. In more aberrated eyes the correction is obvious from the point of view of the observation of the point spread function size before and after adaptive optics but overexposure of the camera image rendered a saturated point spread function in the form of a white disk as presented in Figure 5.16.

Retinal imaging in the eye with the first illumination system was performed with adaptive optics but the source low illumination power resulted in a long exposure image at the camera. Any possible observation of cellular structures was thus blurred by the eye motion. Second, the resolution of this system in short exposures was measured not to be sufficient for resolving the retinal cells.

The system used for acquisition of the results presented in the following was described in Figure 5.5, Section 4.2.2. A change in the first beamsplitter after the eye resulted in an increase in light efficiency. The maximal power into the eye was reached with the single-LED illumination system at 130 μW average power (530 nm) measured over a 10 mm-diameter circular sensor, which was under the safety limits for the eye. Still, given the low light efficiency of the system from the eye to the camera pixel, averaging, high camera gains and 8-bit image acquisition were required, which resulted in signal artifacts in the form of diagonal fringes in the image. Basic image

post-processing operations were applied to these images in the form of digital filtering in order to extract some information on the retina structure.

Experimentally the effect of the adaptive optics on the double pass point spread function improvement was not very visible for the subjects which presented a refractive error below ± 0.25 D dioptre. The subjects studied in the following are thus separated into 2 groups which are noted "good eyes" for the eyes mentioned beforehand and "very aberrated" for the eyes that had a refractive error above 1 D dioptres and which were partially corrected with the Badal stage. In an absolute sense the refractive error in these eyes were below (-3) D diopters thus the system was tested only for low myopia subjects.

5.3.1   Retinal imaging of eyes with refractive error <0.25D

In this case the mirror shape correcting for the aberrations of the system only (that is the voltages set configuration 'flat') retrieved an image of the choroidal blood vessels without requiring dynamic correction.

For these subjects the retinal image with or without adaptive optics is not very different once the aberrations of the system are corrected. For subjects with a good fixation images acquired at 20ms exposure retrieved a correct identification of choroidal blood vessels. The lack of synchronization between the acquisition and the illumination systems resulted in the need for using 20 ms, 50 ms, 100 ms and 200 ms exposure times, which are long exposures for the eye. Binning of the camera chip was necessary to keep the light levels safe in the eye, which increased the size of a pixel at the retina but the light levels were still too low to reduce the exposure time of the image.

The typical acquisition procedure started with the imaging of the double pass ocular point spread function before and after adaptive optics correction. The power of the probe beam laser (780 nm) was 10 μW and the average power of the illumination (535 nm) was 26 μW over a 5degree retinal area.

For the example presented in Figure 5.13, the ocular PSF was not extremely different before and after adaptive optics thus again the correction was mainly effective on the tip and tilt. Infrared laser at 780 nm was used here instead of red light as more convenient for the viewing by the subject. The difference in wavelength between the

(a)	(b)
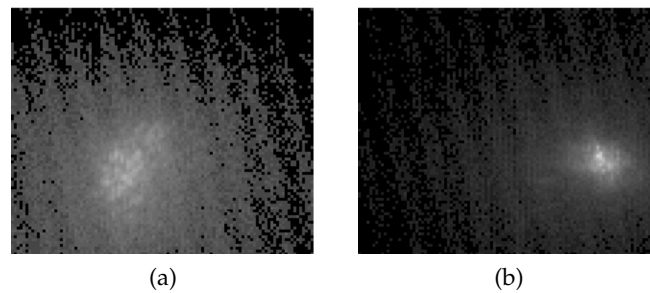
Figure 5.13: The adaptive optics corrected for the tip and tilt of the beam towards the reference axis of the system. Initial point spread function (a) without adaptive optics and after adaptive optics (b) at 50ms exposure.

infrared and the red laser for the same entrance pupil in the eye were estimated as small, and was observed not to destabilise the closed loop.

(a) 3deg up fixation	(b) 2.5deg down fixation	(c) 5deg down fixation
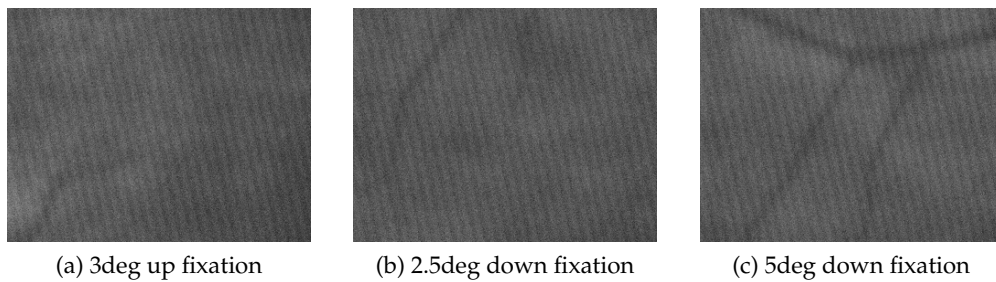
Figure 5.14: 100ms, low-resolution retinal image (continuous 535 nm illumination at 26 μW average power) for an eye with fixation change from $(-5)^\circ$ to $(+3)^\circ$. Field is $4^\circ \times 3.6^\circ$ in the eye. Fringes are signal artifacts due to the high camera gain.

The low light coupling efficiency of the system did not allow the acquisition of high-resolution images and required high camera gains inducing signal artifacts in the form of fringes across the field, as in Figure 5.14. The fixation marks did not appear in those images possibly due to a shift between the image plane and their focusing plane. In another beamsplitter configuration using a lower light efficiency but a higher power at the eye the fixation crosses appeared and the image signal was high enough for lower light exposures to be used. A 16 bit image depth was also used that removed the fringes artifacts but introduced gaussian noise in the image. The maximal power at the eye was however not sufficient to obtain a high-resolution image at low-exposure. Either high-resolution images were obtained at 100 ms typical exposure, either low-resolution images were obtained at 10 ms to 50 ms exposure. The results obtained for such parameters are presented in Figure 5.15.

| (a) 10ms | (b) 50ms | (c) 100ms |
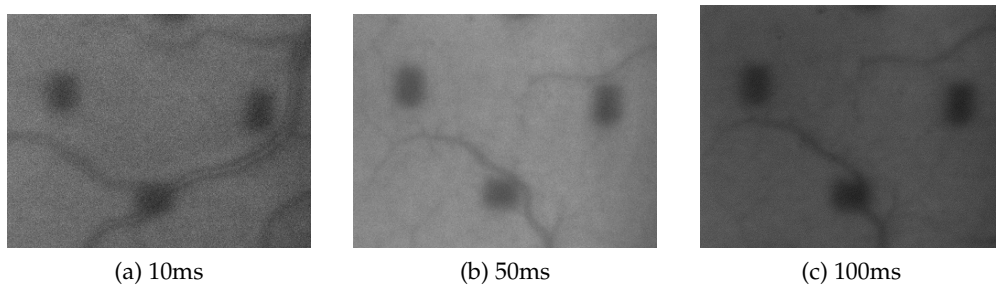
Figure 5.15: Low light levels retrieve either low-resolution images (a) at 10ms exposure or at 50ms exposure (b), either high-resolution images at 100ms exposure deteriorated by the gaussian noise (c). Field is $4° \times 3.6°$ in the eye.

Acquiring such retinal images quantify the system response to the continuous illumination and stress the requirement of using a flashed source. Reduction in the background light from the lab room and quantification of the increase in the illumination power required to reach a good signal to noise ratio represent issues that have to be solved. For example, to obtain a similar signal to noise ratio as Figure 5.15 (b) in a high-resolution image acquired at 1 ms a $400\times$ increase factor in power would be required. Such a power level in the eye (54 mW) would be harmful for the eye thus cannot be implemented. The alternative is to increase the light efficiency from the eye to the imaging camera and to trigger a high-power illumination with the acquisition for a short time after setup of the field to image at low power.

5.3.2 Retinal imaging of eyes with refractive error >0.25D

Eyes with a refractive error of more than 1 D diopter were corrected by the Mirao large stroke until 3 D diopters of refractive error, for which the defocus correction was performed first with the Badal stage axial translation, then by the adaptive optics. Myopic eyes of this amplitude of refractive error were more frequent than hyperopic eyes in the population we tested. The correction in those eyes was unfortunately applied using the lowest pupil spatial sampling and in turn at the fastest software acquisition (40 Hz). This resulted into closed loop instabilities related to the mirror commands oscillation effects.

Without filtering of the red (635 nm) power at the science camera the long exposures retrieved a saturated image of the probe beam and the auto-leveling of the camera grayscale onto this maximal level. The effect of the adaptive optics was thus visible

from the retinal structures appearing in the background. The Badal correction could not be observed from the point spread function shape correction in this configuration. As illustrated in Figure 5.16 the final correction shows the point spread function final correction and the fixation marks to appear in the image.

| (a) | (b) | (c) |
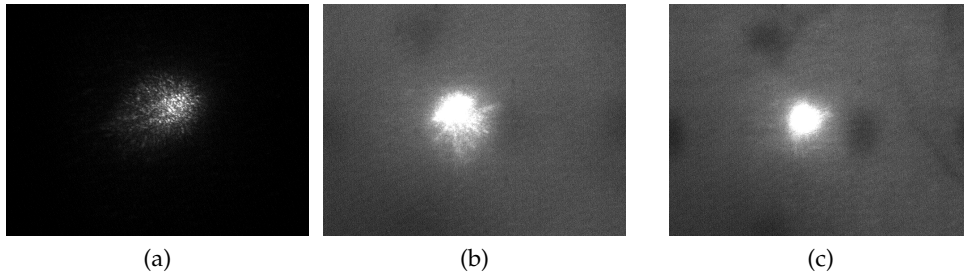
Figure 5.16: Initial point spread function before defocus correction (a). The ocular aberration with defocus corrected still presents aberrations that deteriorate the image (b) while if the adaptive optics is started the retinal structures appear (c). 200ms exposure, $4° \times 3.6°$ in the eye.

After the adaptive optics correction was launched in those eyes retinal blood vessels become visible. Through the noise the retinal image wide field show structures such as the fovea and the capillaries near the avascular zone if the eye was looking at the center of the field. In Figure 5.17, the use of a color filter to remove the adaptive optics beam from the wide field retinal image highlighted a bright ring surrounded by a dark patch of intensity located near the right-hand side of the 1 degree nasal fixation target mark. This signal moving in the image sequences with the fixation followed by the user let us think it could correspond to the signal of the fovea in corrected image.

The adaptive optics correction achieved in the eyes that require constant glass wearing presents an increased experimental difficulty given the strength of the aberration can only be compensated by a very fast application of the correction to acquire a proper retinal sequence. High gain values are thus required, which limits the acquisition to very short times due to the consequent impact on the adaptive optics loop stability.

5.4   Conclusions

This section has been presenting the design of the retinal imaging based on a basic calculation of the transmission of the object high spatial frequencies to the acquisition system.

(a)   (b)
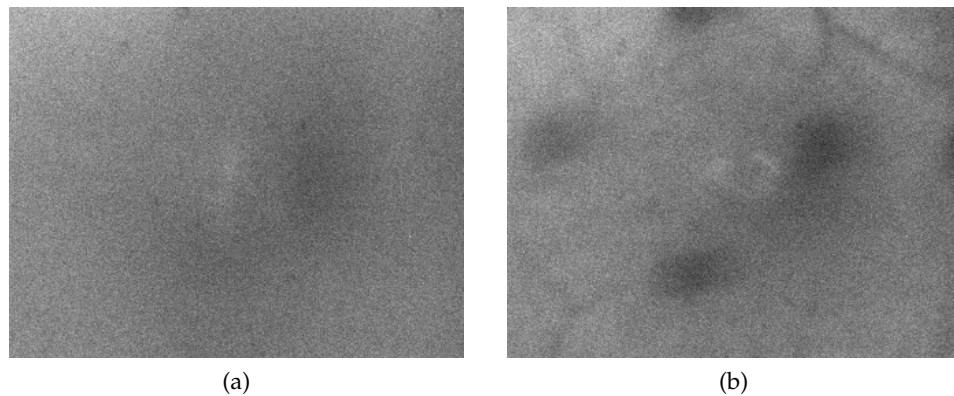
Figure 5.17: When the mirror is correcting for the system aberration only the retina does not appear (a) while if the adaptive optics is started the retinal structures appear (b). 200ms exposure, $4° \times 3.6°$ in the eye fixating at the $1°$ mark on the left side.

Experimental implementation of the illumination was described and experimental testing of the image resolution using static objects in artificial eyes was presented with and without adaptive optics. On a static object presenting an in-depth retinal structure, the adaptive optics led to an improved image resolution, independently of the wavefront sensor pupil sampling ('B' for the Binning parameter) and of the modulation ('M' for the Modulation parameter).

In the human eye in-vivo, for refraction amplitudes of < 0.25 D the adaptive optics could not be clearly distinguished from the cancellation of the aberration of the optical system. The retinal image before and after the ocular aberrations were corrected did not show a signal-to noise improve. For higher amplitudes of refraction, (remaining below 3 D) the adaptive optics effect was clearer, despite the low quality of the final image.

An overall need for improving the light collection efficiency of the system, by the use of a flashed source at the retina synchronized with the image acquisition has been observed. Imaging of the retina asking the subject to fixate at off-axis angles of higher amplitude than $1°$ did not show 'classical' photoreceptors signals despite the cells size expected at those retinal subtenses presence. Unexplained very weak intensity blobs were present in some retinal images (Figure 5.14, left and Figure 5.15, center).

Chapter 6

Conclusion

6.1 General conclusions

In this work a pyramid sensor was implemented in an adaptive optics system dedicated to the correction of ocular aberrations for use in a retinal imaging system for the human eye. The lack of "nice" images of the retinal cells [meaning the cone photoreceptors response to light in an healthy retina] as a result of this work is believed to be mainly related to the lack of power in the illumination of the eye, which resulted in exposure times which were too large to overcome the motion of the eye.

Many assumptions were made in the design of the optical system, whose combined errors might render impossible the imaging of the eye. The first was that a low-coherence source would reduce the speckle observed in the retinal image point spread function, for the part of the probe beam laser not used by the wavefront sensor. The second was that a geometrical optics design would suffice to the description of the propagation, and the third assumption was that the wavefront sensor signal was based on the part of the probe beam light backreflected from the retina in the direction of the sensor. We discuss in the following these assumptions and their relative influences.

The range of the sensor was designed so as to provide the largest possible dynamic range within the limits defined by the mechanical range of the steering mirror and by the optics aperture. As a result, the maximal wavefront aberration detected should

have allowed the measurement of keratoconic eyes [124], although no data were specifically collected for this purpose. The maximal correction amplitude estimated from the numerical simulations was experimentally verified using ophthalmic lenses and phase plates. In the eye, it was observed for 3 eyes of spherical defocus amplitude above 1.5 D diopter that the adaptive optics correction by the mirror only was not sufficient. Complementary correction by the Badal optometer was then necessary. The question of the adaptive optics reference arose after an experimental set acquired in a low-aberrated eye presented a worse image quality with adaptive optics than without.

The effect of the scattering by the retinal cells on the probe beam was visible by a widening of the probe beam diameter image compared to its image after reflection on a glass media or on a piece of paper. The use of a narrow probe beam diameter for the eye was thought to minimize the propagation of unwanted backreflections from the cornea into the system. The improve in the wavefront sensor light collection efficiency provided by the spatial localization of the forward point spread function using a wide-diameter probe beam [125] was expected to be compensated by the insensitivity of a narrow probe beam to the ocular aberration [126,127]. In this view the pre-correction of the spherical defocus by propagation through the Badal optometer is not as powerful as it is on a wide diameter beam, and the parallel input of the probe beam into the eye without pre-correction was then seen as equivalently efficient for the wavefront sensing.

Assuming independence of the wavefront sensor light capture direction towards the incoming direction of the wavefront sensor probe beam, the wavefront sensor light was not only issued from the specular reflection at the outer nuclear segment of the photoreceptors but from many retinal structure emitting in its collection cone. The probe beam light that was not backscattered by the retina was lost for the sensing but did not contribute to the closed loop wither, thus any type of quasi-monochromatic source could have been used as long as the sensor detection plane was conjugated with the pupil plane of the eye and with the correction plane formed by the deformable mirror. Even though this means a light loss for the wavefront sensor, the high sensitivity of the sensing system still coped with very low light-levels. The closed loop divergent regimes could never be attributed to the lack of light for the sensor.

At 50ms camera exposure for a static object such as a plastic-made eye, the narrowing of the double-pass point spread function with adaptive optics corresponded to an improvement in the retinal image definition. However, at 200 ms in the human eye in-vivo with a low-power (20μW average power) illumination, the benefit of the adaptive optics on the retinal image quality was not always obtained despite the reduction in the wavefront sensor probe beam narrowing. If hundreds of milliseconds exposures are common for wavefront sensing in the eye, the order of the millisecond is however required to outweigh the ocular microtremor effect in a fundus camera [15]. The illumination power and the optical system light collection efficiency in this system limited high resolution acquisition below 20ms exposure time. The data collection presented nevertheless a certain consistency in the retinal image definition for the wavelength used and the camera exposures considered after the change in the deformable mirror. The comparison can be established with the data obtained at the beginning of the thesis with 20μW average illumination power.

The adaptive optics correction seemed operational even when the sensor saturation was reached - which shows the control system robustness to high amounts of aberration. This however becomes a limit for the global understanding of the system as it means that the characterizarion of the aberration to correct by the sensor is not necessary to obtain a closed loop regime. As expected from the numerical simulations, the deformable mirror large stroke allowed full correction of a larger amplitude of ocular aberration. The reference signal importance was highlighted in this regard, as if the convergence to the 'flat' closed loop wavefront was defined by the user, the wavefront correction ability given by the large stroke mirror could not be the limit to obtain retinal images.

6.2   Recommendations for further work

Further work on this project would be first to increase the illumination power so as to reach retinal acquisition at exposure times below 5 ms in a flashed sequence. In the current configuration, high resolution cannot be achieved given this limit. It is imperative that the illumination be triggered to the acquisition in a flashed sequence, as high light levels continuously shone on the retina would be harmful for the eye. A great emphasis was put on getting the closed loop working with the pyramid sensor

and the high stroke deformable mirror. The sensor signal interpretation led to the idea that the sensor variable sensitivity to the aberration could not be observed due to the sensor noise. In this thesis it is possible that more attention should have been devoted to the design of a high-quality fundus camera to which would have been added an adaptive optics system afterwards applied to subjects imaging.

Second, it is generally accepted that the implementation of post processing techniques is required to increase the signal to noise ratio after the acquisition of an image sequence in the eye. Evaluation of the raw data contents to guide the signal processing steps are crucial for obtaining an image on which the clinician will assess the stage of the disease. An initial image that presents the photoreceptor signal only after image processing is susceptible to present signal artifacts related to the processing. As shown by the implementation of Fourier deconvolution by the wavefront sensor signal [13, 49], by pure signal processing [51, 128] dramatic improvements can be obtained in the image quality. In some cases, image recentering and averaging algorithms can still retrieve useful information on the retina after processing [129]. Algorithms implemented for astronomy have shown that information could be extracted from the long-exposure point spread function, but the turbulence statisics difference with the eye prevents their application in this domain.

Appendix A

Acquisition software

A.1 Acquisition and processing interfaces

The wavefront reconstruction code calibration for the wavefront aberration in the exit pupil was presented in Section 3.3.3. An upgrade in the operating systems was required so as to synchronise both acquistions. The initial driver of the Mirao52 deformable mirror and the adaptive optics code were written respectively in Labview 7 Express on a Dell Optiplex 260 (Windows XP) and in Labview 7.1 on a Dell Optiplex GX260 (Windows 2000). The initial acquisition software for the science camera was running onto a separate operating system (Windows 2000). The wavefront sensor and the science camera acquisitions now run in parallel on a single machine (Dell Optiplex GX745 using Windows XP Pro) using the dual input of the camera graphics card (1394 port) via separate fireware cables. Two programmes have been written in Labview 8.2, so as to separately control the adaptive optics acquisition parameters and the science acquisition parameters. We observed that the use of global variables to control, for example, the science camera exposure was impacting on the wavefront sensor camera exposure if this parameter was not defined explicitly. Similarly, the global variable controlling for the acquisition of the cameras ('Grab Abort' control, which cancels the transfer of the camera buffer to the computer, but keeps the camera recognized by the user software) once appropriately wired to each camera, could be used to disable temporarily the science acquisition or the wavefront

acquisition, thus increasing the other camera acquisition speed.

The two interfaces presented in Figure A.1 are experimental screenshots of the acquisition. Each software was displayed on a separate screen through a dual-display graphics card (ATI radeon HD 2400, Dell). This organization was more convenient than monitoring the full field of the science camera with the adaptive optics software hidden from the screen or minimized.

A.1.1   Science camera software

In the science software the camera gain, exposure, binning, and gray level offset can be adjusted. The translation stage mount control interface (Thorlabs, APT nanopositioning system Z625B) controls the distance between the camera and the imaging lens of the science path. In the triggered (flashing) mode, the flash duration is controlled by the round knob at the lower left of the interface. The flash power is controlled by the side bar on the right. The small image window on the upper left of the big image window displays the flashed image sequence that is saved. The big image window displays either the continuously acquired image (saved or not) or the image in the flashing acquisition but not saved. When saving the frames in the continuous acquisition mode the software transfers to the computer all the frames acquired by the camera while in the flashed mode a sequence of N frames is transferred to the computer.

The light levels in the flash image are generally higher than in the average image as the illumination is perfectly synchronized with the camera acquisition. This creates a problem for the initialization of the image acquisition parameters as indeed the Labview image display indicator grayscale is adjusted to the image graylevel distribution. For example in Figure A.1, the brightest pixel of the image is at the closed loop point spread function maxima. If the LED-illumination is active in that configuration, the retinal signal is mainly defined within the background, as the Labview image display indicator concatenates into an 8-bit grayscale the initial 16-bit image depth setting the maximum pixel at the level 255 and the camera offset value at the level 0. An histogram control can be implemented to insure the light levels in the continuous and in the flashed image are properly defined but is not used in this version of the software as it was observed to slow down the acquisition consequently. To enhance the retinal signal, the implementation of a green filter in the camera path is

the simplest solution, however at the risk of not finding the image plane, as the point spread function width cannot be used as a criterion of closed loop efficiency.

A.1.2   Adaptive optics software

The adaptive optics software displayed in the lower part of Figure A.1 contains the pupil signals from the wavefront sensor ccd after substraction of a background frame signal on the top row. The sensor signals after operation on the ccd pupils and the sum of the intensities of the 4 sub-pupils is displayed on the second row. The indicator on the right presents the deformable mirror commands. The common pupil mask defined from the thresholded subpupils and the thresholded camera frame is displayed on the lowest row. The indicator in the middle of the lowest row displays the wavefront Zernike decomposition. The 'xgrad' and 'ygrad' histogram indicators display the pupil signal distribution. The PWS mode indicates the type of processing of the wavefront sensing frame in the software. The calibration is performed in the 'Threshold' mode. At each software iteration the pupils are displayed on a mask calculated by zeroing the pixels under the threshold intensity value chosen (Threshold control) within the graylevel of the pupil. During experimental operation the 'Mask' mode defines a fixed pupil mask applied to the camera pupils.

The 'Display alignment' control activates / deactivates the update of these indicators at each acquired frame. The sensor signals ('CalcandDispGradient') control ensures the sensor signal is calculated over a common pupil mask area, the green indicator 'nbpart=ok' is in this case lit. The choose/save option saves in the calibration mode the pupils signal as 'reference' or 'Flat' signal (s_{ref}) and in operation mode with the 'Saves grad or Flat' saves the sensor maps along with the camera signal while the 'Save Sensing' control only saves the signals within the sensing mask.

If the control matrix calculation at each frame is required the 'Czonalcalc' is lit in green. The closed loop parameters of gain ('Gain') and Condition number ('CzonalNb') are the input parameters in the closed loop. If the control matrix is calculated while the closed loop is active the number of modes out of the correction after filtering with the condition number is indicated by 'N modes out'. At the beginning of the closed loop after the command matrix is initiated the 'Fast-op' control can be activated after the command matrix has been defined. If the closed loop is wanted to be applied in steps so as to for example stabilize the mirror operation one possibility is to activate the 'CLfreeze' control, which sends the last mirror voltages at the next
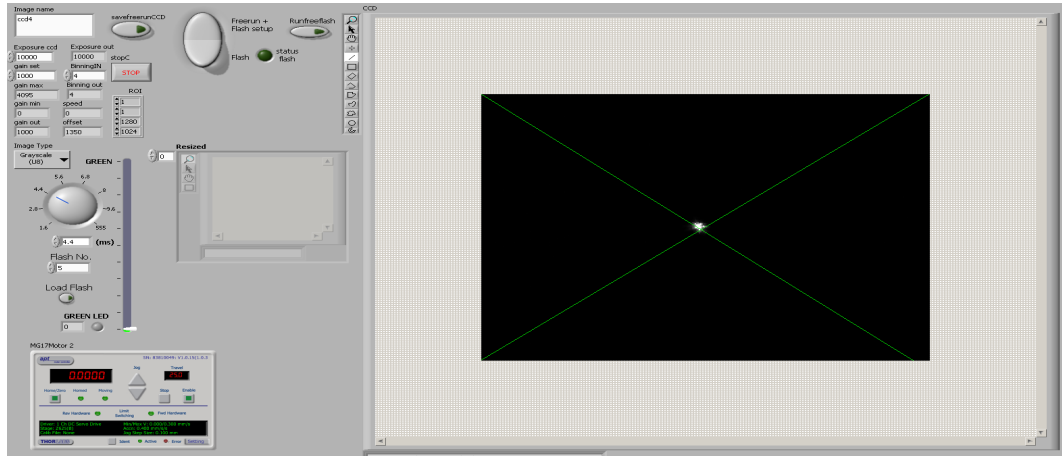
(a) Science software
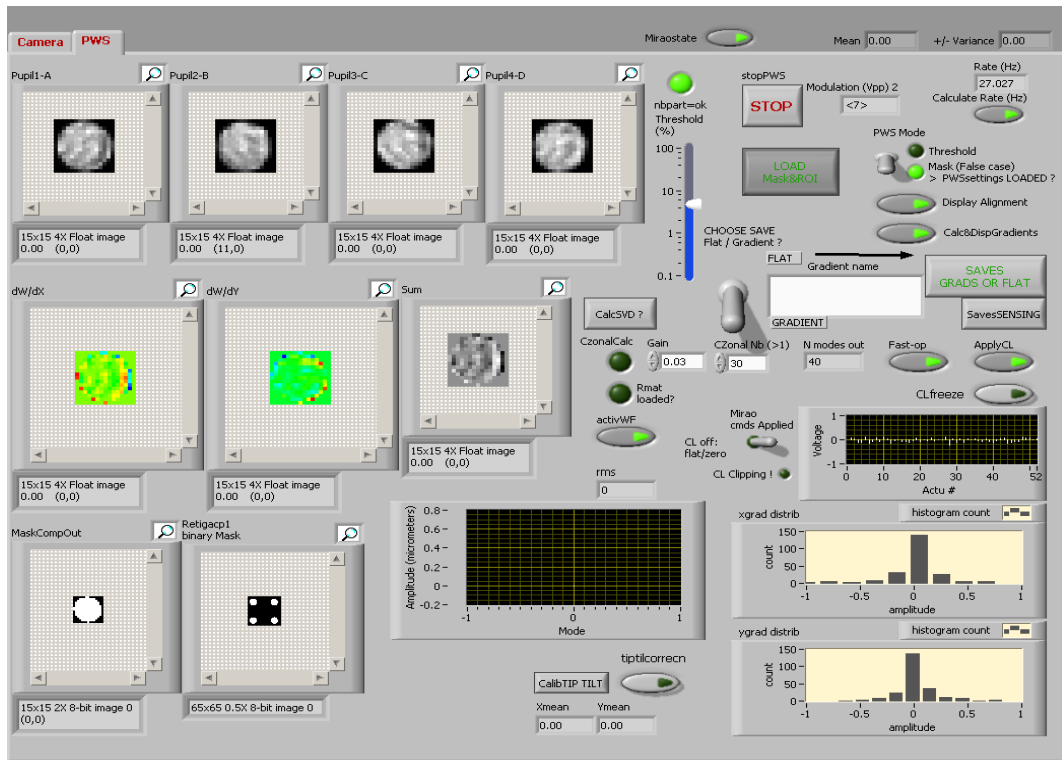
(b) Wavefront software

Figure A.1: Dual display for calibration of the sensor PSF (10 ms) centered on the image of the science camera software and corresponding pupils signal and gradients in the adaptive optics software

loop iteration thus stabilizing the mirror commands for a short time.

Before activating the Zernike live reconstruction ('activWF') the control parameters must be initialized 'Rmat loaded ?'. The tip and tilt of the initial wavefront are determined for each direction under activation of the 'calcTIP TILT' button which displays the associated values in the boxes 'Xmean' and 'Ymean'. The tiptilt correction is preferrably activated after the closed loop is stabilised. If the user wants to obtain convergence of the loop on another wavefront as the reference wavefront an additional control (not displayed here) subtracts the reference signal from the sensor signals at each loop iteration.

Control parameters such as the deformable mirror commands and the live Zernike decomposition of the measured wavefront can be seen on the centre and on the upper-right part of the interface. The same software is used for the calibration and for the live operation, which probably induces losses in the acquisition speed.

During the acquisition the two programmes are operated in parallel. In the closed loop control if the command matrix calculation is performed at each iteration of the loop the closed loop is slowed down. The respective binnings of the cameras and the definition of the region of interest for the wavefront sensing camera are the main parameters for the system speeds. For the optimal acquisition speed to be reached the science camera image depth must be of 8 bit, the optional display of the ccd pupils and gradients is cancelled. The optional Labview on-line Zernike reconstruction is cancelled and the sensor signal maps saving system is disabled. When all displays are updated and all the control parameters are saved the current system is indeed keeping in memory the whole sequence of : mirror commands, sensor signals within the pupil, sensor signals within the masks, and Zernike decomposition coefficients when active. Still, the code suffers from some slowdown, as for example the setup of the saving of the camera frames that necessitated the Labview code to create a new image file at each frame acquired. This was however more appropriate for long acquisition times than using the computer RAM memory which was progressively saturating when long sequences of sensor data were acquired, eventually slowing down the acquisition system.

All camera frames acquired in 8 bit or 16 bit were converted into a double precision value so as to run additive and multiplicative operations on the pixels intensities. In

open loop those operations were not very computationally intensive unless the live wavefront reconstruction routines were active, as based on a Matlab node inserted within the Labview code. In closed loop, the calculation of the control matrix was the longest operation if operated at each frame acquisition. This calculation was thus only initiated at the beginning of the adaptive optics then the same control matrix was loaded in the live sensor operation for a parameter set. The display of the sensor signals was also disabled and the closed loop stability was determined by observation of the point spread function at the science camera and of the mirror commands only.

We verified separately that the binning of the science camera increases linearly with the acquisition speed, and that the use of a 16 bit image depth divides it by almost a factor 2. The science camera integration time is another dependency, as the speed decreases with its increase, but not necessarily linearly over the exposures commonly used in this work (1.6 ms, 10 ms, 50 ms, 100 ms and 200 ms). Over the whole thesis the wavefront sensor camera parameters were constant at 10ms and 8 bit. Those parameters could have been changed but were fixed as providing a sufficient signal for the calibration and for the operation of the system from the start of the thesis.

A.1.3   Reconstruction interface for results analysis

All the data are saved over a set of modulations and the post-processing of the signals is displayed in the form of a movie as in Figure A.2. The exact time the science image is recorded and the exact time the sensor frame is acquired are noted during the data acquisition. In the post-processing of the data, the time stamp of the sensor and of the science are ordered in increasing order. Each point of the ordered timeline is identified to a time stamp of the science timeline or of the sensor timeline, the corresponding data are imported and displayed in a new movie frame. The wavefront sensor signal (k) or the science camera frame (ind) of the reconstruction interface thus correspond to data acquired at a short intervals of time.

The full science camera image is displayed in the top-right corner of the movie frame. A region of interest selected within the frame (typically near the center) is displayed in the top-middle image of the frame. In the upper-right window is displayed the wavefront rms at the time considered calculated from the decomposition into Zernike terms. The wavefront surface reconstructed from the Zernike decomposition is displayed on the left in the middle-row. The Zernike coefficients of the decomposition

are displayed in the central image of the middle row. The mirror commands are monitored in the middle-right window of the display. In the last row the sensor signals of the pixels within the pupil for the horizontal and vertical gradients are respectively displayed in blue and black. This allowed to monitor the saturation when the signal reached ± 1.
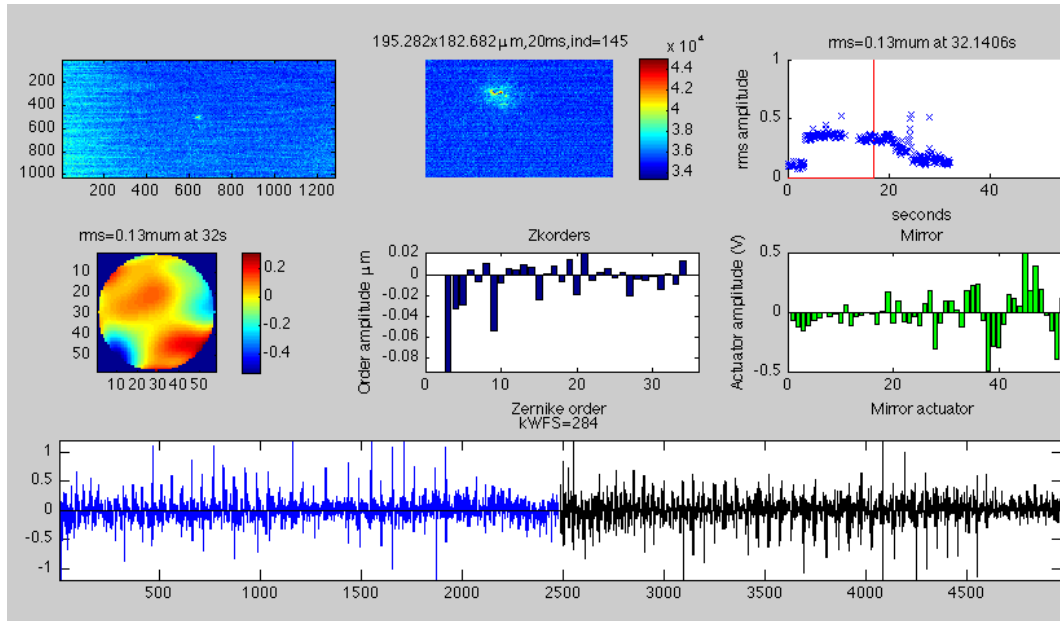
Figure A.2: Offline reconstruction movie interface, closed loop operation in the eye

A.2 Open loop acquisition speed from code parameters

The magnification of the wavefront slope and of the camera pixel to the pupil of the eye is calculated from geometrical optics in Table A.1. The wavefront sensor camera is conjugated to the pupil of the eye through the artificial pupil of the mirror, of constant size. The number of pixels across the pupil can be varied by the camera binning, that is when 1 pixel of the display (i.e. a "super-pixel") is the average of a 2×2, 3×3, or 4×4 pixels area on the camera chip. As fewer "super-pixels" describe the same pupil area, the camera binning means a loss of spatial resolution for the wavefront reconstruction. The advantage for the user is a gain in measurement speed as fewer pixels of the camera chip are read.

141

Table A.1: Pupil parameters with sampling

Binning	1	2	3	4
$N_{samples}$ across pupil diameter	55	27	18	14
N_{pixel} across 1 mirror actuator	6.87	3.37	2.25	1.75
Size of one pixel at the pupil of the eye	109 μm	218 μm	327 μm	436 μm

The average adaptive optics code frequency is thus only dependent on the sensor camera binning parameter as summarized in Table A.2. With 35Hz in the lowest pupil sampling (*a priori* fastest operation regime), the sensor speed is still very slow despite the fact that all parameters are optimised to reach the maximal efficiency. These values are nevertheless consistent with other adaptive optics systems for retinal imaging, and are more related to the processing and saving system than to the operating system or the coding.

Table A.2: Adaptive optics code average speed (Hz)

Binning	1	2	3	4
Average frequency (Hz)	14.8	26.5	31.2	37
Standard deviation (Hz)	1.4	2.1	4.3	1.1
Pixels across the pupil	55	27	18	14

Appendix B

Maximal permissible exposures

• The European standards reference document used for calculations is BS EN 60825-1:2007 [1].

• The American standards reference document used for calculations is ANSI Z136.1-2000 [2].

• The eye pupil is assumed to be of 7mm diameter, dilated with a drop of tropicamide 1% ophthalmic drug.

• The experiment timeframe is 1 hour (3.6×10^3s).

• All experiments are carried out with a dilated pupil and with prolonged exposures. Therefore it is necessary to apply the standards to the LED light considered as a laser emission, neglecting the 30nm spectrum spread around the central wavelength.
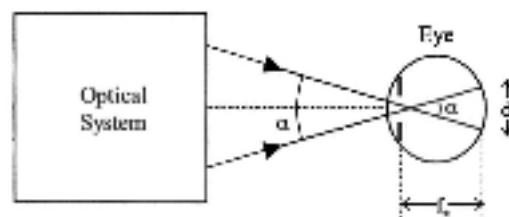
Figure B.1: Illustration of the Maxwellian illumination, from Delori [130].

B.1   Wavefront sensor probe beam

The laser source is a 635 nm - CW collimated gaussian beam of 1.55 mm diameter at the eye, as pictured in Figure B.2b. The retinal damage is thus in the thermal domain.

The angular subtense α of this beam is given considering the collimated input beam at the entrance of the eye is focused on the retina by the eye's optical elements (total focal length = 17 mm) in the form of an Airy spot whos radius sets the height of the angular subtense of the beam:

$\alpha = 2 * \text{atan}[(1.22 * 0.635 \times 10^{-6} * 17 \times 10^{-3} / 1.55 \times 10^{-3}) * 1/17 \times 10^{-3}]$

$\alpha = 2 * 0.49 \text{ mrad} = 0.99 \text{ mrad}$

$\alpha \simeq 1 \text{ mrad}$

The maximal beam power at the cornea is measured at 1.3 μW for the 1.55 mm diameter beam (of area 1.89×10^{-6} m^2).

Hence the maximal corneal irradiance for the experimental input beam is :

$1.3 \times 10^{-6} / [\pi * (1.55 \times 10^{-3})^2 / 4] = 0.7689 \times 10^{-3}$ W.m^{-2}

(a) Retinal flood illumination with annual shape in corneal plane

(b) Airy disk radius for angular subtense of AO beam
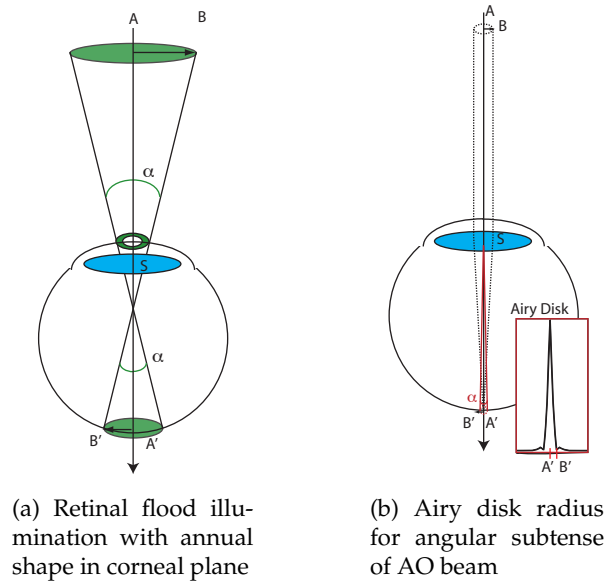
Figure B.2: Schematics for retinal irradiance in the wavefront sensor beacon and illumination

B.1.1   EU standard for AO beam

The Maximum Permissible Exposures (MPE) at the cornea given by the standard (Annex A, p.56 of [1]) is dependent on the parameter C_6 which is given by Table 10 of p.49, [1].

As $\alpha < \alpha_{min}$ = 1.5 mrad, and λ=635 nm,

Table 10 of p.49, [1] gives:

$$C_6=1.$$

Then the maximum permissible exposure for C_6=1 at the cornea is determined by Table A.1. p.57 of [1]. With the exposure time $10^3 < t = 3.6 \times 10^3$s $< 3 \times 10^4$

and 500 nm $< \lambda = 635$ nm < 700 nm

We thus have:

$$\text{MPE} = 10 \text{ W.m}^{-2}$$

The ratio between the MPE irradiance and the experimental beam irradiance is:

10 / 0.689 = 14.5

The laser levels used for this experiment are more than 14 times lower than the maximum permissible exposures at the cornea, thus this experiment is safe for the eye.

B.2   Retinal imaging illumination

The light source is a Light - Emitting - Device (LED) of 530 nm wavelength entering the eye in a Maxwellian illumination as illustrated in Figure B.2a which is a development of Figure B.1. The angular extend of the retinal illumination for imaging is 5° (87.3 mrad).

The beam is composed of flashes of light of 1.33 ms duration separated by 30 μs overshoot. Given this duty cycle of 97.75%, we can approximate the beam as a continuous illumination, as presented in Figure B.3.
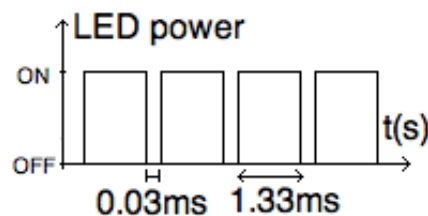
Figure B.3: Flash timeline for the retinal imaging illumination

The power of the source measured at the corneal plane with a powermeter is of 252μW over the 10mm-diameter aperture of the sensor head. The geometry of the source in the corneal plane is annular, the internal ring is of 5 mm diameter and the external ring is of 7 mm diameter. The consecutive area on the cornea is thus:

π*(7 x10^{-3})^2 / 4 - π*(5 x10^{-3})^2 / 4 = 18.8 x10^{-6} m^2

And the resulting corneal irradiance for this source is:

252x10^{-6} / 18.8 x10^{-6} = 13.4 W.m^{-2}

The duration of the experiment is set to 3.6x10^3 s (1 hour).

B.2.1 EU standard for retinal illumination

B.2.1.1 EU Photochemical limit

For the retinal photochemical hazard, as the timeline is in the case:

10^2 s $<$ t = 3.6x10^3 s $< 10^4$ s

We must refer to Table A.2 of [1] with the system's parameters :

MPE$_{ph}$(λ = 530 nm, α = 87.3 mrad, t = 3.6x10^3 s) = 1 C$_3$ W.m^{-2}

With the limiting angle of acceptance γ_{ph} defined by:

γ_{ph} = 1.1 $t^{0.5}$ mrad.

For our experiment duration t = 3.6x10^3 s :

γ_{ph} = 1.1 * (3.6x10^3)$^{0.5}$ mrad = 66 mrad

Note:

As paragraph 3.50 of [1], p.14 and section A.4.3 of [1] p.61 specifies the definition of γ_{ph}. This angle must be taken into account for the calculation of the photochemical limit :

"The angle γ_{ph} is related to eye movements and is not dependent upon the angular subtense of the source. If the angular subtense of the source is larger than the specified limiting angle of acceptance γ_{ph}, the angle of acceptance γ is limited to γ_{ph} and the source is scanned for hotspots. If the measurement angle of acceptance γ is not limited to the specified level, the hazard may be over-estimated."

and:

"If the angular subtense of the source α is larger than the specified limiting angle of acceptance γ_{ph}, the angle of acceptance should not be larger than the values specified

for γ_{ph}. If the angular subtense of the source α is smaller than the specified limiting angle of acceptance γ_{ph}, the angle of acceptance should fully encompass the source under consideration but need not otherwise be well defined (i.e. the angle of acceptance needs not be restricted to γ_{ph})."

The effective MPE irradiance according to the hypothesis forementioned thus becomes:

$$MPE_{ph} = \frac{C_3}{\Omega_{\gamma_{ph}} = \frac{\pi\gamma_{ph}^2}{4}} \ (\Omega_{source} = \frac{\pi\alpha^2}{4}) \ \text{W.m}^{-2} \qquad (B.1)$$

After elimination of the constants :
$\text{MPE}_{ph} = \frac{C_3}{\gamma_{ph}^2}\alpha^2 \ \text{W.m}^{-2}$

And given C_3 is given by Table 10 of p.49, [1].
$C_3(450 \ \text{nm} < \lambda = 530 \ \text{nm} < 600 \ \text{nm}) = 10^{0.02(\lambda-450)}$
$C_3 = 10^{0.02(530-450)} = 39.8$

We obtain:
$\text{MPE}_{ph} = \frac{39.8}{0.066^2}0.0873^2 = 69.6 \ \text{W.m}^{-2}$

That way the limiting angle γ_{ph} is taken into account in the calculation of the photo-chemical maximum permissible exposure.

B.2.1.2   EU Thermal limit

As dual limits apply, the retinal thermal hazard is given depending on T_2, set by Table 10 of [1].
$T_2(\lambda = 530 \ \text{nm}, \alpha = 87.3 \ \text{mrad}) = 10 \times 10^{[(\alpha-\alpha_{min})/98.5]} \ \text{s}$
That is, with the angular extend of the source as defined $\alpha = 87.3 \ \text{mrad}$:
$T_2 = 10 \times 10^{[(87.3-1.5)/98.5]} = 74.3 \ \text{s}$
Thus with $t > T_2$
$\text{MPE}_{Thermal}(\lambda = 530 \ \text{nm}, t = 3.6\text{x}10^3 \ \text{s}) = 18 \ C_6 T_2^{-0.25} \ \text{W.m}^{-2}$
In which:
$C_6 = \frac{\alpha}{\alpha_{min}} = \frac{87.5\times10^{-3}}{1.5\times10^{-3}} = 58.3$
$\text{MPE}_{Thermal}(\lambda = 530 \ \text{nm}, t = 3.6\text{x}10^3 \ \text{s}) = 18 * 58.33 * 74.31^{-0.25} = 357.6 \ \text{W.m}^{-2}$

B.2.1.3   Conclusion on EU limit

The minimum limit that must be applied in this case is thus set by the photochemical limit at 69.65 W.m^{-2} and thus the ratio between the experimental irradiance calculated in the introductive part of this section and the photochemical limit is :

69.65 / 13.4043 = 5.2

We can say that the light levels used in the experiment are more than 5 times safe for the eye.

B.3   Conclusion

With 5 times under the safety limits the illumination levels are considered as safe for the eye but given the sensitivity of the photoreceptors at 530 nm, the use of pulsed illumination is used, which lowers the average power in the eye and provides additional comfort of viewing to the subject.

For the adaptive optics wavefront sensing beam, the factor considering the use of ophthalmic drugs reduces the safety levels, but the laser beacon is sent in the eye for the time of closing the loop only.

Thus the timeline of the experiment is given for the longest possible exposure, and the safety limits have been calculated for the worst case scenario, but the patient is not exposed to the different sources during the whole experiment.

The MPE levels for the retinal illumination and for the beam diameter at the cornea and the power considered have also been verified to be consistent with the US standards using the OcLc calculator software provided by Prof. F. Delori, Schepens Eye Research Institute and Department of Ophthalmology, Harvard Medical School, Boston, USA.

Appendix C

Aberration of subject S3

Figure C.1 displays the wavefront sensing data for the subject S3, which point spread function with and without adaptive optics was displayed in Chapter 4, Section 4.4.2, Figure 4.15. The dimensions of the uncorrected double pass point spread function let expect an aberration of large amplitude, confirmed by the amplitude of the aberration measurement by the sensor.

C.1 Wavefront reconstruction data for S3

Wavefront root mean squared (rms) error calculated from 35 coefficients including and excluding tip and tilt are respectively presented in Figure C.1a and Figure C.1b. In the usual representation, tip and tilt terms are not included in the calculation of the rms. Given the influence of these terms on the aberration measurement was observed in Section 3.3.3.4, Figure 3.14. Both rms calculations with and without tip and tilt terms are presented. In other subjects, tip and tilt amplitudes were identified as the source of the high rms values, but for this subject, the limit amplitudes for tip, tilt and defocus are not reached. The aberration measurement is nevertheless not leveling, that is that other terms could be at the origin of the rms increase.

Zernike wavefront coefficients (first 21 terms) are presented in Figure C.2. For each dynamic range the coefficient is calculated from the average coefficient (100, 73 and 19 frames for dynamic ranges 12, 24 and $36\lambda/D$ respectively) after reconstruction of the open-loop frames presented in the rms display Figure C.1a and Figure C.1b. The
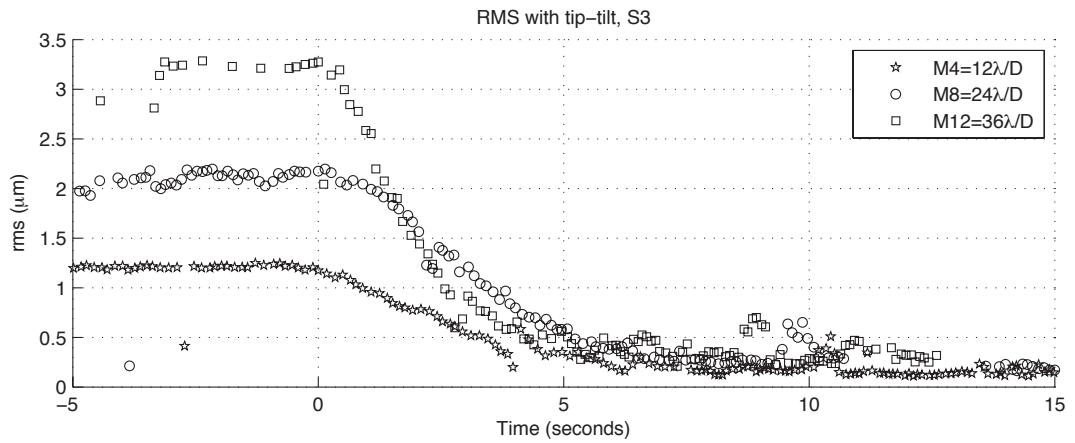
(a)
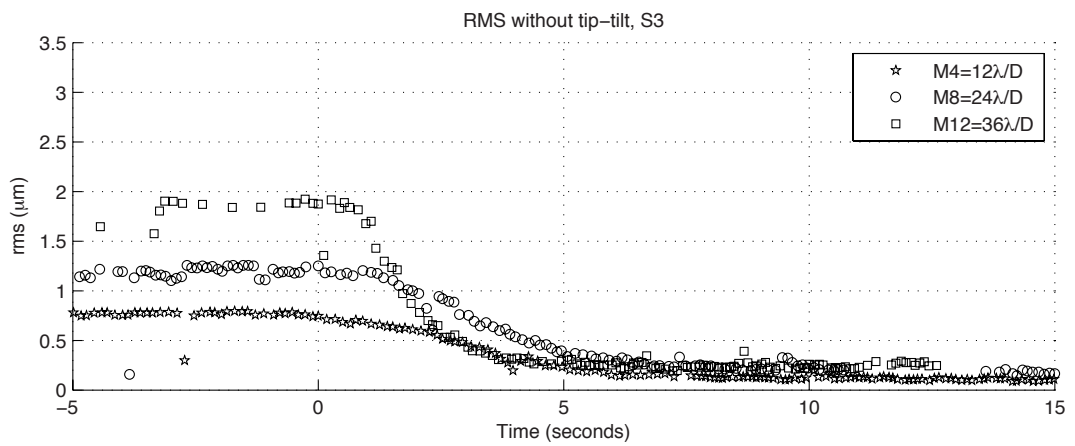
(b)

Figure C.1: Figures for the S3 wavefront rms sensor data

increase in a coefficient value with the increase in dynamic range is estimated as representative of the sensor saturation for this term. Tip, Tilt and Defocus (j=1, 2, 4) terms are identified as the main contributors for the wavefront error.
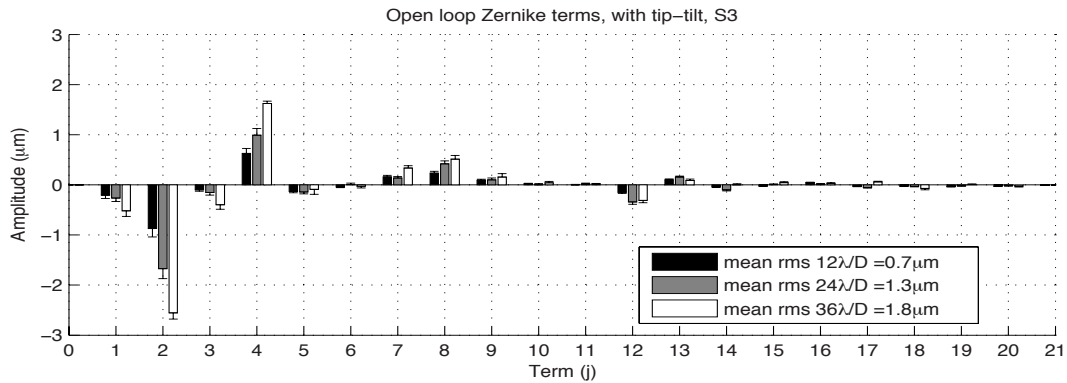
Figure C.2: Zernike decomposition of open-loop aberration

Open loop and closed loop values of tip, tilt and defocus terms are displayed in Figure C.3a, Figure C.3b and Figure C.3c. Figure C.3a shows the contribution of tip term is zero in the open-loop rms and does not require correction by the adaptive optics. Figure C.3b shows a tilt term of (-0.9, -1.7 and -2.6 μm) amplitude for the respective dynamic ranges (12, 24 and 36 λ/D), that is below the saturation values for this Zernike aberration order. Figure C.3c displays a defocus term (j=4) of (0.6, 1 and 1.6μm) for the respective dynamic ranges (12, 24 and 36 λ/D) before adaptive optics, meaning that the saturation amplitude of the sensor for this term is not obtained.

In conclusion, even though the aberration measurement for this subject in this experimental set is not saturated by tip, tilt and defocus terms, leveling of the ocular wavefront rms is not observed. The saturation of the sensor by other Zernike orders as presented in Section 3.3.3.2 is not necessarily avoided by the use of large dynamic ranges. In addition noise constraints for a given order limit the accuracy of the aberration measurement. Reconstruction of the aberration corrected by the mirror commands might allow this quantification.

151

(a)

(b)

(c)
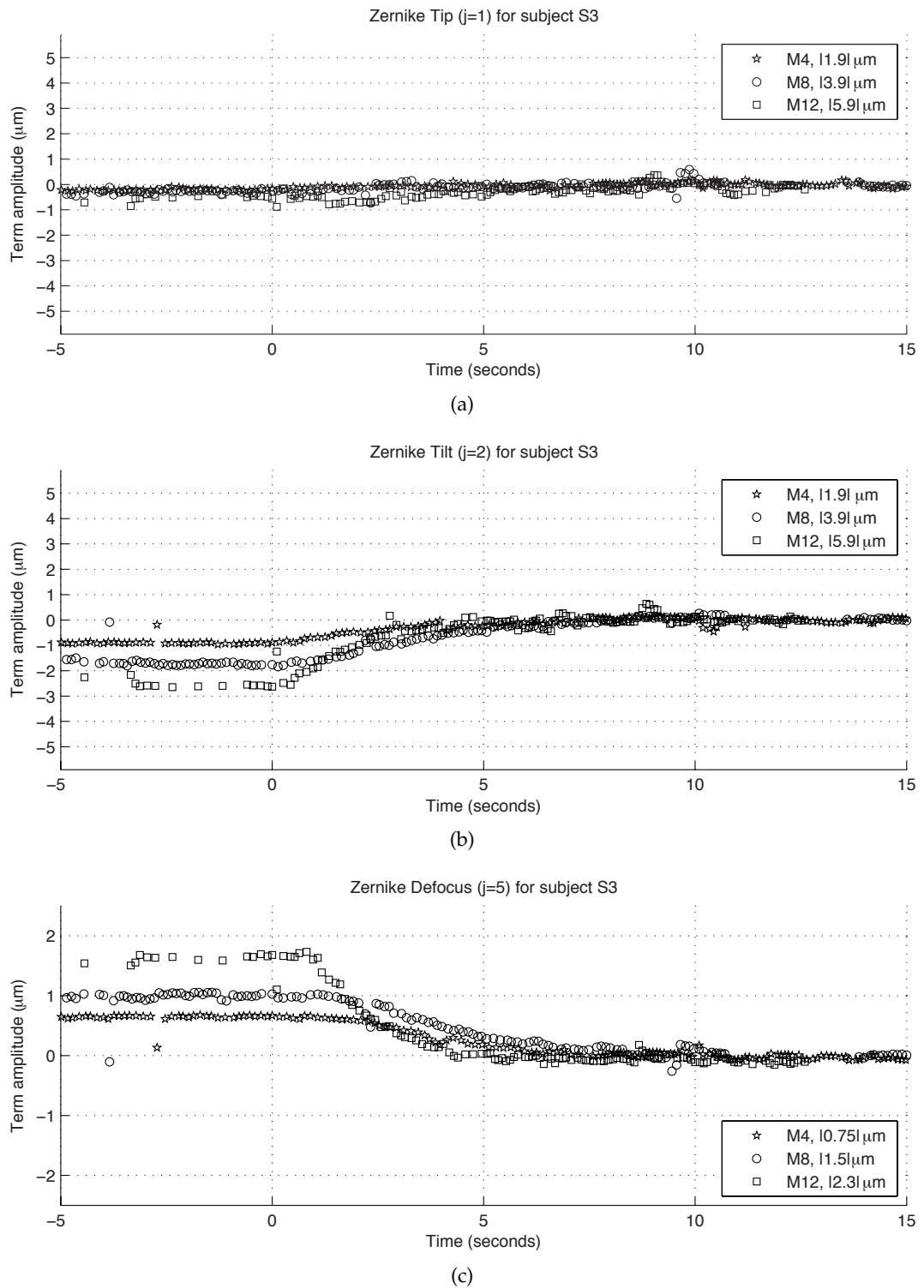
Figure C.3: S3 tip, tilt, defocus terms from sensor data

Bibliography

[1] S. R. Chamot, C. Dainty, and S. Esposito, "Adaptive optics for ophthalmic applications using a pyramid wavefront sensor," Opt. Express **14**, 518–526 (2006).

[2] S. L. Polyak, *The Retina* (University of Chicago Press, Chicago, 1941).

[3] L. Diaz-Santana and J. C. Dainty, "Effects of retinal scattering in the ocular double-pass process," J. Opt. Soc. Am. A. **18**, 1437–1444 (2001).

[4] M. Nowakowski, M. Sheehan, D. Neal, and A. V. Goncharov, "Investigation of the isoplanatic patch and wavefront aberration along the pupillary axis compared to the line of sight in the eye," Biomed. Opt. Express pp. 240–258 (2012).

[5] L. Thibos, M. Ye, X. Zhang, and A. Bradley, "The chromatic eye: a new reduced-eye model of ocular chromatic aberration in humans," Appl. Opt. **31**, 3594–3600 (1992).

[6] H. Hofer, L. Chen, G. Y. Yoon, B. Singer, Y. Yamauchi, and D. R. Williams, "Improvement in retinal image quality with dynamic correction of the eye's aberrations," Opt. Express **8**, 631–643 (2001).

[7] K. Grieve, P. Tiruveedhula, Y. Zhang, and A. Roorda, "Multi-wavelength imaging with the adaptive optics scanning laser ophthalmoscope," Opt. Express **14**, 12230–12243 (2006).

[8] D. De Brouwere, H. Ginis, G. Kymionis, I. Naoumidi, and I. Pallikaris, "Forward scattering properties of corneal haze," Opt. Vis. Science **85**, 843–848 (2008).

[9] J. M. Bueno, D. De Brouwere, H. Ginis, I. Sgouros, and P. Artal, "Purkinje imaging system to measure anterior segment scattering in the human eye," Opt. Lett. **32**, 3447 (2007).

[10] D. A. Peyrot, F. Aptel, C. Crotti, F. Deloison, S. Lemaire, T. Marciano, S. Bancelin, F. Alahyane, L. Kowalczuk, M. Savoldelli, J.-M. Legeais, and K. Plamann, "Ef-

fect of incident light wavelength and corneal edema on light scattering and penetration: Laboratory study of human corneas," J. Refract. Surgery **26**, 786–795 (2010).

[11] J. M. Bueno and M. C. W. Campbell, "Confocal scanning laser ophthalmoscopy improvement by use of Mueller-matrix polarimetry," Opt. Lett. **27**, 830–832 (2002).

[12] S. Marcos, R. Navarro, and P. Artal, "Coherent imaging of the cone mosaic in the living eye," J. Opt. Soc. Am. A. **13**, 897–905 (1996).

[13] D. Catlin and C. Dainty, "High-resolution imaging of the human retina with a Fourier deconvolution technique," J. Opt.Soc. Am. A **19**, 1515–1523 (2002).

[14] J. Liang, D. Williams, and D. Miller, "Supernormal vision and high-resolution retinal imaging through adaptive optics," J. Opt. Soc. Am. A. **14**, 2884–2892 (1997).

[15] J. Rha, S. Jonnal, Ravi, K. E. Thorn, J. Qu, Y. Zhang, and D. T. Miller, "Adaptive optics flood-illumination camera for high speed retinal imaging," Opt. Express **14**, 4552–4569 (2006).

[16] R. S. Jonnal, R. Jungtae, Y. Zhang, B. Cense, W. Gao, and D. T. Miller, "In vivo functional imaging of human cone photoreceptors," Opt. Express **15**, 16141 – 16160 (2007).

[17] M. Glanc, E. Gendron, F. Lacombe, D. Lafaille, J. F. Le Gargasson, and P. Léna, "Towards wide-field retinal imaging with adaptive optics," Optics Communications **230**, 225–238 (2004).

[18] B. Xue, S. S. Choi, N. Doble, and J. Werner, "Photoreceptor counting and montaging of enface retinal images from an adaptive optics fundus camera," J. Opt. Soc. Am. A. **24**, 1364–1372 (2007).

[19] N. M. Putnam, H. J. Hofer, N. Doble, L. Chan, J. Caroll, and D. R. Williams, "The locus of fixation and the foveal cone mosaic," Journal of Vision **5**, 632–639 (2005).

[20] N. Doble, S. S. Choi, J. L. Codona, J. Christou, J. M. Enoch, and D. R. Williams, "In-vivo imaging of the human rod photoreceptor mosaic," Opt. Lett. (2010).

[21] D. Merino, J. C. Dainty, A. Bradu, and A. G. Podoleanu, "Adaptive optics enhanced simultaneous en-face optical coherence tomography and scanning laser ophthalmoscopy," Opt. Express **14**, 3345–3353 (2006).

[22] A. Roorda and D. R. Williams, "The arrangement of the three cone classes in the living human eye," Nature **397**, 520–523 (1999).

[23] K. Grieve and A. Roorda, "Intrinsic signals from human cone photoreceptors," Invest. Ophthalmol. Vis. Sci. **49**, 713–719 (2008).

[24] S. A. Burns, S. Wu, F. Delori, and A. E. Elsner, "Direct measurement of human cone photoreceptor alignment," J. Opt. Soc. Am. A. **12**, 2329–2338 (1995).

[25] S. A. Burns, S. Wu, J. C. He, and A. E. Elsner, "Variations in photoreceptor directionality across the central retina," J. Opt. Soc. Am. A. **14**, 2033–2041 (1997).

[26] S. A. Burns, R. Tumbar, A. E. Elsner, D. Ferguson, and D. X. Hammer, "Large-field-of-view, modular, stabilized, adaptive-optics-based scanning laser ophthalmoscope," J. Opt. Soc. Am. A. **24**, 1313–1326 (2007).

[27] D. C. Gray, W. Merigan, J. I. Wolfing, B. P. Gee, J. Porter, A. Dubra, T. H. Twietmeyer, K. Ahmad, R. Tumbar, F. Reinholz, and D. R. Williams, "In vivo fluorescence imaging of primate retinal ganglion cells and retinal pigment epithelial cells," Opt. Express **14**, 7144–7158 (2006).

[28] D. P. Biss, D. Sumorok, S. A. Burns, R. H. Webb, Y. Zhou, T. G. Bifano, D. Côté, I. Veilleux, P. Zamiri, and C. P. Lin, "In vivo fluorescent imaging of the mouse retina using adaptive optics," Opt. Lett. **32**, 659–661 (2007).

[29] A. Bindewald-Wittich, M. Han, S. Schmitz-Valckenberg, S. R. Snyder, G. Giese, J. F. Bille, and F. G. Holz, "Two-photon excited fluorescence imaging of human RPE cells with a femtosecond Ti:Sapphire laser," Investigative Ophthalmology and Visual Science **47**, 4553–4557 (2006).

[30] D. Malacara, *Optical Shop Testing* (Wiley-Interscience, 2006), 3rd ed.

[31] A. G. Podoleanu, J. A. Rogers, D. A. Jackson, and S. Dunne, "Three dimensional OCT images from retina and skin," Opt. Express **7**, 292–298 (2000).

[32] R. G. Cucu, A. G. Podoleanu, J. A. Rogers, J. Pedro, and R. B. Rosen, "Combined confocal/en face t-scan-based ultrahigh-resolution optical coherence tomography in vivo retinal imaging," Opt. Lett. **11**, 1684–1686 (2006).

[33] Y. Zhang, J. Rha, R. Jonnal, and D. Miller, "Adaptive optics parallel spectral domain optical coherence tomography for imaging the living retina," Opt. Express **13**, 4792–4811 (2005).

[34] A. R. Tumlinson, B. Hermann, B. Hofer, B. Považay, T. H. Margrain, A. M. Binns, and W. Drexler, "Techniques for extraction of depth-resolved in vivo human retinal intrinsic optical signals with optical coherence tomography," Jpn J. Ophthalmol. **53**, 315–326 (2009).

[35] W. Gao, B. Cense, Y. Zhang, R. S. Jonnal, and D. T. Miller, "Measuring retinal contributions to the optical Stiles-Crawford effect with optical coherence tomography," Opt. Express **16**, 6486–6501 (2008).

[36] Y. Zhang, B. Cense, J. Rha, S. Jonnal, Ravi, W. Gao, R. J. Zawadzki, J. S. Werner, S. Jones, S. Oliver, and D. T. Miller, "High-speed volumetric imaging of cone photoreceptors with adaptive optics spectral-domain optical coherence tomography," Opt. Express **14**, 4380–4395 (2006).

[37] E. J. Fernández, B. Hermann, B. Považay, A. Unterhuber, H. Sattmann, B. Hofer, P. K. Ahnelt, and W. Drexler, "Ultrahigh resolution optical coherence tomography and pancorrection for cellular imaging of the living human retina," Opt. Express **16**, 11083 (2008).

[38] C. Torti, B. Považay, B. Hofer, A. Unterhuber, J. Carroll, P. K. Ahnelt, and W. Drexler, "Adaptive optics optical coherence tomography at 120,000 depth scans/s for non-invasive cellular phenotyping of the living human retina," Opt. Express **17**, 19382 (2009).

[39] R. Sabesan and G. Yoon, "Visual performance after correcting higher order aberrations in keratoconic eyes," Journal of Vision **9**, 1–10 (2009).

[40] E. J. Fernandez, L. Vabre, B. Hermann, A. Unterhuber, B. Povazay, and W. Drexler, "Adaptive optics with a magnetic deformable mirror: Applications in the human eye," Opt. Express **14**, 18 (2006).

[41] D. T. Miller, D. R. Williams, G. M. Morris, and J. Liang, "Images of cone photoreceptors in the living human eye," Vision Research **36**, 1067 – 1079 (1996).

[42] A. Burvall, E. Daly, S. R. Chamot, and C. Dainty, "Linearity of the pyramid wavefront sensor," Opt. Express **14**, 11925–11934 (2006).

[43] L. N. Thibos, R. A. Applegate, J. T. Schwiegerling, R. Webb, and V. S. T. Members, "Standards for reporting the optical aberrations of eyes," Conference Paper for Vision Science and its Applications (VSIA) pp. 232–244 (2000).

[44] E. Logean, E. Dalimier, and J. C. Dainty, "Measured double-pass intensity point-spread function after adaptive optics correction of ocular aberrations," Opt. Express **16**, 17348–17357 (2008).

[45] E. Dalimier and C. Dainty, "Comparative analysis of deformable mirrors for ocular adaptive optics," Opt. Express **13**, 4275–4285 (2005).

[46] T. Farrell, E. Daly, E. Dalimier, and C. Dainty, "Task-based assessment of deformable mirrors," Proc. of SPIE **6467**, 64670F (2007).

[47] N. Devaney, E. Dalimier, T. Farrell, D. Coburn, R. Mackey, D. Mackey, F. Laurent, E. Daly, and C. Dainty, "Correction of ocular and atmospheric wavefronts: a comparison of the performance of various deformable mirrors," Appl. Opt. **47**, 6550–6562 (2008).

[48] B. M. Welsh and M. C. Roggemann, "Signal-to-noise comparison of deconvolution from wave-front sensing with traditional linear and speckle image reconstruction," Appl. Opt. **34**, 2111–2119 (1995).

[49] J. C. Christou, A. Roorda, and D. R. Williams, "Deconvolution of adaptive optics retinal images," J. Opt. Soc. Am. A. **21**, 1393–1401 (2004).

[50] E. F. Y. Hom, F. Marchis, T. K. Lee, S. Haase, D. A. Agard, and J. W. Sedat, "AIDA: an adaptive image deconvolution algorithm with application to multi-frame and three-dimensional data," J. Opt. Soc. Am. A. **24**, 1580–1600 (2007).

[51] G. Chenegros, L. M. Mugnier, F. Lacombe, and M. Glanc, "3D phase diversity: a myopic deconvolution method for short-exposure images: application to retinal imaging," J. Opt. Soc. Am. A. **24**, 1349–1357 (2007).

[52] R. Ragazzoni, "Pupil plane wavefont sensing with an oscillating prism," Journal of Modern Optics **43**, 289–293 (1996).

[53] M. C. Roggemann and T. J. Schulz, "Algorithm to increase the largest aberration that can be reconstructed from hartmann sensor measurements," Appl. Opt. **37**, 4321–4329 (1998).

[54] L. A. Poyneer, D. T. Gavel, and J. M. Brase, "Fast wave-front reconstruction in large adaptive optics systems with use of the Fourier transform," J. Opt. Soc. Am. A. **19**, 2100–2111 (2002).

[55] R. Ragazzoni, A. Ghedina, A. Baruffolo, E. Marchetti, J. Farinato, T. Niero, G. Crimi, and M. Ghigo, "Testing the pyramid wavefront sensor on the sky," Proc. of SPIE **4007**, 423–430 (2000).

[56] F. Pérennès, M. Ghigo, M. Tormen, and S. Cabrini, "Production of identical pyramid wavefront sensors for multi-conjugate adaptive optic systems using the LIGA process," Proc. of SPIE, Microsystem Technologies **10**, 552–555 (2004).

[57] A. Tozzi, P. Stefanini, E. Pinna, and S. Esposito, "The double pyramid wavefront sensor for LBT," Proc. SPIE **7015**, 701558:1–9 (2008).

[58] A. Wang, J. Yao, D. Cai, and H. Ren, "Design and fabrication of a pyramid wavefront sensor," Proc. of SPIE **49**, 073401 (2010).

[59] B. Bauman, "Optical design for extremely large telescope adaptive optics systems," Ph.D. thesis, The University of Arizona (2003).

[60] L. Foucault, "Mémoire sur la construction des téléscopes en verre argenté," Annales de l'Observatoire de Paris **5**, 197–237 (1859).

[61] M. A. Van Dam, "Measuring the centroid gain of a Shack-Hartmann quad-cell wavefront sensor by using slope discrepancy," J. Opt. Soc. Am. A. **22**, 1509–1514 (2005).

[62] R. M. Clare and R. G. Lane, "Wave-front sensing from subdivision of the focal plane with a lenslet array," J. Opt. Soc. Am. A. **22**, 117–125 (2005).

[63] J. A. Johnson, R. Kupke, D. Gavel, and B. Bauman, "Pyramid wavefront sensing: theory and component technology development at LAO," Proc. SPIE, Advances in Adaptive Optics II **6272**, 62724R (2006).

[64] R. Kupke, D. Gavel, J. Johnson, and M. Reinig, "Implementation of the pyramid wavefront sensor as a direct phase detector for large amplitude aberrations," Proc. SPIE, Adaptive Optics Systems **7015**, 70155H (2008).

[65] J. Le Due, L. Jolissaint, J.-P. Véran, and C. Bradley, "Calibration and testing with real turbulence of a pyramid sensor employing static modulation," Opt. Express **17**, 7186–7195 (2009).

[66] O. A. Feeney, "Theory and laboratory characterization of novel wavefront sensor for adaptive optics systems," Ph.D. thesis, National University of Ireland, Galway (2001).

[67] S. Esposito and A. Riccardi, "Pyramid wavefront sensor behavior in partial correction adaptive optic systems," Astronomy and Astrophysics **369**, 9–12 (2001).

[68] J. B. Costa, R. Ragazzoni, A. Ghedina, M. Carbillet, C. Verinaud, M. Feldt, S. Esposito, E. Puga, and J. Farinato, "Is there need of any modulation in the pyramid wavefront sensor?" Proc. SPIE **4389** (2003).

[69] J. B. Costa, "Modulation effect of the atmosphere in a pyramid wave-front sensor," Appl. Opt. **44**, 60–67 (2005).

[70] D. Peter, M. Feldt, B. Dorner, T. Henning, S. Hippler, and J. Aceituno, "PYRAMIR: Calibration and operation of a pyramid near-infrared wavefront sensor," Publ. Astr. Soc. Pac. **120**, 872–886 (2008).

[71] D. Peter, M. Feldt, T. Henning, S. Hippler, J. Aceituno, L. Montoya, J. Costa, and B. Dorner, "PYRAMIR: Exploring the on-sky performance of the world's first near-infrared pyramid wavefront sensor," Publ. Astr. Soc. Pac. **122**, 63–70 (2010).

[72] I. Iglesias, R. Ragazzoni, Y. Julien, and P. Artal, "Extended source pyramid wave-front sensor for the human eye," Opt. Express **10**, 10 (2002).

[73] V. Korkiakoski, C. Vérinaud, M. Le Louarn, and R. Conan, "Comparison between a model-based and a conventional pyramid sensor reconstructor," Appl. Opt. **46**, 6176–6184 (2007).

[74] V. Korkiakoski, C. Vérinaud, and M. Le Louarn, "Improving the performance of a pyramid wavefront sensor with modal sensitivity compensation," Appl. Opt. **47**, 79–87 (2008).

[75] R. Ragazzoni, E. Diolati, and E. Vernet, "A pyramid wavefront sensor with no dynamic modulation," Optics Communications **208**, 51–60 (2002).

[76] R. Ragazzoni, J. Farinato, and E. Marchetti, "Adaptive optics for 100-m-class telescopes: new challenges require new solutions," (2000), vol. 4007, pp. 1076–1087.

[77] C. Arcidiacono, E. Diolaiti, M. Tordi, R. Ragazzoni, J. Farinato, E. Vernet, and E. Marchetti, "Layer-oriented simulation tool," Appl. Opt. **43**, 4288–4302 (2004).

[78] E. Diolaiti, A. Tozzi, R. Ragazzoni, D. Ferruzzi, E. Vernet-Viard, S. Esposito, J. Farinato, A. Ghedina, and A. Riccardi, "Some novel concepts in multipyramid wavefront sensing," Proc. of SPIE, Adaptive Optical System Technologies II **4839**, 299–306 (2003).

[79] C. Vérinaud, "On the nature of the measurements provided by a pyramid wavefront sensor," Optics Communications **233**, 27–38 (2004).

[80] M. Nicolle, T. Fusco, G. Rousset, and V. Michau, "Improvement of Shack-Hartmann wave-front sensor measurement for extreme adaptive optics," Opt. Lett. **29**, 2743–2745 (2004).

[81] L. A. Poyneer and B. Macintosh, "Spatially filtered wave-front sensor for high-order adaptive optics," J. Opt. Soc. Am. A. **21**, 810–819 (2004).

[82] C. Vérinaud, M. Le Louarn, V. Korkiakoski, and M. Carbillet, "Adaptive optics for high-contrast imaging: pyramid sensor versus spatially filtered Shack-Hartmann sensor," Mon. Not. R. Astron. Soc. **357**, 26–30 (2005).

[83] R. Ragazzoni and J. Farinato, "Sensitivity of a pyramidic wave front sensor in closed loop adaptive optics," AAP **350**, L23–L26 (1999).

[84] S. Esposito, A. Tozzi, A. Puglisi, L. Fini, P. Stefanini, P. Salinari, D. Gallieni, and J. Storm, "Development of the first-light AO system for the large binocular telescope," Proc. SPIE, Astronomical Adaptive Optics Systems and Applications **5169**, 149–158 (2003).

[85] E. Pinna, A. T. Puglisi, F. Quiros-Pacheco, L. Busoni, A. Tozzi, S. Esposito, E. Aller-Carpentier, and M. Kasper, "The pyramid wavefront sensor for the high order testbench (HOT)," Proc. SPIE **7015** (2008).

[86] E. Aller-Carpentier, M. Kasper, P. Martinez, E. Vernet, E. Fedrigo, C. Soenke, S. Tordo, N. Hubin, C. Verinaud, S. Esposito, E. Pinna, A. Puglisi, A. Tozzi, F. Quiros, A. G. Basden, S. J. Goodsell, G. D. Love, and R. M. Myers, "High order test bench for extreme adaptive optics system optimization," Proc. SPIE, Adaptive Optics Systems **7015**, 70153Z (2008).

[87] S. Esposito, E. Pinna, A. Tozzi, P. Stefanini, and N. Devaney, "Cophasing of segmented mirrors using the pyramid sensor," Proc. SPIE, Astronomical Adaptive Optics Systems and Applications **5169**, 72–78 (2003).

[88] S. Esposito, E. Pinna, A. Puglisi, A. Tozzi, and P. Stefanini, "Pyramid sensor for segmented mirror alignment," Opt. Lett. **30**, 2572–2574 (2005).

[89] B. Le Roux, "Pyramid wave-front sensing with a laser guide star for an ELT," in "Adaptive Optics: Methods, Analysis and Applications," (Optical Society of America, 2009), p. AOTuB3.

[90] S. R. Chamot, S. Esposito, and J. C. Dainty, "Application of pyramid wavefront sensing to ocular aberration measurements and corrections," in "Frontiers in Optics," (Optical Society of America, 2005), p. FThZ3.

[91] S. Chiesa, E. Daly, J. C. Dainty, and S. R. Chamot, "Adaptive optics system for retinal imaging based on a pyramid wavefront sensor," in "Adaptive Optics for Industry and Medicine," Sixth International Workshop National University of Ireland (Imperial College Press, 2008), pp. 336–341.

[92] E. M. Daly and J. C. Dainty, "Measuring phase aberrations using a pyramid wave front sensor," (2010), vol. 7726.

[93] E. M. Daly and J. C. Dainty, "Ophthalmic wavefront measurements using a versatile pyramid sensor," Appl. Opt. **49**, G67–G77 (2010).

[94] A. Riccardi, N. Bindi, R. Ragazzoni, S. Esposito, and P. Stefanini, "Laboratory characterization of a "Foucault-like" wavefront sensor for adaptive optics," **3353**, 941–951 (1998).

[95] D. A. Atchison, "Recent advances in measurement of monochromatic aberrations of human eyes," Clinical and Experimental Optometry **88**, 5–27 (2005).

[96] L. Thibos, X. Hong, A. Bradley, and X. Cheng, "Statistical variation of aberration structure and image quality in a normal population of healthy eyes," J. Opt. Soc. Am. A. **19**, 2329–2348 (2002).

[97] J. Porter, A. Guirao, I. G. Cox, and D. R. Williams, "Monochromatic aberrations of the human eye in a large population," J. Opt. Soc. Am. A. **18**, 1793–1803 (2001).

[98] R. Iskander, B. A. Davis, M. J. Collins, and R. Franklin, "Objective refraction from monochromatic wavefront aberrations via Zernike power polynomials," Ophthal. Physiol. Opt. pp. 245–255 (2007).

[99] L. Thibos, "Handbook of visual optics," (2008).

[100] R. J. Noll, "Zernike polynomials and atmospheric turbulence," J. Opt. Soc. Am. **66**, 207–211 (1976).

[101] K. Hampson, "The higher-order aberrations of the human eye: relation to the pulse and effect on vision," Ph.D. thesis, Imperial College, London (2005).

[102] D. R. Neal, D. M. Topa, and J. Copland, "Resolution effects on the dynamic range and accuracy of ophthalmic wavefront sensing," in "Vision Science and its Applications," (Optical Society of America, 2001), p. SuD5.

[103] J. Schwiegerling, *Field Guide to Visual and Ophthalmic Optics* (SPIE Press book, Field guides, 2004).

[104] R. Navarro, E. Moreno-Barriuso, S. Bará, and T. Mancebo, "Phase plates for wave-aberration compensation in the human eye," Opt. Lett. **25**, 236–238 (2000).

[105] C. E. Leroux, A. Tzschachmann, and J. C. Dainty, "Pupil matching of Zernike aberrations," Opt. Express **18**, 21567–21572 (2010).

[106] L. N. Thibos, "Retinal image quality for virtual eyes generated by a statistical model of ocular wavefront aberrations," Ophthalmic and Physiological Optics **29**, 288–291 (2009).

[107] T. Shirai, "Liquid-crystal adaptive optics based on feedback interferometry for high-resolution retinal imaging," Appl. Opt. **41**, 4013–4014 (2002).

[108] J. W. Hardy, *Adaptive optics for astronomical telescopes* (Oxford University Press, 1998).

[109] E. Dalimier, "Adaptive Optics Correction of Ocular Higher-Order Aberrations and the Effects on Functional Vision," Ph.D. thesis, Department of Experimental Physics, National University of Ireland, Galway (2007).

[110] W. Zou and S. A. Burns, "High-accuracy wavefront control for retinal imaging with adaptive-influence-matrix adaptive optics," Opt. Express **17**, 20167–20177 (2009).

[111] A. Dubra, "Wavefront sensor and wavefront corrector matching in adaptive optics," Opt. Express **15**, 2672–2769 (2007).

[112] E. Daly, C. Dainty, G. O'Connor, and T. Glynn, "Wave-front correction of a femtosecond laser using deformable mirrors," Proc. SPIE **5708** (2005).

[113] E. Ödlund, H.-F. Raynaud, C. Kulčsar, F. Harms, X. Levecq, F. Martins, N. Château, and A. G. Podoleanu, "Control of an electromagnetic deformable mirror using high speed dynamics characterization and identification," Appl. Opt. **49**, G120–G128 (2010).

[114] R. K. Tyson, *Principles of Adaptive Optics* (Academic Press; 2 edition, 1998).

[115] G. Smith and D. A. Atchison, *The eye and visual optical elements* (Press syndicate of the University of Cambridge, 1997).

[116] C. A. Curcio, K. R. Sloan, O. Packer, A. E. Hendrickson, and R. E. Kalina, "Distribution of cones in human and monkey retina: Individual variability and radial asymmetry," Science **236**, 579–582 (1987).

[117] W. S. Stiles and B. H. Crawford, "The luminous efficiency of rays entering the eye pupil at different points," Proceedings of the Royal Society of London, Series B, Containing Papers of a Biological Character **112**, 428 – 450 (1933).

[118] G. Smith and D. A. Atchison, *Optics of the human eye* (Elsevier Science, 2003).

[119] J. W. Goodman, *Speckle phenomena in optics* (Roberts and Co., 2006).

[120] J. I. Yellot, "Spectral analysis of spatial sampling by photoreceptors: topological disorder prevents aliasing," Vision Res. (1982).

[121] K. Li and A. Roorda, "Automated identification of cone photoreceptors in adaptive optics retinal images," J. Opt. Soc. Am. A. **24**, 1358–1363 (2007).

[122] G. Österberg, "Topography of the layer of rods and cones in the human retina," Acta Ophthal. **Suppl.6**, 1–103 (1935).

[123] S. Marcos, S. A. Burns, E. Moreno-Barriusop, and R. Navarro, "A new approach to the study of ocular chromatic aberrations," Vision Research **39**, 4309–23 (1999).

[124] R. Sabesan, K. Ahmad, and G. Yoon, "Correcting highly aberrated eyes using large-stroke adaptive optics," Journal of Refractive Surgery **23**, 947–952 (2007).

[125] L. Diaz Santana Haro, "Wavefront sensing in the human eye with a Shack-Hartmann sensor," Ph.D. thesis, University of London (2002).

[126] P. Artal, S. Marcos, R. Navarro, and D. R. Williams, "Odd aberrations and double-pass measurements of retinal image quality," J. Opt. Soc. Am. A. **12**, 195–201 (1995).

[127] R. A. Applegate, W. J. Donnelly III, J. D. Marsack, and D. E. Koenig, "Three-dimensional relationship between high-order root-mean-square wavefront error, pupil diameter, and aging," J. Opt. Soc. Am. A. **24**, 578 – 587 (2007).

[128] M. J. Booth, "Wavefront sensorless adaptive optics for large aberrations," Opt. Lett. **32**, 5–7 (2007).

[129] N. Meitav and E. N. Ribak, "Improving retinal image resolution with iterative weighted shift-and-add," J. Opt. Soc. Am. A. **28**, 1395–1402 (2011).

[130] F. C. Delori, R. H. Webb, and D. H. Sliney, "Maximum permissible exposures for ocular safety (ANSI 2000), with emphasis on ophthalmic devices," J. Opt. Soc. Am. A. **24**, 1250–1266 (2007).